Vortex-Surface Interactions

An experimental investigation and the development of a conceptual model

Jeremy van Mourik Broekman

TU Delft

Vortex-Surface Interactions

An experimental investigation and the development of a conceptual model

by

J.M. van Mourik Broekman

to obtain the degree of Master of Science
at the Delft University of Technology,
to be defended publicly on Friday September 1, 2017 at 14:00 AM.

Student number:	1517759	
Project duration:	Febuary 1, 2016 – September 1, 2017	
Thesis committee:	Prof. dr. ir. G. Eitelberg,	TU Delft
	Dr. D. Ragni,	TU Delft
	Dr. M. Kotsonis,	TU Delft
	Ir. T. Sinnige,	TU Delft, supervisor

An electronic version of this thesis is available at `http://repository.tudelft.nl/`.
Thesis registration number: 159#17#MT#FPP

TU Delft

Preface

J.M. van Mourik Broekman
Delft, August 2017

It is such a relief finally writing this text. I still cannot quite believe that the report is finished. Looking back at the past 18 months, I can honestly say that it has been the hardest time of my life in but also a highly educational one. The lessons learnt did not lie so much in the academic aspect of the project, but more on a personal level. Specifically, I learnt a lot about dealing with setbacks, as there have been a few. From failing components, to failing greenlight meetings, from personal losses to self-doubt. It has not been an easy process. That is not to say that there were no good times. I thoroughly enjoyed teaming up with my supervisors to find an explanation for the results from the experimental campaign and preparing for the experiment with DEMO was a definite highlight. All in all it was a wild ride and I am ready to move forward.

Finally, I would like to thank a few people:

My parents, for having been supportive of me my entire life, in everything I have done and every choice I have made.

Bella, for listening to me in the hard times and allowing me to help you in yours.

Jasper and Sergio, for being in this mess together and being able to make fun of it and ourselves.

My friends and family, for cheering me on the during the final stretch.

Ed Roessen, for taking your time and helping me develop the 'the wheel of fortune'.

And of course Tomas, for putting in so much time and energy to pull me across the finish line. I could not have done it without your help.

Summary

The high efficiency of open rotor propulsion has led to a comeback of propeller propulsion systems in recent years. The main issue preventing wide application of the technology is its high noise level. One of the main contributors to this noise is the pressure fluctuations generated during the interaction between a propeller tip vortex and a downstream surface. The vortex-surface interaction phenomenon can be broken down in a number of components, or 'sub-phenomena', such as the low pressure vortex core, the shearing of the vortex and the induced angle of attack effect. The interaction is governed by a number of parameters such as the vortex strength and orientation, the surface geometry and the flow conditions. The goal of this research project is to create a better understanding of the vortex-surface interaction, which would allow for more effective noise mitigation strategies to be developed. An experimental approach was adopted to quantify the effect of a number of governing parameters on the pressure fluctuations over the surface induced by the vortex. Furthermore, an attempt was made to develop a conceptual model describing the vortex-surface interaction in order to study the relative contributions of the sub-phenomena of the interaction. The accuracy of the conceptual model was assessed using the data obtained from the experimental campaign.

The experiment was performed in the M-tunnel of the Delft University of Technology. Vortices were generated using a propeller driven by an electric motor placed in the open jet windtunnel. Wing sections were placed in the flow at the tunnel exit. Each section contained a chordwise row of embedded microphones that was used to measure the unsteady pressure fluctuations over the surfaces. The wing sections were moved in lateral direction through the flow to map the spanwise distribution of the pressure fluctuations at each chordwise microphone position. The independent variables were the advance ratio, freestream velocity, airfoil geometry and incidence angle, which is the angle between the vortex axis and the lateral surface axis. The advance ratio and freestream velocity were controlled with the engine and windtunnel settings. To investigate the effect of the airfoil geometry, the two wing sections were designed with different profiles, one with a NACA0012 and the other a NACA0016 profile. Additionally, the wings were mounted in a cylindrical wing mount that could be rotated about its axis, allowing for the investigation of the effect of the incidence angle of the vortex on the pressure fluctuations over the surface.

From the results it was clear that the low pressure vortex core was the primary mechanism that generated fluctuations over the surface. The vortex path was clearly visible and dominant over a large part of the chord. In the slipstream region the wake generated the largest pressure fluctuations. The effect of the wake was contained at the leading edge, up to 4% of the wing chord. Changing the advance ratio from 0.67 to 0.60 resulted in an increase of maximum root mean square of the unsteady pressure coefficient, $C'_{p,RMS}$, in the vortex impingement region of 156% and 28% on the advancing and retreating sides, respectively. The increase in pressure fluctuation was attributed to the increase in vortex strength associated with the increase in blade loading. Contrary to expectations, there was no discernible change in vortex path with a change in advance ratio. However, this could be due to the relatively small change in advance ratio. Changing the freestream velocity from 10 to 15 m/s, while keeping the advance ratio constant at 0.67, only caused an increase in $C'_{p,RMS}$ of 60% on the advancing side. Additionally, it did not visibly change the distribution of the unsteady pressure. The effect of the airfoil geometry was less than expected, with no discernible change in pressure fluctuation magnitude. The vortex path, however, was shifted outboard by 0.25 and 0.5 y/r_0 on the advancing and retreating side respectively. The impact of the vortex incidence angle, i.e. the angle between the vortex axis and the spanwise surface axis, on both the magnitude and distribution of the pressure fluctuations was significant. On the advancing side, a change in angle from 0 to 90 degrees led to a decrease in peak $C'_{p,RMS}$ of 72.5 %. On the retreating side, the same change in incidence angle causes a 27% decrease in $C'_{p,RMS}$. Additionally, for both sides the width of the peak increased dramatically, from being a clearly discernible peak to spanning the entire width of the measured wingspan.

At the leading edge an unexpected region of low pressure fluctuations was observed between up to 4% of the wing chord, which was not expected. After further analysis of the microphone waveforms in this region, it

was theorized that the lack of unsteady pressure resulted from interference between the propeller wake and the vortex. No definitive proof could be provided and further research is required to fully understand the physical events that result in the observed behavior.

A conceptual model was developed by breaking down the vortex-surface interaction into a number of sub-phenomena, such as the vortex core pressure, vortex shearing and the induced angle of attack effect, and adding those that were expected to have the largest impact on the magnitude and distribution of the pressure fluctuations to the model. The components that were selected were the vortex core pressure and the induced angle of attack effect. A number of assumptions were made in order to model the sub-components. The vortex core pressure was modeled using a Lamb-Oseen vortex model and Bernoulli's law for curved flow. The induced angle of attack effect was assumed to originate from velocities induced by the vortex as extracted at the leading edge of the wing.

The assessment of the model was done by comparing the model results with the results obtained from the experiment. Large discrepancies between the unsteady pressure, both in magnitude and in spatial distribution, were observed. Three contributing factors to the discrepancies were identified. Firstly, the induced angle of attack effect was overestimated. In the experimental results, the contribution of this sub-phenomenon was not discernible, while in the model results it was the main contributor to the pressure fluctuations. The two-dimensional approach that makes use of the velocities induced by the vortex at the leading edge was not appropriate. Secondly, the Lamb-Oseen vortex used to model the vortex core pressure underestimated the size of the vortex core due to a number of assumptions contained in the model. Finally, the vortex radius was determined from the experimental results and used as an input in the model. However, the method with which this was done led to erroneous values for the vortex radius. These discrepancies implied that the conceptual model could not be used for its intended purposes.

The results of this study show that the advance ratio and incidence angle are the most critical parameters governing the vortex-surface interaction. Although the former is difficult to incorporate into noise mitigation strategies, the latter can be used as a parameter in the initial design phase. Interestingly, the geometry of the airfoil seems to have limited effect on both the magnitude and distribution of the interaction. Although the conceptual model discussed in this report is not accurate, the development of such a simplified model would still contribute a lot to the body of knowledge. It could be used to evaluate the relative contributions of the different vortex-surface interaction sub-phenomena, as suggested in this project. Another use would be the execution of a 'parameter sweep' to investigate the effect of the governing parameters on the unsteady pressure distribution and magnitude, which was done in a more limited manner with the experimental campaign. However, for the latter intended use the approach taken in this project would not be recommended as the level of fidelity would be too low. A much in-depth approach is recommended seeing the complex behavior of the flow.

Contents

List of Figures

List of Tables

Nomenclature

Acronyms

DAQ	Data Acquisition
FPL	Fluctuating Pressure Level
FOW	Field Of View
LSL	Low Speed Laboratory
NI	National Instruments
PIV	Particle Image Velocimetry
PTU	Programmable Timing Unit
RMS	Root Mean Square
RPS	Rotations Per Second
SPL	Sound Pressure Level
UDF	Unducted Fan

Greek symbols

α	Angle of attack	$[deg]$
β	Vortex pitch angle	$[deg]$
ϵ	Miss distance	$[m]$
$\epsilon_{V,mean}$	Mean velocity error	$[m/s]$
ϵ_V	Instantaneous velocity error	$[m/s]$
η_p	Ideal propulsive efficiency	$[-]$
γ	Incidence angle	$[deg]$
ν	Kinematic viscosity	$[kg/(s*m)]$
ω	Vorticity	$[1/s]$
ϕ	Phase angle	$[deg]$
ρ_∞	Freestream density	$[kg/m^3]$
σ_V	Standard deviation of velocity component V	$[-]$
Γ	Circulation	$[m^2/s]$

Roman symbols

A_p	Cross-sectional area of the propeller plane	$[m^2]$
A_{neck}	Cross-sectional area of resonator neck	$[m^2]$
A_{wt}	Cross-sectional windtunnel area	$[m^2]$

c	Chord	$[m]$
C'_p	Unsteady pressure coefficient	$[-]$
$C'_{p,RMS}$	Root mean square of the unsteady pressure coefficient	$[-]$
C_p	Pressure coefficient	$[-]$
C_T	Thrust coefficient	$[-]$
$C_{p,base}$	Baseline pressure coefficient	$[-]$
$C_{p,ind}$	Induced pressure coefficient	$[-]$
$C_{p,vor}$	Vortex pressure coefficient	$[-]$
D_p	Diameter of propeller	$[m]$
dt	Pulse delay	$[s]$
F	Frequency	$[Hz]$
F_{eig}	Eigenfrequency	$[Hz]$
J	Advance ratio	$[-]$
J_{eq}	Equivalent advance ratio	$[-]$
L	Characteristic length	$[m]$
l_{corr}	Resonator neck end-correction	$[m]$
l_{neck}	Resonator neck length	$[m]$
M_{pix}	Magnification factor	$[-]$
N	Number of images taken in PIV measurement	$[-]$
n	RPS	$[-]$
p	Pressure	$[Pa]$
p_s	Static pressure	$[Pa]$
p_t	Total pressure	$[Pa]$
p_∞	Freestream pressure	$[Pa]$
R	Propeller radius	$[m]$
r	Distance to vortex center	$[m]$
r_c	Vortex core radius	$[m]$
r_{cav}	Resonator cavity radius	$[m]$
R_{hub}	Radial distance from propeller center to base of the blade	$[m]$
R_{tip}	Radius of propeller blade	$[m]$
T	Thrust	$[N]$
t	Vortex age	$[s]$
T_b	Thrust produced per blade	$[N]$
T_{off}	Thrust measured with the propeller removed from setup	$[N]$

T_{on}	Thrust measured with the propeller on the setup	$[N]$
u	Velocity component in x-direction	$[m/s]$
V_a	Flow velocity in axial direction	$[m/s]$
V_j	Jet velocity	$[m/s]$
V_t	Tangential velocity	$[m/s]$
$V_{\infty,eq}$	Equivalent freestream velocity	$[m/s]$
V_∞	Freestream velocity	$[m/s]$
$V_{LO,tan}$	Tangential velocity of Lamb-Oseen vortex model	$[m/s]$
V_{prop}	Propeller slipstream velocity	$[m/s]$
x	Axial coordinate	$[m]$
y	Spanwise coordinate	$[m]$

Sub- and superscripts

$'$	Unsteady component
1/3	One-third octave bands
$base$	Baseline
cc	Calibration correction curves
cor	Corrected
ind	Induced
mic	Surface microphone
ref	Reference microphone
tot	Total
x	Orientated in the x-direction
y	Orientated in the y-direction
z	Orientated in the z-direction

I

Background

1 Introduction

The context of the research project is provided in section 1.1, followed by the research goal, research objective and research questions in section 1.2. Finally, in section 1.3 the outline of the report is discussed.

1.1. Context of Research

At the advent of powered flight the propulsion mechanism of choice was the propeller. During the first half of the twentieth century a lot of research was performed on propeller theory and design, resulting in an extensive base of knowledge on the matter [1]. During the second world war the demand for aircraft that operated faster and at higher altitudes led to the conception of the turbojet. With low oil prices and the high amounts of thrust produced by this propulsion method the interest in propeller research waned. However, with the rise in fuel cost in the seventies, increasing propulsive efficiency was a key driver in aircraft propulsion research, leading to the resurgence of propeller research [2].

The intrinsic difference between a propeller and a turbojet is that the former generates a small increase in velocity to large amount of air, while the latter does the opposite. The formulaic representation of the ideal propulsive efficiency η_p is expressed as:

$$\eta_p = \frac{2}{1 + \frac{V_j}{V_\infty}} \tag{1.1}$$

where V_∞ is the freestream velocity and V_j is the jet velocity. Examining equation 1.1 one can conclude that the propeller driven propulsion is inherently more efficient than turbojet propulsion. The higher propulsive efficiency translates to a lower specific fuel consumption, which is visualized in figure 1.1.
The higher efficiency of the turboprop with respect to the turbojet is true up to moderate Mach numbers and flight altitudes. From a certain Mach number, dependent on the design, the propeller blade tips move at supersonic speeds, causing significant wave drag. Seeing that the Mach numbers at which this phenomenon occurs are lower than the operating speed of the turbojet the effective operating speed and altitude of the turboprop are therefore significantly lower. As a response to the increase in fossil fuel price in the late seventies NASA devised a propulsion concept that promised to solve this problem: the advanced turboprop or propfan [1, 2]. In essence the concept consists of a turbine driven open propeller system. More specifically the need for high power loading led to a propeller with an increased number of blades, larger blade chord and highly swept blades. Examples of advanced turboprop designs showing the key characteristics are presented in figure 1.2. Due to the decrease in fuel cost in the late eighties, many of the designated NASA programs were canceled and a lot of the technology was shelved.

In recent years, increased understanding of the effects of global warming on the environment and the expected growth of the world population have led to calls to reduce the environmental impact of aerospace travel, making advanced turboprop research relevant once again. Collaborations between aerospace manufacturers and governmental organizations have resulted in reports such as the FlightPath 2050 Initiative, authorized by the European Commission [5]. These documents lay out long-term aircraft emissions and

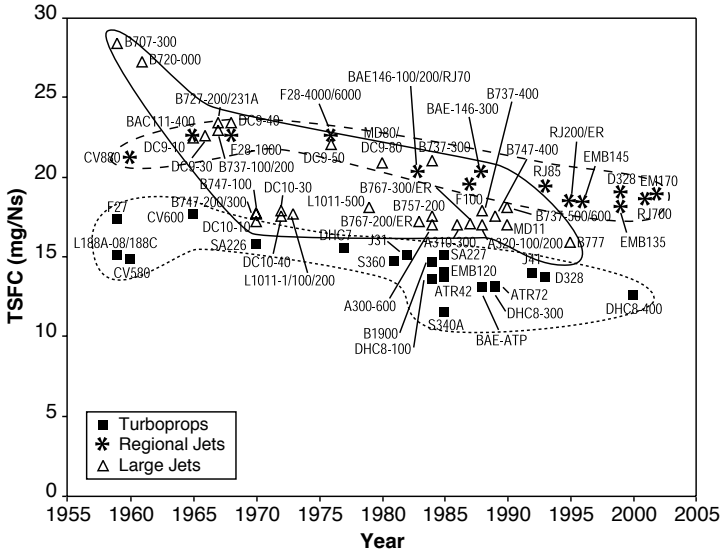

Figure 1.1: Historical trends of the specific fuel consumption at cruise thrust setting for various turbojet and turboprop aircraft. Note that the cruise velocities are not equal for different planes and / or technologies [3]

noise targets, such as a 75% reduction in CO_2 emissions and a 65% reduction in perceived noise emissions with respect to standard levels in the year 2000. Although the advanced turboprop technology contributes to lower CO_2 emissions [6], propeller noise generation is still a significant issue. Due to the tonal nature of propeller noise it is perceived as being more annoying than the broadband noise generated by turbojets [7]. Furthermore, the absence of a cowling allows the noise to radiate outward freely [8]. These aspects, among others, lead to higher perceived cabin and far-field noise levels with respect to modern turbofan engines.

Far-field noise from the engines causes noise exposure around airports during aircraft landing and take-off, which is strictly regulated. Additionally, increased cabin noise reduces passenger comfort, which is an important design consideration for manufacturers. Tonal propeller noise is generated through a number of mechanisms [8]; the first is the isolated propeller noise, which consists mainly of propeller thickness and loading noise. Secondly, there may exist unsteady loading on the propeller due to installation effects [9]. Finally, noise is generated by the interaction between the propeller slipstream and any downstream surfaces. Of these noise sources the latter still poses large challenges. The pressure fluctuations generated on the surface by the slipstream, of which the discrete propeller tip vortex is the main contributor due to its strong and localized velocity field [8], results in both radiated noise and in structure-borne noise, which comprises the propagation of noise from aerodynamically induced vibrations through the airframe into the cabin. The former is not significant compared to the latter, which is regarded to be a major source of passenger discomfort [10] and is harder to mitigate than the cabin noise resulting from the direct airborne propeller noise [11].

The focus of this thesis will be on the vortex surface interactions, which encompasses propeller tip vortex-surface interactions but also Blade Vortex Interactions, vortex chopping that occurs in Counter Rotating Open Rotor technology and many more. Research on this topic is necessary seeing the relevance of propeller technology in fuel-efficient air transportation methods and seeing that high noise levels are one of the major challenges still facing this technology. As the subject is very extensive, a literature study has been performed to map out the opportunities and challenges that exist within the research area. The conclusions from the study, resulting research objective and the outline of the report are presented the next section.

1.2. Research Objective

Vortex-surface interactions are highly complex phenomena with unsteady, three-dimensional and non-linear flow. The phenomenon can be broken up into multiple components, or 'sub-phenomena', such as the low pressure vortex core, induced angle of attack effect and vortex shearing, each with its own governing parameters. A better quantification and understanding of the relative contribution of the different sub-phenomena

(a) PTA propfan concept developed by Lockheed for the NASA Advanced Turboprop Project [2].

(b) Unducted Fan (UDF) developed by G.E. for the NASA Advanced Turboprop Project [2].

(c) TP400 turboprop developed by Europrop currently used on the Airbus A400M [4]

Figure 1.2: Various advanced turboprop engines.

and the effect of the governing parameters on the pressure fluctuations induced by the vortex over the surface will help in evolving a methodology for low noise designs [12]. Some of the sub-phenomena have been studied extensively, while others have not. Belonging to the former are the aerodynamic interference between the propeller slipstream and downstream surfaces [9], the trailing vortex structure [13], and the behavior of the vortex [14]. Less well understood are sub-phenomena such as vortex bending and shearing or the viscous interactions between the vortex and surface boundary layer, which have been described qualitatively but not quantitatively [15, 16], at least not in the level of detail required. The sub-phenomena will be discussed at greater length in Chapter 2.

Additionally, the current trend in the aeroacoustic community is to improve acoustic prediction strategies that can be used in the early design stage, which is currently not the case, in order to define low-noise configurations with the help of optimization algorithms [17]. In order to do so, an analysis tool is required that can perform fast iterative designs to optimize the final outcome. A number of high-fidelity compressible Navier-Stokes solvers have been developed to predict the sound generation [18, 19]. However, these solvers require significant amounts of computational power and are therefore disqualified for the use intended here. Analytical noise prediction models, such as those developed by Roger [8, 17, 20, 21], Amiet [22] and Kingan [23], require much less computational power, but many sub-phenomena of which the interaction comprises are not contained in these models.

Although noise mitigation is the underlying rationale to study the vortex-surface interaction, the scope of this

research project is limited to the pressure fluctuations over the surface resulting from the interaction. The audible noise resulting from the interaction will not be considered. The understanding of the distribution of the pressure fluctuations over the surface and on the effects of the parameters governing the interaction on the fluctuations, can be translated into noise mitigation strategies. An experimental campaign will be performed to measure the pressure fluctuations induced by a vortex over a surface. Although experimental data on vortex-surface interaction is available [10, 15, 24], these campaigns were focused on the propeller surface interaction as a whole and not specifically tailored toward the investigation of the vortex.

Additionally the development of a fast analysis tool describing the vortex-surface interaction is attempted in this research project. A conceptual model, consisting of a simplified version of reality that contains certain aspects of the phenomenon, or 'sub-phenomena', and neglects others, is developed and assessed. In constructing the model, a balance will be sought between accuracy, speed and the measure in which it can be validated. The validation will be done by making use of the experimentally obtained data. The advantage of this approach is that by containing a number of the key sub-phenomena in the model, it is possible to study their relative effect on the pressure fluctuations and allow for a more fundamental understanding of the interaction.

The goal of the research is to obtain a better understanding of the vortex-surface interaction in order to facilitate noise mitigation strategies. This goal will be achieved by performing an experimental campaign to quantify the effect of a number of governing parameters on the pressure fluctuations over the surface induced by the vortex. Furthermore, a conceptual model describing the vortex-surface interaction will be developed in order to study the relative contributions of the sub-phenomena. The accuracy of the conceptual model will be assessed using the data obtained from the experimental campaign. From this we can summarize the following research objective:

Quantify the effect of the governing parameters and sub-phenomena on the magnitude and distribution of the vortex induced pressure fluctuations over a surface by performing an experimental campaign and developing a conceptual model.

Based on the the research objective a number of research questions are proposed. The research questions can in turn be split into more specific multiple sub-questions:

- What is the effect of the governing parameters on the pressure fluctuations induced by the vortex over the surface during the interaction?
  - Which parameters are critical for the vortex surface interaction?
  - What effect do the selected parameters have on the magnitude of the pressure fluctuations on the surface?
  - What effect do the selected parameters have on the distribution of the pressure fluctuations on the surface?
- How accurate is the conceptual model?
  - What are the quantitative differences between the experimental data and the model results?
  - To what modeling approaches can the differences be attributed?
- What is the relative contribution of the sub-phenomena to the pressure fluctuations induced by the vortex over the surface during the interaction?

1.3. Report Outline

The thesis was performed as follows. First, a literature study was done to investigate different aspects of the vortex-surface interaction, vortex models and experimental techniques. Then the experimental campaign was executed, followed by the processing of the gathered data. The conceptual model was created afterwards and finally a validation of the model using the results from the experiment took place.

This report contains the most important aspects of the project. It should be noted that the order in which the material is presented is not the same as with which it was executed during the project. In Chapter 2 the relevant results of the literature study, which covered the different phenomena occurring during the vortex-surface interaction, are presented. This knowledge is required to design of the experimental campaign, choose the measurement techniques and the select of the test conditions, as is covered in Chapter 3. The knowledge is also necessary for the development of the conceptual model, which is discussed in Chapter 4 and where the selection of the components of the model and its structure will be presented.

The accuracy of the experimental data and the verification of the conceptual model is discussed in Chapter 5. In Chapter 6 the results from the experimental campaign are discussed and the accuracy of the conceptual model is assessed using the experimental data. In Chapter 7 the results from these analyses are used to answer the research questions and conclusions on the research objective are drawn. In the same Chapter a discussion of the project as a whole and recommendations for future research are presented.

2

Theoretical background

To better design the conceptual model and the experimental campaign it is useful to examine the theoretical background of the phenomena at hand. In order to do so a number of different aspects, namely the propeller slipstream characteristics, vortex behavior and vortex-surface interaction phenomena will be discussed. Propeller theory itself is of less interest, seeing that the focus of the project is on the interaction of the slipstream with downstream objects. However, historically a lot of research has been performed on the topic of propeller theory, with an experimental study on propeller geometry by the Wright brothers as one of the earliest examples. Later a number of analytical models have been created that describe the performance of propeller blades such as the actuator disk theory and the Blade Element Method. A recommended work on these topics has been written by Glauert [25]. Also worth mentioning is a wide ranging study on the topic of propeller aerodynamics written by Wald [13].

With respect to fundamental vortex theory a comprehensive book has been written by Green [14], which covers all facets of the topic. A number of notable authors who have written about vortex-surface interaction are Johnston, Sullivan [26], who performed experimental research on the topic in the late eighties and early nineties as a result of the resurgence of propeller engine research. One of the first analytical models predicting the sound pressure levels resulting from vortex-surface interactions was devised by Amiet [22]. More recently a series of papers on the vortex-surface interaction between CROR blades was written by Roger [8, 17, 20, 21].

In the first section of this chapter the propeller slipstream characteristics are discussed seeing that they affect the pressure fluctuations generated by the vortex. In section 2.2 the vortex itself will be covered, including its fundamental characteristics, vortex models and the helical vortex structure. The different aspects concerning vortex-surface interactions and parameters describing this interaction will be treated in section 2.3.

2.1. Propeller Slipstream Phenomena

The interaction between the incoming flow and the propeller results in a number of changes to the flow with respect to the freestream flow conditions. The pressure differential between the upper and lower side of the propeller blade, indicated in figure 2.1 with Δp_s, created by the rotational movement and shape of the blade causes an increase in flow speed in axial direction (V_a in figure 2.1), both up- and downstream of the propeller blade. Due to the viscous interaction between the blade surface and the incoming flow a velocity component in tangential direction around the propeller axis is also created, which is called the swirl component of the flow.

The steady increase in axial velocity results in higher dynamic pressure over the wing, increasing the amount of lift over any surfaces situated behind the propeller compared to surfaces outside the slipstream. These differences result in spanwise gradients in lift. The effect of the swirl on the wing loading depends on the location of the surface with respect to the propeller axis. On the downward going blade side the swirl is perceived as a downwash, locally reducing the loading over the wing. On the upward going blade side, the opposite is true. The possible combinations of the axial velocity and swirl components and their effect on the spanwise lift distributions is visualized qualitatively in figure 2.2.

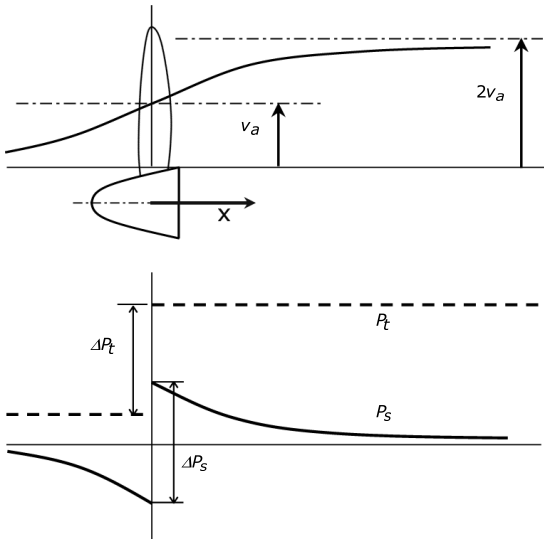

Figure 2.1: Qualitative example of the total pressure, P_t, and static pressure, P_s, in the slipstream and the flow speed in axial direction, V_a, as a function of x-coordinate [9].

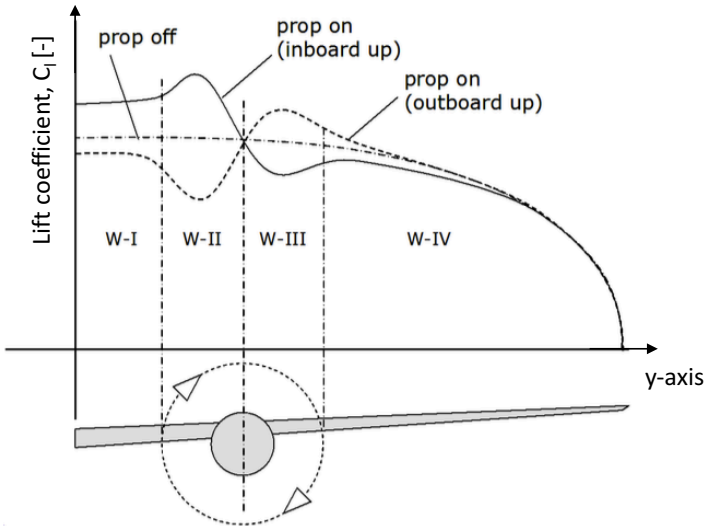

Figure 2.2: Qualitative representation of the combined effect of the axial and swirl components of the propeller slipstream on the lift distributions over a wing [9].

Although the axial and swirl components are quasi-steady [9] there exists an additional periodic component, namely the blade wake. It can be viewed as the periodic element of the swirl component. With respect to surfaces that are situated downstream of the propeller, the unsteady components of the propeller slipstream result in periodic variations in dynamic pressure and angle of attack. Furthermore, the downstream flow as a whole has higher levels of turbulence than the upstream flow resulting from the interaction between the blade and the flow. Finally, there are discrete propeller tip-vortices trailing each propeller blade, of which the origin and characteristics are discussed at greater length in section 2.2 and their interaction with downstream surfaces will be discussed in section 2.3.

2.2. Vortex Behavior

According to Green [14], a vortex is an inherently vague term and therefore no single definition has gained broad acceptance. However, most definitions do make use of one, or both, of the underlying concepts,

namely vorticity and circulation. "Vorticity is a measure of a fluid element's rotation about a given axis", according to Gowanlock [27]. Formally vorticity, $\vec{\omega}$, is defined as the curl of the velocity field, $\vec{u}$, as expressed mathematically in equation 2.1. It should be noted that, being the curl of a vector quantity, vorticity is also a vector. Another important concept, one that is closely related, is circulation, Γ. The circulation about any closed curved line, C, is defined as the line integral of the velocity around that curve, as expressed in equation 4.1. It is related to the flux of the vorticity passing through the area bounded by the line, as is expressed in equation 2.3. This means that if there exists circulation around some curve, there must be vorticity running through the curve.

$$\vec{\omega} = \nabla \cdot \vec{u} \tag{2.1}$$

$$\Gamma = \oint_C \vec{u} \cdot \mathrm{d}\vec{l} \tag{2.2}$$

$$\Gamma = \iint_S \vec{\omega} \cdot \mathrm{d}\vec{A} \tag{2.3}$$

Definitions for the term 'vortex' range from those that are relatively open to interpretation, such as "a clearly identifiable region of large vorticity which is surrounded by irrotational fluid" [14], to very precise definitions, such as "a two-dimensional vortex can be defined as a simply-connected region of a fluid bounded by the contour on which $|\vec{\omega}|$ is 20% of the local extremum of $|\vec{\omega}|$" [28]. For this project an often used definition provided by Gowanlock [27] will be used: "A vortex can be viewed as any region of concentrated vorticity".

An important descriptor of a vortex, next to the amount vorticity and circulation contained in a vortex, is the tangential velocity distribution. It provides a view of the compactness, or intensity, of the vortex. The more compact or intense a vortex is, the higher the tangential velocities will be near the core with respect to the velocities at some distance from the core. An example of the velocity distributions for vortices with different strengths, that is with different values of circulation, is provided in figure 2.3a. One way of determining the pressure distribution that corresponds to the tangential velocity distribution is by integrating Bernouilli's law for curved flow, which is expressed in equation 2.4. In this equation V_t is the tangential flow velocity at distance r from the vortex center. The pressure distributions corresponding to the tangential velocity distributions as provided in figure 2.3a obtained in this manner are provided in figure 2.3b.

$$\frac{dp}{dr} = \rho \cdot \frac{V_t^2}{r} \tag{2.4}$$

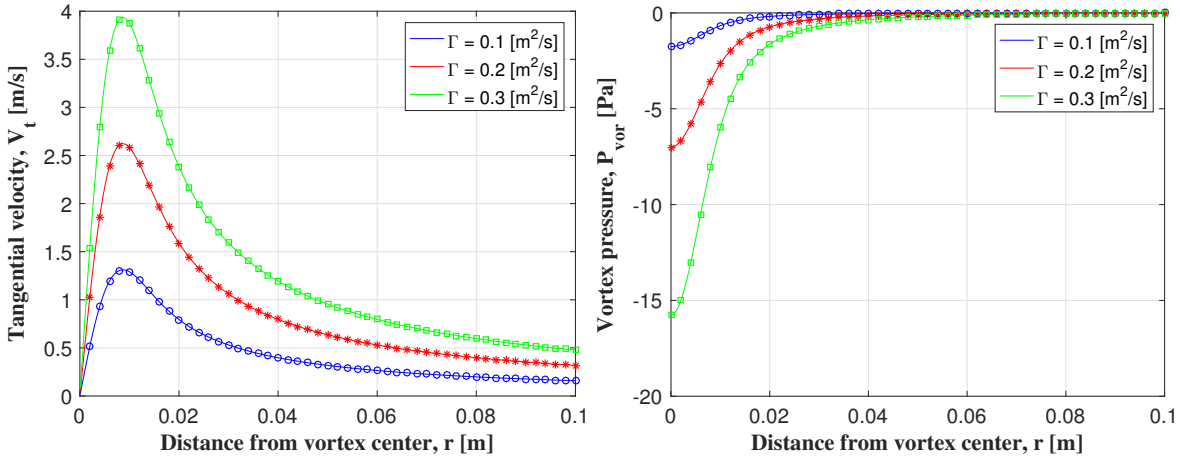

(a) Tangential velocity distributions.

(b) Pressure distributions.

Figure 2.3: Example of tangential velocity and pressure distributions of a Lamb-Oseen vortex with circulation values of 0.1, 0.1 and 0.3$[m^2/s]$ at a vortex age of 1$[s]$

One would like to be able to model vortices in order to understand their behavior and the impact they have in different situations. In order to do so theoretical models can be used to allow for numerical analysis. A large number of different models, with names such as the Iverson, Vatistas or Rankine [29] vortex models, are available. Different models contain different aspects, such as axial velocity, decay rate, etc. The Lamb-Oseen vortex model, in its original form or as a variation, is one of the most widely used vortex models. It describes a two-dimensional axisymmetric line vortex in an initially inviscid, infinite fluid [14]. Equation 2.5, in which ν is the kinematic viscosity and t the vortex age, describes the vortex core radius. This parameter is in turn used in equation 2.6 that describes the tangential velocity distribution as a function of the distance to the vortex center, defined by r. At time t = 0 viscosity starts to act on the flow and the diffusion of the vortex resulting from the viscous interaction can be analyzed. Decay over time as result of diffusion results in increased core size. As for the vortex definitions there are many ways to define the core size, but in this project the definition will be the distance between maximum and minimum tangential velocity.

$$r_c = \sqrt{4 \cdot \nu \cdot t} \tag{2.5}$$

$$V_t = \frac{\Gamma}{2 \cdot \pi \cdot r} \cdot \left[1 - e^{-\frac{r^2}{r_c^2}} \right] \tag{2.6}$$

As defined earlier, a vortex is an area of concentrated vorticity and thus contains a relatively high amount of energy. This energy will dissipate over time as the vortex interacts with its surroundings. Additionally, in reality the energy in a vortex is not spread consistently over its volume; certain parts contain more energy than others, leading to interactions between different parts of the vortex to distribute and diffuse the energy. This distribution, both within the vortex and with the surroundings, can be called vortex decay and is an important aspect of vortex theory. There are three mechanisms of vortex decay that occur naturally: viscous diffusion, expansion of existing flow instabilities and vortex bursting [27]. Viscous diffusion "involves a weak means of natural vortex decay which relies upon the effect of shear between fluid particles to slow the rotational velocities of the vortex to the point where they are no longer strong enough to overcome ambient disturbances." according to Gowanlock [27]. It is a process that acts on molecular level. Due to the fact that fluid viscosity is very low for air, diffusion is a relatively slow process [30].

Existing flow instabilities consist of small scale eddies that are initially located on the outer edge of the vortex structure. These eddies are relatively turbulent structures that promote the mixing of high and low momentum air, leading to the radial expansion and diffusion of the vortex. This in turn leads to a wider distribution of swirl velocity. At a young age, when the vortex is still concentrated, the centrifugal force of the vortex leads to laminar core flow and prevents the instabilities to reach the vortex core. It therefore imposes the aforementioned molecular diffusion process in the core region [30]. The final decay mechanism is called vortex bursting. As a vortex travels downstream, it enlarges and becomes more diffused. If the rotational velocity of the vortex drops low enough, the increasing pressure within the vortex causes it to lose its coherent structure and break apart. This in turn leads to a rapid increase in vortex diameter, mixing of the vortex with its surroundings and dispersion of turbulent kinetic energy. Generally speaking vortex bursting occurs at later vortex age and in different situations than is relevant for the vortex impingement problems discussed in research project.

In reality, vortices can be generated in a large number of manners. For example, the presence of a wingtip allows the flow to move from the high pressure region under the wing to the low pressure region on the upper side, causing a rotational movement in the flow resulting in a vortex, as is shown in figure 2.4. For the purpose of this research project, however, propeller tip vortices are considered. The generation method is the same as the trailing wingtip vortices explained above, but due to the orientation and the movement of the propeller with respect to the flow, the resulting vortex structure is very specific. That is to say that the vortices trailing from the propeller are shaped as a helix, as depicted in figure 2.5. Here the pitch of the helix, β, which is the angle of the vortex with respect to the x-axis positive toward the z-axis, as shown in figure 2.6, is dependent on the flow velocity, V_∞ and the propeller rotational speed, as expressed in equation 2.7 where the propeller diameter is denoted by D_p. From 0 to 1 propeller diameter distance behind the propeller plane the helix structure reduces due to increased axial velocity [32], a phenomenon that is called the contraction of the streamtube.

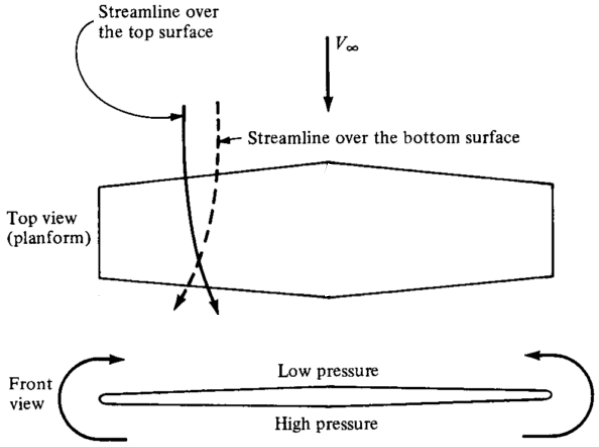

Figure 2.4: Schematic representation of vortex structures resulting from flow over a finite wing [31].

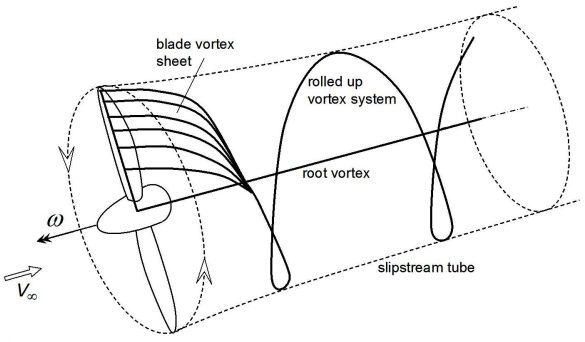

Figure 2.5: Schematic representation of the helical vortex structure resulting from a propeller [9].

$$\beta = \arctan\left(\frac{V_\infty}{RPS \cdot D_p \cdot \pi}\right) \tag{2.7}$$

Although it is easy to assume the vortex is completely formed when it leaves the propeller tip, this is not true in reality. The shedding of the circulation from the propeller occurs for a large part at the tip but also over the entire length of the propeller. This circulation then rolls up into the vortex over a period of time, as is depicted in figure 2.5. What is also important to note is that a propeller tip vortex contains an axial velocity component in the same direction as the swirl components of the flow as a whole.

2.3. Vortex-Surface Interaction Phenomena

The vortex-surface interaction is a complex phenomenon. It is unsteady, non-linear, three-dimensional and there exist large differences in length and time scales between the vortex and freestream flow [33]. The name 'vortex-surface interaction' covers a large variety of different phenomena that occur in reality, such as blade-vortex interactions in helicopter technology, vortex chopping as occurs in counter rotating open rotors, rotor-stator interactions and propeller tip vortex-wing interactions that occur in aircraft with a tractor configuration propulsion setup. The orientation and movement of the vortex with respect to the surface are different in each of these cases and have a large impact on the resulting pressure fluctuations.

Firstly, the distinction between collision and impingement should be made. Collision, as defined by Conlisk [33], refers to the situation where the vortex core is destroyed or significantly changed due to the interaction. An example of such an interaction is the cutting of a single vortex into two separate filaments as occurs during a perpendicular vortex-surface interaction (consult figure 2.6). Impingement on the other hand describes the situation where the main vortex velocity component acts perpendicular to the surface.

Normally, the axis of the vortex is aligned obliquely to the surface it interacts with. However, three distinct situations, namely two parallel (one with respect to the chord, the other with respect to the span of the surface) and one perpendicular alignment, can be identified. They are depicted in figure 2.6. In the case of the parallel interaction the intensity, defined as the change in pressure over time, is strongly related to the miss distance, ϵ, and the radius of the vortex core with respect to the surface nose radius. The first is important as the induced velocities experienced by the surface strongly decrease with distance, while the second parameter dictates if a collision or an impingement interaction occurs. If the nose radius is much smaller than the vortex core radius a collision may occur. If not, the interaction will be an impingement. One can therefore conclude that in the case of a parallel BVI a collision is unlikely. Moving from parallel to perpendicular interactions, there is less influence on the pressure distribution from induced velocities, and more from low pressure core. A perpendicular interaction however will always consist of a collision seeing that the axis of the vortex will always cross the surface plane.

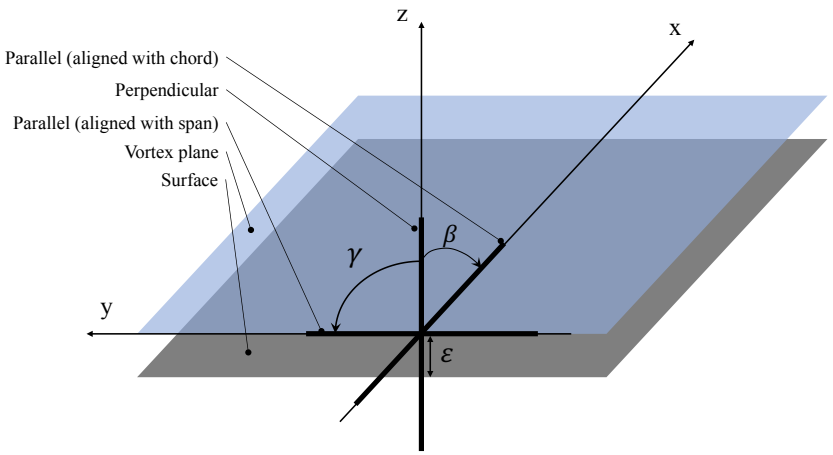

Figure 2.6: Schematic representation of different vortex orientations, miss distance and angles.

During a perpendicular vortex collision the behavior of the vortex at the leading edge and over the surface is for a large part dependent on the leading edge radius of the surface with respect to the vortex core size, wherein two extremes are identified. Firstly, if the nose radius is much smaller than the vortex core, the vortex is instantaneously sheared in two. The vortex contains an axial velocity component, which due to the presence of the surface must stagnate on the advancing side and tends to separate on the retreating side. This causes a thickening, or bulging, of the vortex on one side and a thinning on the other. This process has been captured by Johnston [26], as seen in figure 2.7a. A graphical representation of this phenomenon is provided by Conlisk [33] in figure 2.7b. The compression on the advancing side causes a pressure increase that propagates outward from the vortex and upward the filament. On the retreating side the vortex thins and causes a suction peak resulting in an inflow of boundary layer [34].

The other extreme occurs when the vortex core is of the same order or smaller than the leading edge radius. Instead of being sheared, the vortex core starts to bend around the leading edge. When the vortex filaments separate the part of the vortex closest to the airfoil is almost parallel to the surface. The resulting velocity components are perpendicular to the surface and have an impact on the pressure over the surface.

These induced velocity components are one of two phenomena causing the vortex induced pressure fluctuations over the surface, the other of which is the low static pressure in the vortex core. Due to the orientation of the vortex (expressed with pitch and incidence angle, consult figure 2.6) and the induced velocity components, an up- or downwash on the surface exists. This is called the induced angle of attack effect and is depicted in figure 2.8. The magnitude of the resulting pressure fluctuations depends on a number of aspects, such as the vortex strength, orientation and location. Also the airfoil shape and loading dictate the unsteady pressure distribution over the airfoil.

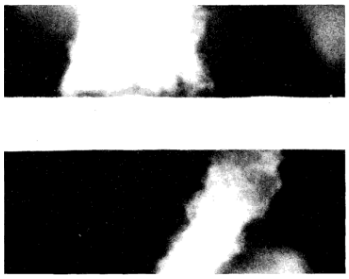

(a) Image taken during an experiment showing the vortex compression and stretching on the upper and lower side of the surface [26].

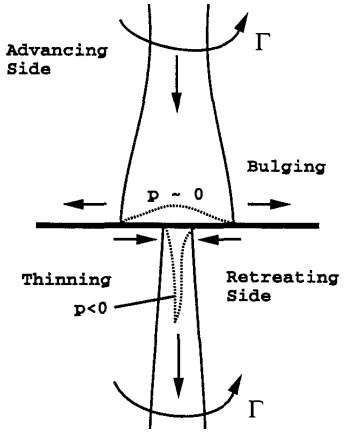

(b) Schematic representation of vortex compression and stretching [33].

Figure 2.7: Vortex compression and stretching.

As mentioned earlier the low static pressure in the core is the second phenomenon causing pressure fluctuations over the airfoil. As explained in section 2.2 the distribution and strength of the tangential velocity of the vortex dictate the pressure magnitude and distribution. Therefore the unsteady pressure distribution over the surface is dependent on the vortex strength, i.e. the circulation, its core radius and age. It is interesting to note that some of the recent noise mitigation research, such as the work by Han [29], Gorsul [35] and at the TU Delft by Vedamanickam [36], has focused on the reduction in noise through the accelerated vortex core diffusion by propeller tip blowing. This increases the tangential velocity distribution resulting in less intense pressure fluctuations.

Seeing that the low pressure vortex core is one of two main contributors to the presure fluctuations, the path the vortex travels is of importance for the distribution of the fluctuations. Therefore it is of interest to discuss a phenomenon called vortex shearing. As the sheared vortex filements travel downstream they start to move in opposite spanwise directions [16]. The direction and magnitude of the movement depends on the loading pattern over the wing [16]. According to the lifting-line theorem [31], the wing loading can be expressed as the amount of bound circulation of the wing. Every spanwise change in lift corresponds to a spanwise change in bound circulation, and is accompanied by a shed vortex representing the change in lift. These trailing vortices cause a spanwise flow to occur which affects the vortices. For a tractor propeller, an outward flow, i.e. away from the propeller axis, is present on the advancing side of the blade, while on the retreating side an inboard flow is present. Figure 2.9 shows the top view of the experimental setup with the direction of rotation of the propeller and the expected vortex shear movements for the top and bottom surfaces in a qualitative sense.

Additionally, the shear movement is expected to increase with increased loading, so for a lower advance ratio or an increase in angle of attack more movement is expected. Finally, it has been shown by Johnston [16] that the vortex on the advancing side of the surface shows significantly less vortex shear movement than on the other side. The underlying cause of this difference has not yet been determined, but the behavior could be related to the compression of the vortex on this side and the extension of the vortex on the other side [33].

Another aspect affecting the vortex path is the viscous interaction with the boundary layer. Not a lot of quantitative data is available on the effect of this interaction on the vortex characteristics but qualitatively a number of effects are clear. As with turbulent flow, a rapid distribution of vorticity through the boundary layer will occur, seeing that as the leading mechanism, namely the circulation of the vortex, is much faster than the viscous diffusion that normally causes the distribution of vorticity. The result of this distribution in vorticity is a reduction in vortex strength and an increase in vortex core size. Furthermore, due to the zero-slip condition at the airfoil surface the vortex convective velocity at the surface decreases with respect to its velocity in the freestream. This in turn results in a deformation of the vortex in the form of vortex bending.

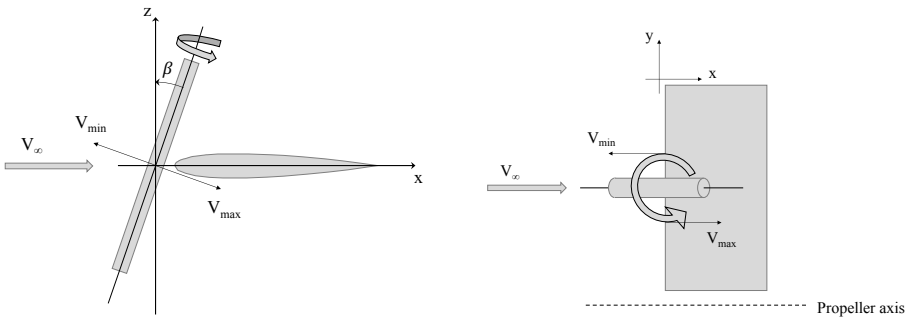

(a) Side view **(b)** Top view

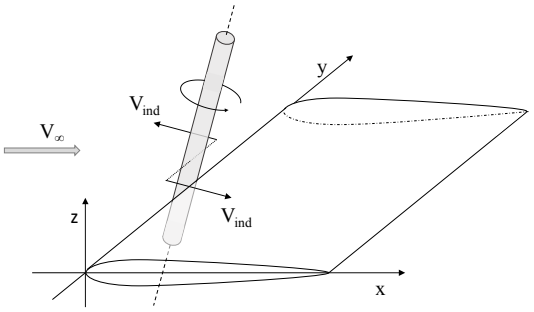

(c) Overview

Figure 2.8: Schematic representation of the induced angle of attack effect.

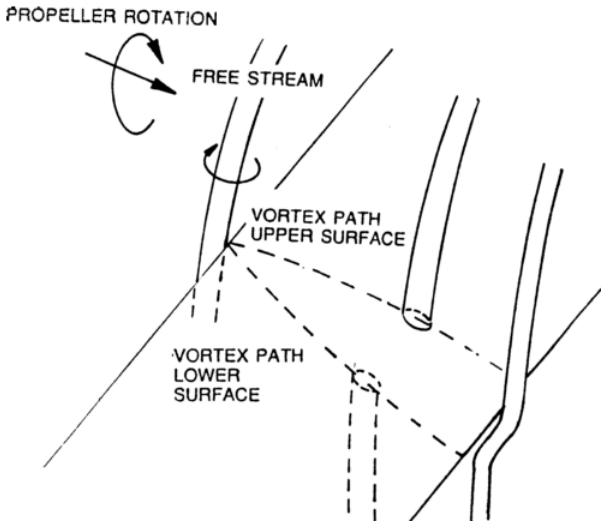

Figure 2.9: Schematic representation of vortex shearing [16]

II

Methodology

3

Experimental Campaign

As assessed in the previous chapter, there is a need for experimental data in order to validate the analytical model and to further investigate the vortex-surface interaction phenomenon. In this chapter, all aspects of the experimental campaign are covered. First, in section 3.1 the experimental setup will be presented. Then a review of the measurement techniques will be given in 3.2 and finally the test conditions will be discussed in section 3.3.

3.1. Experimental Setup

The experimental campaign is designed with two goals in mind. The first is the investigation of the vortex-surface interaction as an objective by itself. The second is the validation of the conceptual model. For both objectives the aim of the experiment is to obtain the unsteady pressure induced by vortex over a surface. Additionally, for both goals it is important to quantify the impact of certain parameters on the pressure fluctuations. This allows for a more thorough investigation of the interaction and for a broader validation of the conceptual model. From the literature study performed in advance of the research project it was concluded that the parameters most critical to the interaction are the propeller settings and geometry, surface geometry, flow conditions and vortex orientation.

The dependent variable of the experimental campaign is the unsteady pressure distribution over the advancing and retreating side of the surfaces, and that the independent variables are the advance ratio, freestream velocity, airfoil shape and incidence angle.The propeller settings are captured in the advance ratio, as defined in equation 3.3. The flow conditions that can be achieved are largely determined by the capabilities of the windtunnel. In this case the only adjustable parameter is the flow velocity. Finally the vortex orientation in case of the the most basic vortex-surface interaction, namely that of a tractor propeller configuration, is perpendicular to the surface. However, the incidence angle seems to have a large impact on the interaction so its influence will be studied as well.

For the validation of the conceptual model the governing parameters, such as the vortex strength, windtunnel velocity and Reynolds number, must be the same for both the experiment and the model. The experiment is designed such that its governing parameters are the same as those of the conceptual model. Additionally, since it is unavoidable that there are differences between the experiment and the model, the experiment should be designed so that the differences, or at least the impact thereof on the results, are minimized. Since the idealized conceptual model is designed to simulate a vortex surface interaction which is as fundamental as possible, meaning a sole vortex interacting with an airfoil without any other aerodynamic phenomena present, one would ideally design an experiment in which a single vortex interacts with an the airfoil in a windtunnel. This was initially tried, but these experiments were unsuccessful and due to limitations on time and resources a different approach was chosen.

Instead, the vortices were generated using a propeller driven by an electric motor placed in an open jet windtunnel. Movable wing sections are placed in the flow at the tunnel exit, as is presented in figure 3.1. The wing sections contain a single row of embedded microphones that are used to measure the pressure fluctuations

over the surface. The choice for this experimental setup was based on windtunnel availability, the available resources (both material and time) and the ease of use. Additionally, the differences between the conceptual model and the setup are limited and, importantly, well understood.

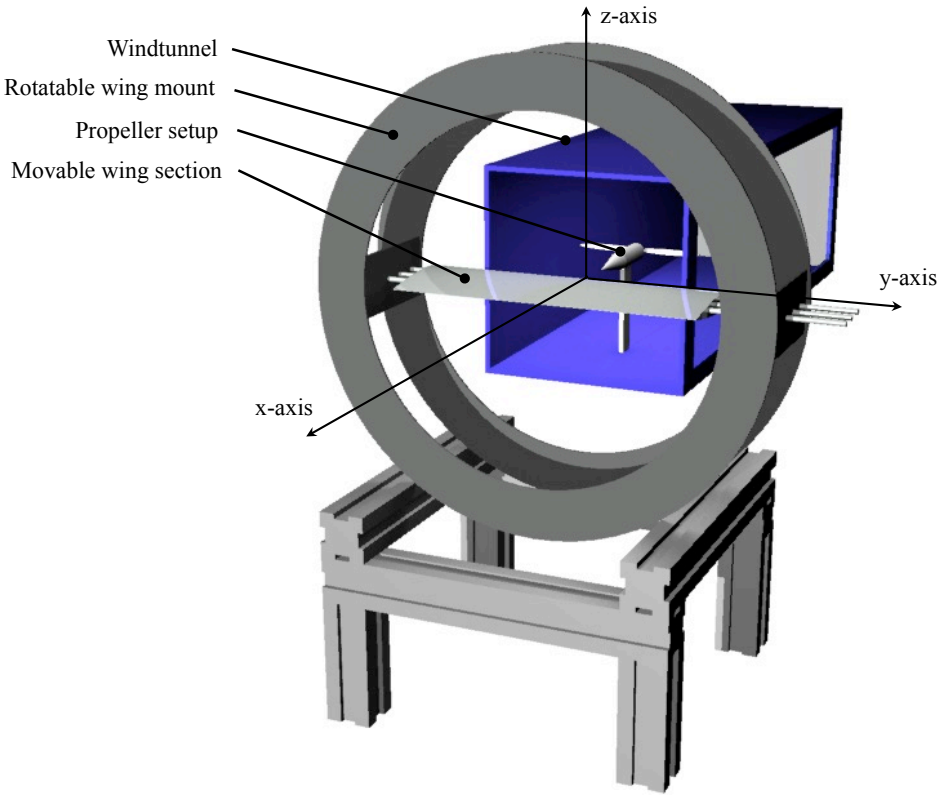

Figure 3.1: Overview of the experimental setup showing the components and reference frame.

The M-tunnel, located in the Low Speed Laboratory (LSL) of the Delft University of Technology, is used to perform the experiment. The tunnel has a 0.4 x 0.4 meter cross section and is operated in an open jet configuration, which allows for a maximum velocity of 35 m/s. A two-bladed tractor propeller driven by an electric motor is connected to a mounting plate, as is shown in figure 3.2a. The mounting plate can be fixed in different locations along the windtunnel floor. The motor and the mounting plate are connected through a support strut containing a load cell, allowing for thrust measurements to be taken. Additionally, an infrared reflective sensor is connected to the propeller support strut which provides the two-pulse-per-revolution trigger signal, i.e. the blade passage signal, which can be used to determine the Rotations Per Second (RPS). The used propeller is an off-the-shelf plastic propeller with a diameter of 0.176m, made by the company Advanced Precision Composites and has the product code LP07040(1). A photograph of the propeller is provided in figure 3.2b.

Two straight, non-tapered, wing sections are used to measure the pressure fluctuations resulting from the vortex impingement. The sections are partially hollow allowing the placement of 9 microphones each that are spaced from leading to trailing edge along the surface centerline. The selected airfoils are the NACA0012 and NACA0016. The different thickness to chord ratios allow for an analysis of the effect of airfoil thickness on the vortex-surface interaction. The absence of camber in the measurement surfaces simplifies the interaction, which in turn reduces the differences between the interaction measured during the experiment and the interaction described by the conceptual model. As the wing chord length of propeller aircraft is generally of the same order as the propeller diameter [9], a measurement surface chord of 0.2m is selected. Seeing that the microphones are spaced in a single line, the measurement surface is moved through the flow in the y-direction (consult figure 3.1) in order to capture pressure fluctuations of the entire flowfield. In order to prevent the surface edge from entering the flowfield as a result from this movement, the span of the surfaces

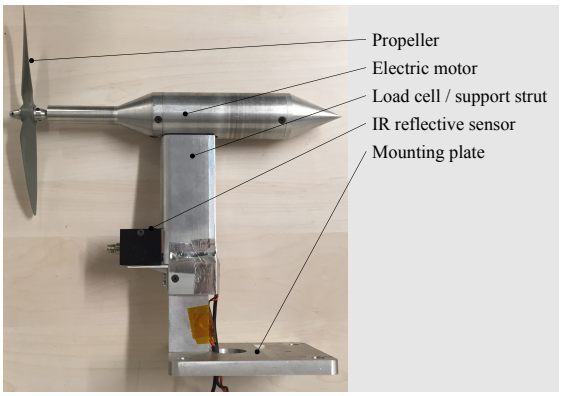

(a) Electric motor, load cell and mounting plate.

(b) Propeller blade.

Figure 3.2: Pictures showing the propeller setup.

was chosen to be 0.6m. Finally, due to limited amount of loading and due to the fact that the measurement surface tip is kept outside of the flow, tip end effects can be neglected. A summary of the measurement surface characteristics are provided in table 3.1.

Table 3.1: Measurement surface characteristics.

Characteristic	Value
Wingspan [m]	0.6
Chord length [m]	0.2
Sweep [°]	0
Taper ratio [-]	1.0
Airfoil [-]	NACA0012 & NACA0016

The wing section model is placed in a mounting system just outside the tunnel opening. The wing mount, shown in figure 3.1, consists of two parts: a circular element in which the wing is mounted, allowing it to move laterally along its y-axis, and a structure on which the circular mount is placed that is level with the windtunnel, allowing the entire circular section to rotate around the x-axis while the wing is locked in place in the mount, as is shown in figure 3.3. For the inclination angle effect to be investigated, the mounting system is aligned so that x- and y-coordinates of the center of the circular mount correspond to the x- and y-coordinates of the vortex core as impinges on the measurement surface.

In order to find the vortex strength and vortex size, a planar Particle Image Velocimetry (PIV) setup is used. The PIV measurements are taken in absence of the measurement surface in order to analyze the vortex strength without any disturbances in the flow. The cameras and laser are positioned outside the flowfield to avoid disturbances that could affect the measurements, while the smoke generator is positioned next to the tunnel inlet. The PIV setup is covered in more detail in section 3.2.3

3.2. Measurement Techniques

During the experiment a number of types of data, namely the thrust generated by the propeller, the fluctuating pressure levels and the flowfield vectors, are measured. In this section the different measurement techniques that are employed to obtain this data are discussed in more detail.

3.2.1. Load Cell

The electric motor driving the propeller is connected to the windtunnel floor through a strain gauge load cell. The data obtained with the load cell allows for an analysis of the propeller performance. The propeller performance is used to determine the test matrix, as described in subsection 3.3. The output of the gauges is fed

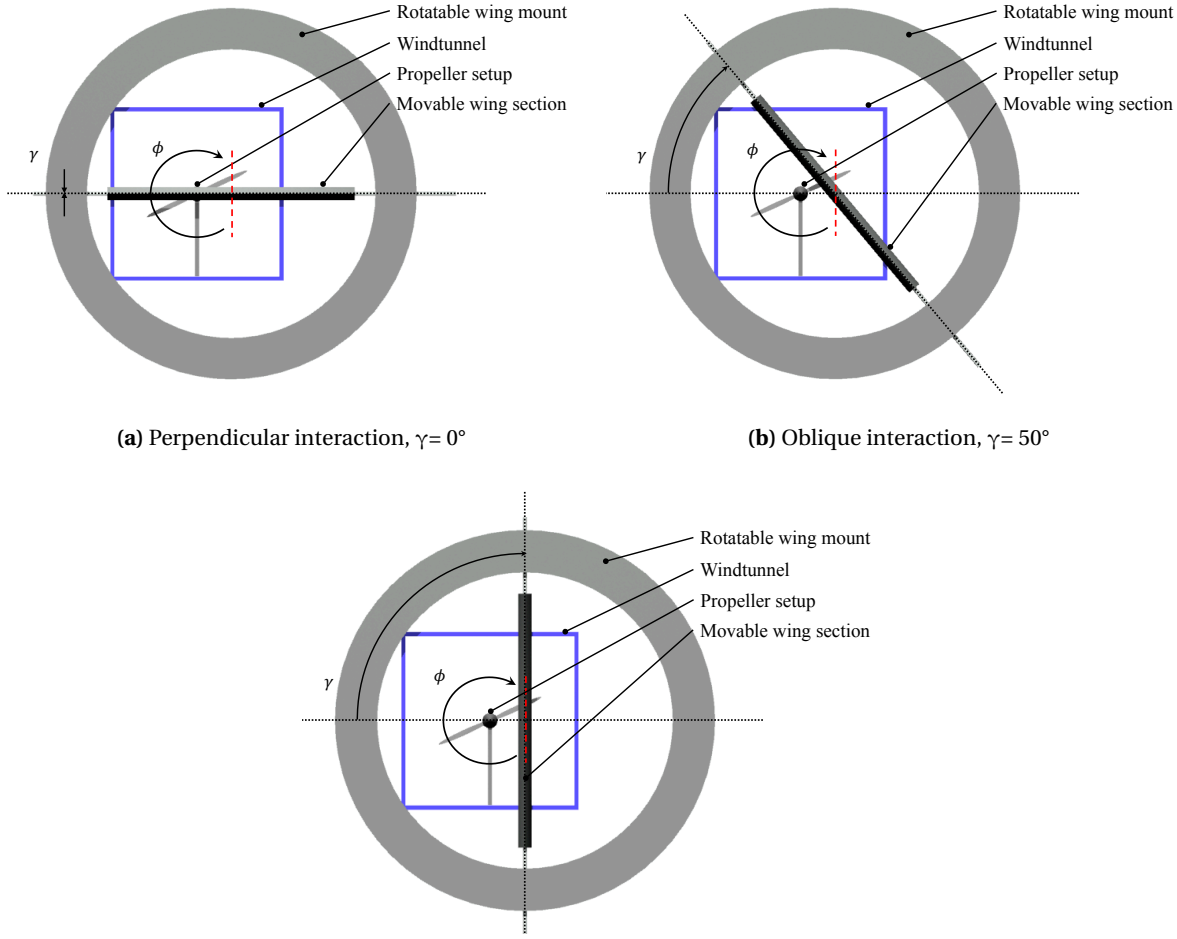

(a) Perpendicular interaction, $\gamma = 0°$

(b) Oblique interaction, $\gamma = 50°$

(c) Parallel interaction, $\gamma = 90°$

Figure 3.3: Aft view of the experimental setup. The dashed red line denotes the propeller tip vortex axis at the location of interaction.

into the GM8802E Weighing Transmitter, which, in combination with the load cell dimensions, determines the force applied in the x-direction. The value was read from the display of the weighing transmitter and recorded by hand. The accuracy of the display is zero decimals and therefore the accuracy of these measurements is ±0.5 gf. The smallest recorded load was equal to 60 gf, leading to a possible error of approximately 1%. An additional indication of the accuracy of the measurements is the sensitivity of the load cell, which ranges from -50 gf to 500 gf.

The force in the x-direction consists of two components, namely the thrust of the propeller in the positive x-direction and the drag on the nacelle and support strut in the opposite direction, as expressed in equation 3.1. Therefore, in order to determine the actual thrust produced by the propeller, the drag component must be determined, which is done by removing the propeller blade from the setup, running the windtunnel and measuring the drag of the support structure.

$$T = T_{on} - T_{off} \tag{3.1}$$

The thrust of the propeller is rewritten to its non-dimensional form in order to make it scalable. Its new form, namely the thrust coefficient, is defined as:

$$C_T = \frac{T}{\rho_\infty \cdot n^2 \cdot D_p^4} \tag{3.2}$$

where ρ_∞ represents the freestream density, n the RPS and D the blade diameter. The propeller performance is evaluated by examining the measured C_T against the advance ratio, J, which is described as:

$$J = \frac{U_\infty}{n \cdot D} \tag{3.3}$$

It should be mentioned that for a constant advance ratio the pitch of the vortex helix is constant. Additionally, for a given propeller design at a constant blade pitch setting, lowering the advance ratio results in a higher perceived angle of attack on the blade and thus in a higher blade loading, provided the propeller is operated outside its stall region.

As the propeller is relatively large with respect to the windtunnel, the windtunnel blockage must be examined to conclude if the blockage effects can be neglected. Seeing that the propeller generates a streamtube of increased velocity flow, V_{prop}, and the windtunnel has a finite cross-sectional area, the conservation of mass dictates that the surrounding flow must have a lower velocity than the upstream freestream flow, V_∞. Glauert [25] has defined that there exists an "equivalent freestream velocity", $V_{\infty,eq}$, at which the propeller not experiencing the blockage effect would provide the same thrust. The correction, based on simple actuator disk theory is provided in equation 3.4:

$$\frac{V_{\infty,eq}}{V_\infty} = 1 - \frac{\left(\frac{T}{\rho_\infty \cdot A_p \cdot V_\infty^2}\right)\frac{A_p}{A_{wt}}}{2\sqrt{1+2\left(\frac{T}{\rho_\infty \cdot A_p \cdot V_\infty^2}\right)}} \tag{3.4}$$

The variables in equation 3.4 are defined as follows: $V_{\infty,eq}$ denotes the equivalent airspeed, A_p and A_{wt} are the propeller disk area and windtunnel area respectively and the term between the parentheses equals an alternative definition of the thrust coefficient, namely one that is non-dimensionalized with freestream density, propeller disk area and freestream velocity. Evaluating the above equation for a propeller to tunnel area ratio of 0.15 and a thrust coefficient in the order of 10^{-1}, the freestream and equivalent airspeed ratio variation is 1.5%. Therefore, we can conclude that for the experiment, $J_{eq} \approx J$.

3.2.2. Surface Microphones

To measure the pressure fluctuations caused by the vortex-surface interactions 9 Sonion 8010T microphones [37] are incorporated in the measurement surfaces. They were positioned on the midline of the measurement surfaces, just below and perpendicular to the surface, with a small cavity connecting them to the flowfield. The microphones are spaced at intervals along the chord, with smaller intervals near the leading edge. A technical drawing of the microphones is provided in figure 3.4a, the chordwise microphone positions on the surface are shown in figure 3.4b. Additionally, the absolute and relative chordwise microphone locations are presented in table 3.2. It is important to note that the microphones are alligned perpendicular to the surace. The frequency range of the microphones is 10 Hz to 11.5 kHz, with a maximum sound pressure level of 112 dB at 1 kHz . The microphones are connected to two National Instruments (NI) 9234 DAQ modules and one NI9215 DAQ module [38][39]. These are in turn connected to the windtunnel computer and processed largely using the LabView software package. Two corrections need to be made to the data due to the use of two different DAQ systems as there was a difference in mean voltage and a difference in phase between the module data. Additional information on these corrections are provided in Appendix A.

The pressure measurements are taken by moving the entire measurement surface through the flowfield in a stepwise manner. The number of steps per measurement was approximately 40. A variable step size is maintained with the smallest step of 1mm applied in the vortex region and the largest of 5mm applied in the freestream and slipstream regions. At a microphone sampling rate of 51.2 kHz, an advance ratio of 0.67, a freestream velocity of 10 m/s and with a measurement time of 20 seconds, which are the baseline measurement characteristics, the number of samples per propeller rotation is 550 and the number of propeller rotations per measurement is 1900. Seeing that the microphones are positioned on one side only, the measurement surface must be removed from the mount and flipped, after which the measurements can be repeated for the opposite side.

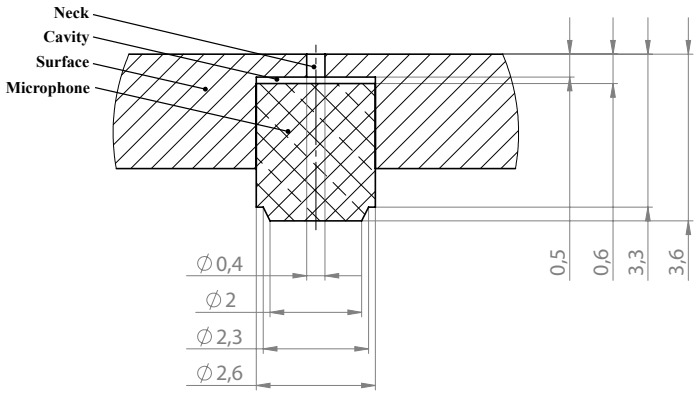

(a) Technical drawing of surface microphone.

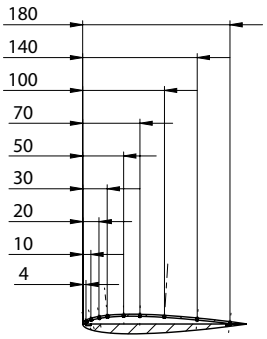

(b) Spacing of surface microphones along the wing chord.

Figure 3.4: Technical drawing of the surface microphone setup. All dimensions are provided in mm.

Table 3.2: Chordwise microphone locations.

Microphone	x [mm]	x/c [-]
1	4	0.02
2	10	0.05
3	20	0.10
4	30	0.15
5	50	0.25
6	70	0.35
7	100	0.50
8	140	0.70
9	180	0.90

A frequency dependent calibration is performed using a LinearX M53 reference microphone, which is in turn calibrated using a GRASS 42AA piston phone at 250 Hz combined with frequency response curves provided by the manufacturer. The calibration was repeated after the experiment and the results indicate a successful calibration. The calibration sequence is discussed in more detail in Appendix A.

An additional check is performed to ensure the eigenfrequency of the cavities is not reached during the experiment. Equation 3.5 is used to determine the eigenfrequency [40]:

$$F_{eig} = \frac{a}{2 \cdot \pi} \cdot \sqrt{\frac{A_{neck}}{V_{cav} \cdot (l_{neck} + l_{corr})}} \tag{3.5}$$

where a represents the speed of sound in air, A_{neck}, l_{neck} the cross-sectional area and length of the resonator neck respectively, V_{cav} the cavity volume and finally, l_{corr} represents the resonator neck end-correction, which can be approximated as $l_{corr} \approx 0.48\, r_{cav}$ [40], where r_{cav} is the resonator cavity radius. The eigenfrequency of the system is found to be 4.6 kHz, which is far above the frequencies of interest and is therefore of no concern. Finally, the data can be phase averaged in order to obtain a view of the data with reduced the fluctuations. The converged solution of the phase averaging, which is further discussed in Appendix A, allows for an effective analysis of the results.

3.2.3. PIV Setup

The vortex strength and size need to be determined to be able to compare the data generated by the model with the experimentally obtained data. It is also useful to examine the flowfield in order to investigate if the vortices are coherent for certain propeller settings. Particle Image Velocimetry is employed to do so. An overview of the PIV setup and the location and dimensions of the planar Field Of View (FOV) with respect to the measurement surface and tunnel is shown in figure 3.5.

A high-resolution image is preferred but simultaneously the FOV must be large enough to capture a sufficient part of the flowfield. Therefore, the choice is made to use two LaVision Imager Pro LX (16 Mpx) cameras with 200 mm Nikon AF lenses and to stitch the fields together in post-processing. This type of CCD camera has a 4872 x 3248 px sensor with a pixel size 7.4 μm and a pixel aspect ratio of 1. The laser sheet is produced by a Quantel Evergreen laser, which is of the Nd:YAG type and has a pulse energy of 200 mJ. The tracer particles are generated by a SAFEX Twin Fog DP smoke machine with SAFEX-Inside-Nebelfluid consisting of dyethelene-glycol and water, located at the tunnel inlet. The tracer particles have a size in the order of 1 μm and a relaxation time of 1 μs. The laser and cameras are synchronized using a LaVision Programmable Timing Unit (PTU). The software used to process and store the obtained data is the LaVision Davis v8.3 software package. The PIV processing done with the software is further covered in Appendix A. The images are taken in a phase locked manner and 300 images are taken per measurement. The characteristics of the PIV measurements are summarized in table 3.3.

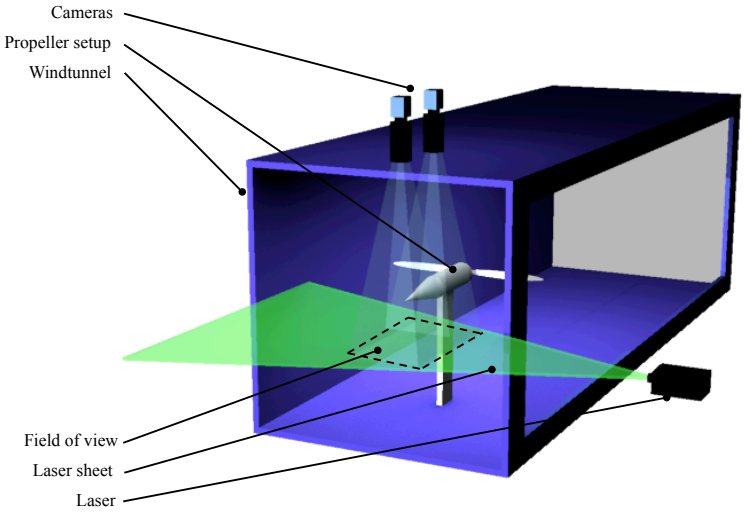

(a) Overview of the PIV setup

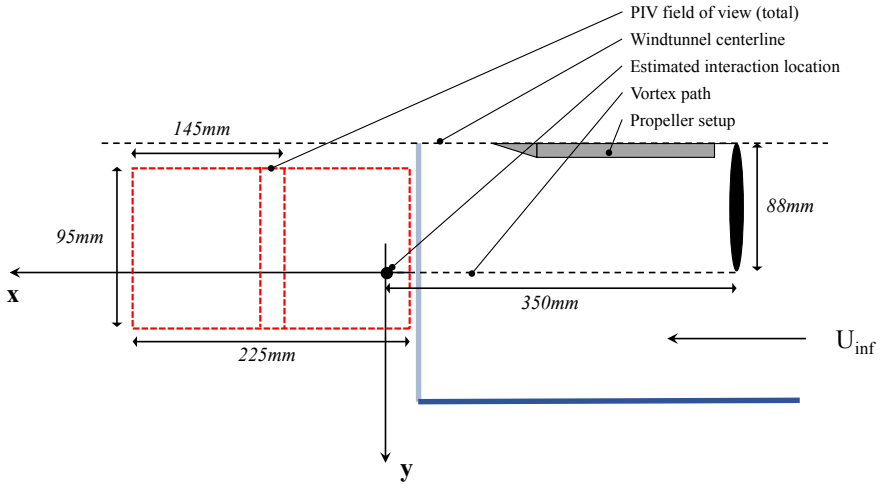

(b) Schematical representation of the PIV setup, top view

Figure 3.5: Setup of PIV system during the experiment.

Table 3.3: Planar PIV setup characteristics.

PIV characteristic	Value
Acquisition rate [Hz]	0.7
Focal length [mm]	200
Magnification [-]	0.11
Field of view, per camera [mm^2]	145 x 95
Field of view, total [mm^2]	225 x 95
Pulse delay [μs]	50
Freestream pixel shift [px]	14
Image resolution [px/mm]	34
Window size [px^2]	24 x 24
Overlap factor [%]	50
Vector spacing [mm]	0.4

3.3. Test Conditions

The propeller slipstream was examined for windtunnel velocities of 5, 10 and 15 m/s and advance ratios between 0.35 and 0.9. From the microphone and PIV data it was apparent that for advance ratios below and freestream velocity values above a certain threshold, instabilities in the flowfield occurred: the location and strength of the propeller tip vortex was found to differ per blade, as can be observed in figure 3.6. The source of these instabilities could not be determined but seeing that the propeller blade is an off-the-shelf model, it may simply be due to asymmetry in the blades or blade deformation during operation. It was concluded that for an advance ratio between 0.6 and 0.7 and a windtunnel velocity range of 10 to 15 m/s the propeller wake was coherent and clearly structured, without the presence of the aforementioned fluctuations.

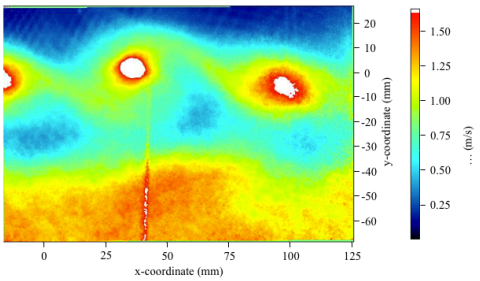

(a) $V_\infty = 10\ m/s$, $J = 0.54$, $RPS = 105\ Hz$.

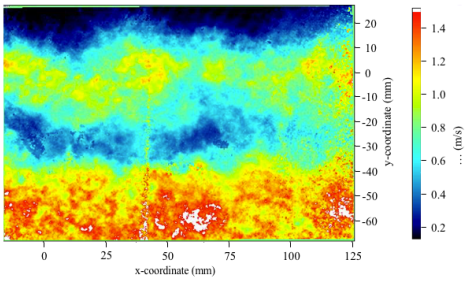

(b) $V_\infty = 10\ m/s$, $J = 0.43$, $RPS = 132\ Hz$.

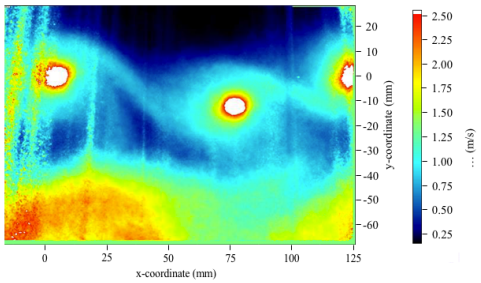

(c) $V_\infty = 15\ m/s$, $J = 0.55$, $RPS = 143\ Hz$.

Figure 3.6: Examples of flow instabilities for a number of advance ratios and windtunnel speeds.

The selected advance ratio range was checked by examining the corresponding $C_T - J$ curve. The curve provides an indication of the propeller performance and was constructed using the measured loading data. The curve shows a clear linear behavior over its entire range, indicating that for the selected operating regime,

Table 3.4: Parameters of the different experimental cases.

Case	RPS [Hz]	V_∞ [m/s]	Advance ratio [-]
1	95	10	0.60
2	85	10	0.67
3	127	15	0.67

i.e. a freestream velocity of 10 m/s and an advance ratio between 0.6 and 0.7, no flow separation occurs over the blades. The final selection of considered test cases is shown in table 3.4. It should be noted that the small difference in range of advance ratios is not optimal for the validation of the conceptual model, since the effect of such a small difference might not be clearly visible for certain analyses.

Due to the geometry of the windtunnel, a limited choice of propeller location was available. The windtunnel floor panel included 3 locations to mount the propeller setup, namely at approximately 4, 5 and 6 propeller diameters, D_p, from the propeller plane. Interactions between propellers and wings / pylons are generally studied at between 0 and 1 D_p distance [9]. As the goal of the experiment is to validate a relatively fundamental aerodynamic model, this was not considered to be a problem. At 4 D_p a coherent and stable vortex structure was observed in the PIV data while at 5 and 6 D_p the vortex structure became less coherent. Therefore, a propeller location of 4 D_p was selected.

The angle of attack of the measurement surface is kept at 0 degrees throughout the experimental campaign. Although the conceptual model contains an angle of attack variable, the addition of a non-zero angle of attack would create more complex aerodynamic phenomena and thus complicate the interpretation of the test results. The effect of the incidence angle of the wing with respect to the x-y-plane, as shown in figure 3.3, is investigated with a step size of 10 degrees. The 50 degree incidence angle position could not be measured due to mechanical interference between the two elements of the wing mount. The complete test matrix is presented in table 3.5.

Table 3.5: Parameters of the test matrix.

Parameter	Value
Airfoil [-]	[NACA0012 NACA0016]
Case	[1 2 3]
Surface [-]	[Advancing Retreating]
Incidence angle [°]	[0 10 20 30 40 60 70 80 90]

Seeing that the experimental data is used to validate the conceptual model, the same Reynolds number needs to be used as input for the model. We find a Reynolds number of $1.28 \cdot 10^5$ at the windtunnel operating speed of 10 m/s, given that the characteristic length, L, and kinematic viscosity, ν, are equal to 0.2 m and $15.1 \cdot 10^{-6}$ m^2/s respectively. In comparison, the Reynolds number of a standard turbopropeller driven aircraft, such as the Fokker F50, is approximately equal to $3.1 \cdot 10^7$ [41]. This is a significantly higher value and will result in different flow characteristics, but as explained in previous Chapters, the goal is to study a fundamental vortex surface interaction, not to simulate a situation that is applicable in the aerospace industry.

4

Conceptual Model

This chapter covers the development of the conceptual model, which is done using the theoretical background discussed in Chapter 2. Conceptual models can be constructed in multiple ways and can be used for multiple purposes. In this case the conceptual model consists of a simplified version of a phenomenon that is not fully understood and contains certain aspects of the phenomenon, or 'sub-phenomena', and neglects others. The goal of the development and use of such a conceptual model is to study the relative contribution of the gain insight into its workings. The approach taken to develop the model, the assumptions that are made and the resulting model are discussed in this chapter.

In section 4.1 the approach taken to develop the model will be discussed. The criteria used to select the model components and the subsequent analysis of the components using these criteria will also be provided. Thereafter an in-depth explanation of the different model components and corresponding assumptions is provided in section 4.2. This section also contains a discussion on the expected discrepancies between the model and experimental results. For the verification of the model, see Chapter 5.

4.1. Model Development

There are many different methods to construct a conceptual model describing the vortex-surface interaction and all employ different levels and methods of abstraction that achieve the goal of simulating the pressure fluctuations as a result of the vortex-surface interaction. The underlying design principles and the approach used in this case is described in this section.

4.1.1. Approach

As described in Chapter 1, the goal of the project is twofold. Firstly, to facilitate noise mitigation through a better physical understanding of the propeller tip vortex-surface interaction. Secondly, the development of a tool that would allow noise mitigation to be taken into consideration during the early design phase. The model being developed is the first version and the decision is therefore made to model the most basic and fundamental interaction. By assessing such model will provide an indication on the quality and accuracy of the chosen approach. If proven accurate, further iterations can be performed to create a more complex model that more closely represents the interaction.

A fundamental propeller tip vortex surface interaction looks as follows: a non-cambered, well-studied airfoil without high lift devices is placed under a zero degree angle of attack in a constant flow. By doing so the wing loading is minimized resulting in the most basic pressure distribution over the wing. Ideally, the vortex is simulated as a single vortex perpendicular to the surface. However, due to limitations posed during the design of the experimental campaign, the generation of such a fundamental vortex proved was not possible. Therefore, a propeller is modeled at a significant distance with respect to the surface that generates multiple vortices under a pitch angle dependent on the flow speed and propeller setting. The assumption is made that by distancing the propeller from the surface the vortices are fully formed and there is less effect of the wake and can therefore be neglected.

As described in Chapter 2, the vortex surface interaction phenomenon can be broken down into a number of sub-phenomena or 'components'. The underlying assumption is made here that the individual components are independent of one another. This assumptions allows the summation of multiple components without taking into account the effects of excluding others. The limitations posed by this approach can be described with an example: given the above mentioned assumption, the model could contain the viscous interaction between the boundary layer and the vortex, which will dissipate the local energy is and is therefore make the vortex more susceptible to spanwise movement. Due to the assumption, however, the expected increase in vortex shearing does not occur.

The next step is to select what components to include. In doing so a number of aspects should be considered, the first being that some components have a smaller impact on the pressure fluctuations generated during the interaction than others. In order to simplify the model but simultaneously keep the effects of the interaction as close to reality as possible, the components with a larger impact on the pressure fluctuations should therefore have a preference during the selection process. If possible, the contribution of the individual component will be quantified in order to make an justified selection.

The second aspect that must be taken into account is the level of scientific knowledge available on each of the components. The reason therefore is that without the proper level of physical understanding the components cannot be accurately modeled. If few studies have been performed on a certain topic it complicates the task at hand. Clearly this criterion is hard to quantify and it will largely be up to the judgment of the student. Another aspect of this criterion is the amount of time required to model the component. There is a limited amount of time available to complete the project and the selection on the components will be dependent on the time requirements. This to is hardly quantifiable and left to the judgment of the student.

Finally, it is imperative to validate the results of the conceptual model in order to successfully achieve the research objective. To do so each component of the conceptual model must be validated individually. Ideally the experimental campaign would be designed so that the data required to validate the components deemed important to the accuracy of the model is collected. However, this was not possible seeing the order in which the project was performed. Seeing the importance of this criterion and the fact that there is only certain data available, this criterion can considered a 'hard' criterion, meaning that if a sub-component cannot be individually validated it is excluded from the model.

The following criteria will be employed when evaluating the model components:

1. *Impact*; how large is the contribution of the component to the total pressure fluctuation.

2. *Understanding*; how well can a the component be modeled from the available scientific literature.

3. *Comparability*; to what extent can the component be validated using the available experimental data.

4.1.2. Component Assessment and Selection

Applying the criteria covered in the previous sub-section to the components discussed in Chapter 2 a conclusion can be drawn on what components will be contained in the model. Each component is discussed independently according to each criterion:

1. *Vortex pressure*; the pressure generated by the low pressure in the vortex core is expected to be the largest contributor to the resulting pressure fluctuations on the downstream aerodynamic surface. This phenomenon has been thoroughly studied and is well understood. The experiment has been set up in such a way that the vortex characteristics needed to model it, such as the circulation and core size, are known.

2. *Induced angle of attack*; although no in-depth studies have been performed on the topic of the induced angle effect, it can be analyzed. Some assumptions will be necessary to model the component however. At low mach numbers and lightly loaded airfoils, as is the case for the experiment, the effect of the induced angle of attack is expected to be relatively low. Additionally, the effect of the induced angle of attack effect has been measured indirectly through the pressure measurements.

3. *Vortex shearing*; a number of studies have shown the existence of this phenomenon and quantified the actual movement of the upper and lower surface vortex filament movement. The effect is expected to be significant, not in the sense of the pressure fluctuation magnitude but in its distribution over the surface. Finally, seeing that the pressure fluctuations have been measured over a number of x- and y-coordinates, the effect of shearing can be compared with the conceptual model results.

4. *Boundary layer-vortex interaction*; although the boundary layer of airfoils has been thoroughly studied, the effect it has on a vortex is not, making it hard to correctly model. The impact is expected to significantly affect the vortex strength at the surface as the vortex travels along the chord [ref:]. The measure of viscous interaction has been measured indirectly through the pressure fluctuation measurements.

5. *Vortex bending*; although the general characteristics for this phenomenon as well as the conditions under which it is likely to occur have been studied, the actual impact on pressure fluctuations has not yet been quantified. This fact, in combination with the complexity of the phenomenon makes it difficult to correctly model. Additionally, no specific measurements have been performed to quantify or visualize the vortex bending during the experiment. However, the impact of the component on the pressure fluctuations is expected to be be significant.

6. *Vortex stretching / compression*; similar to the vortex bending, the effect of vortex stretching / compression is has not been thoroughly studied nor has it been quantified. Furthermore, the effect is expected to be limited and no measurements were performed during the experiment to visualize or quantify this particular component.

From the analysis the vortex pressure and the induced angle of attack effect have been chosen to be contained in the conceptual model. A more in-depth explanation of the modeling of the components is provided in section 4.2.

4.2. Modeling of Individual Components

In this section the individual components that make up the conceptual model are discussed. The theoretical background of the components has been discussed in Chapter 2. Here the manner of implementation of the components and the assumptions that are made are discussed.

4.2.1. Vortex Pressure

In order to model the vortex pressure, two assumptions are made. Firstly, incompressible flow is assumed, which can be considered correct for the range of Mach numbers under consideration. Secondly, the tangential velocity distribution of the vortex is modeled using the Lamb-Oseen vortex model. Using the first assumption the vortex pressure can be determined by integrating Bernouilli's law for curved flow, the equation for which is expressed in Chapter 2 (eq. 2.4).

In order to obtain the tangential velocity distribution as a function of radial position, one could use the PIV data obtained during the campaign. However, due to the centrifugal forces the particle density within the core of the vortex is too low for the velocity distribution inside the core to be correctly determined with this method. Therefore, the assumption is made that the tangential velocity distribution behaves according to the Lamb-Oseen vortex model [14]. This is a widely used method for modeling vortices that takes into account the degradation of the vortex due to diffusion. The Lamb-Oseen model is described with equations 2.5, where r_c is the core radius as a function of vortex age t and kinematic viscosity ν, and 2.6, where Γ is the vortex circulation and r the radial distance to the vortex center.

In order to model the vortex pressure, the vortex age and circulation must be known. The vortex age can be determined using the distance between the propeller and the measurement surface and assuming the vortex propagates with the freestream flow velocity. The circulation of the vortex is obtained using the PIV data. First, the location of the vortex center is determined using the vorticity information obtained from post-processed PIV data. Then the diameter of the vortex, defined as the distance between the peak tangential velocities of the vortex, is calculated. Finally, the circulation of the vortex is determined by integrating the tangential velocity along the circumference of the vortex, as defined in equation 4.1.

$$\Gamma = \oint_C \vec{u} \cdot \mathrm{d}\vec{l} \tag{4.1}$$

Having obtained the circulation and vortex age, the vortex pressure can be determined with equation 2.4 for all x- and y-locations for all vortex ages. Finally, the pressure coefficient is obtained according to equation 4.2. Making the pressure dimensionless allows for the model components to be added together and allows for comparison between the different experiments.

$$C_p = \frac{p - p_\infty}{{}^1/_2 \cdot \rho_\infty \cdot V_\infty^2} \tag{4.2}$$

An example of the resulting tangential velocity distribution and corresponding pressure distribution is presented in figure 4.1. As can be observed, the vortex travels in the positive x-direction, which is downstream. The absolute value of the velocity distribution is shown which is used to determine the pressure distribution.

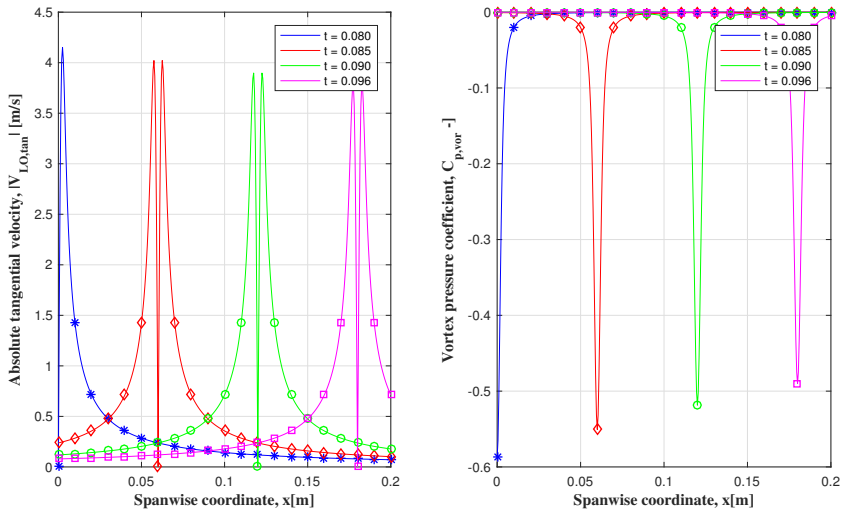

Figure 4.1: Example of absolute tangential velocity distribution, $V_{LO,tan}$, and the vortex pressure coefficient distribution, $C_{p,vor}$, of a Lamb-Oseen vortex. The governing characteristics are $t = 0.08$ $[s]$ and $\Gamma = 0.09$ $[m^2/s]$.

4.2.2. Induced Angle of Attack

As is explained in Chapter 2, the vortex is orientated at an angle equal to the pitch of the helical vortex structure, which causes a velocity component in the z-direction $V_{ind,z}$ to occur in addition to the induced velocity in the x-direction $V_{ind,x}$. As shown in figure 4.2, the direction of induced velocity components depends on the location relative to the vortex, i.e. in- or outboard of the vortex. These components, in combination with the baseline velocity in the x- and z-directions, $V_{base,x}$ and $V_{base,z}$ respectively, create a total velocity V_{tot} and angle of attack α, as shown in figure 4.3. As a result, the vortex causes a time dependent change in pressure distribution over the airfoil that differs at each y-location of the airfoil.

To model the induced angle of attack effect it is assumed that the induced pressure depends on the angle of attack and flow velocity at the leading edge of the surface. The goal was to do a two-dimensional analysis of the basis of strip theory, in order to minimize the runtime of the model. The assumption causes the vortex to have a larger upstream effect than would be realistic, as the pressure distribution over the entire airfoil is dependent on the flow conditions at the leading edge. Although this is a significant simplification, the fact that the influence of the vortex on the induced pressure is largest when it is close to the leading edge is captured in this manner.

The induced pressure is determined at all x- and y-coordinates over the surface for each vortex age using Xfoil [42], which is a numerical flow solver based on a panel method with a Karman-Tsien compressibility correction. The inputs of Xfoil are the Reynolds number, Mach number, angle of attack and the x- and y-coordinates of the airfoil contour. The results of Xfoil are provided as both upper and lower surface total

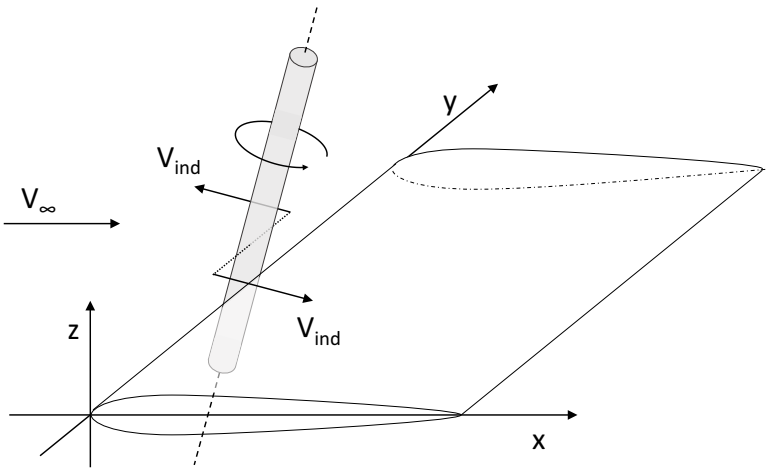

Figure 4.2: Schematic representation of velocity components induced by vortex.

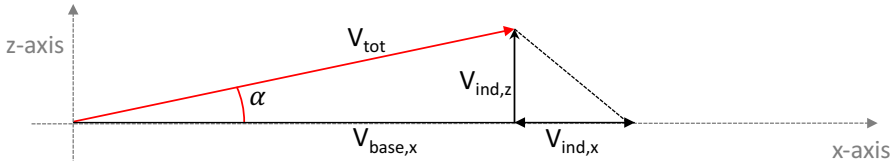

(a) Outboard of vortex

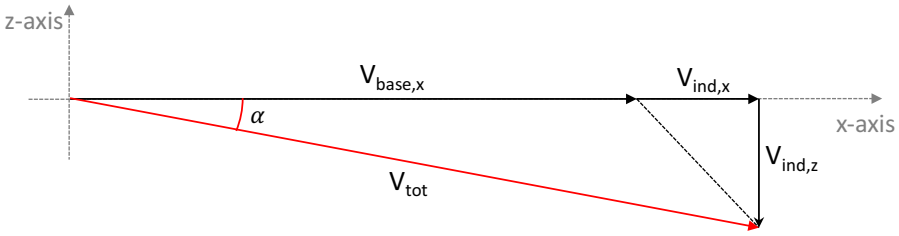

(b) Inboard of vortex

Figure 4.3: Schematic representations of the individual baseline and induced velocity components and the resulting total velocity component and angle of attack.

pressure coefficient distribution with one data point for each airfoil contour x-coordinate. In order to obtain the same resolution as that of the experiment, the data is interpolated to the corresponding x-coordinates.

4.2.3. Baseline Pressure Distribution

As is discussed in the previous subsection the induced angle of attack effect is determined in terms of the total static pressure, while the value that is required is the change in static pressure, i.e. the unsteady pressure. Seeing that during the experiment the pressure fluctuations were measured instead of the static pressure, the mean or 'baseline' pressure needs to be subtracted from the pressure fluctuations caused by the induced angle of attack. This allows for comparison between the results of the conceptual model and the results of the experiment. As mentioned in the previous subsection, the pressure distribution over the airfoil is determined by the angle of attack and the Mach number of the flow at the leading edge, the flow conditions and the airfoil shape. The latter two, the airfoil shape and flow conditions, are known and differ per test case. The angle of attack and the Mach number, however, change along the y-axis and need to be determined.

It is assumed that the steady flow at the wing leading edge consists of two velocity components, one in the x-direction and one in the z-direction. The first is a result of the combined axial velocity increase generated by

the propeller and the freestream velocity. The baseline velocity component in the x-direction is determined using the PIV data obtained from the experiment, as shown in figure 4.4a. For each grid y-coordinate the velocity vectors in the x-direction, $V_{PIV,x}$, between two vortices was plot and the inflection point of that plot was determined. The assumption is made that the baseline flow speed is equal to the velocity in the x-direction at that inflection point seeing that the vortex induces an additional velocity component. On the outboard side the component is in the negative x-direction, so the baseline velocity will be the largest velocity at those y-locations. Inboard of the vortex, the component is positive and therefore the baseline velocity will be the smallest velocity at those y-locations. An example of this method is provided in figure 4.4b.

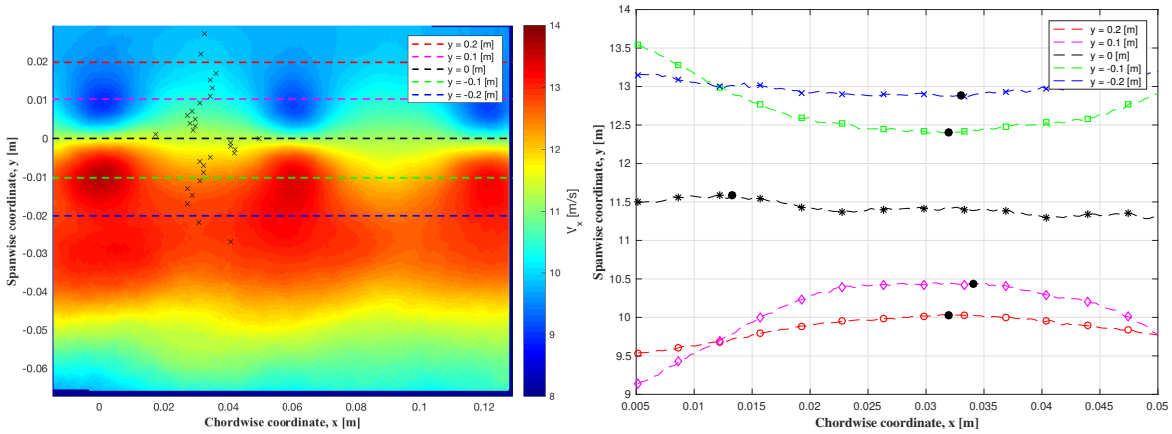

(a) Example of a contourplot of the $V_{base,x}$ velocity vectors. The black crosses indicate the locations at which the $V_{base,x}$ values are determined.

(b) Example of a plot of the $V_{base,x}$ velocity component at a number of y-locations.

Figure 4.4: Elaboration of method used to determine the baseline flow velocity, $V_{base,x}$ at each y-location. The dotted lines in figures 4.4a and 4.4b correspond to one another.

There are a number of methods to determine the down- or upwash distribution in the slipstream due to the swirl of the flow during the experiment. A PIV measurement could have been done to determine the velocity component in the z-direction. However, from the PIV measurements that were made, namely planar PIV measurements in the x-y-plane, it was not possible to extract the velocity component in the z-direction. Another method is to analyze the swirl of the flow by making use of a Blade Element Method analysis of the propeller blade used during the experiment. To do so, the geometry of the propeller blade used during the experiment, namely the APC Free Flight 7x4, must be known. However, neither the website of the manufacturer nor scientific literature on the topic of model propeller blades contain the required information. The blade geometry could be measured, however this is a time consuming and inaccurate method. The assumption is therefore made that the propeller slipstream velocity component in the z-direction has a negligible impact on the results.

4.2.4. Finalizing Model

With the model inputs defined and the contributions of the individual components determined, the unsteady pressure coefficient C'_p can be obtained following equation 4.3:

$$C'_p = C'_{p,vor} + (C'_{p,ind} - C_{p,base}) \tag{4.3}$$

where $C'_{p,ind}$ is the unsteady vortex pressure coefficient adjusted for shearing and boundary layer-vortex interaction, $C'_{p,ind}$ is the unsteady induced pressure coefficient and $C_{p,base}$ the baseline pressure coefficient. Additionally, the effect of multiple vortices can be simulated by simply adding a number of vortices corresponding to the number of blades of the propeller was used during the experiment. The unsteady pressure coefficient at all x- and y-coordinates for all phase angles is then available.

4.2.5. Model Inputs and Outputs

The above mentioned components are modeled in Matlab. The script requires a number of inputs and generates a number outputs. For clarity it is useful to list these here.

Firstly, the case independent parameters, such as the propeller blade characteristics, distance between propeller and measurement surface and fluid properties, are required. Secondly, the test case dependent parameters are required. These test condition characteristics contain such values as the freestream velocity and RPS. Thirdly, the x- and y-coordinates of the required data points must be specified. In order to obtain an output from the conceptual model that can be compared with the experimental campaign, the chosen x- and y-coordinates are the same as those used during the experiment. Similarly, the phase steps with which the analysis is performed are equal to 1 degree, as is the case for the experimental data processing. These aspects are explained further in Chapter 3. Finally, the vortex path must be defined. The x-location is defined as a function of the tunnel freestream velocity and phase. Seeing that vortex shearing is not one of the aspects of the vortex surface interaction that is under investigation, the y-location of the upper and lower vortex filaments are equal and set to zero deviation from the vortex centerline.

The output of the model is as follows: for a phase of $0-2\pi$, the total unsteady pressure coefficient, i.e. the sum of the individual components, is available at each data point. Finally, the model must be run for the same set of test conditions as the experiment in order to be able to fully validate the model. The test matrix in question is discussed in Chapter 3.

III

Results and Discussion

5

Verification and Data Quality

In section 5.1 the quality of the data obtained with the various measurement techniques, namely the surface microphones, PIV setup and the load cell, is evaluated. Then the results of the conceptual model need to be verified. For the verification of the conceptual model a qualitative approach will be taken, as is explained in section 5.2. With these steps taken the results can be presented, which is done in Chapter 6.

5.1. Experimental Data Quality

During the experiment a number of measurement techniques were employed to obtain the required data. Evaluating the quality of the data will remove a measure of uncertainty during the assessment of the conceptual model in Chapter 6. For each measurement technique a different approach is employed to determine the accuracy; the background noise of the surface microphones are evaluated, an uncertainty analysis is applied to the PIV data and the propeller thrust data is assessed by analyzing the propeller performance plot.

5.1.1. Background Noise

The quality of the surface microphone measurements is evaluated by examining the background noise levels. In order to do so, the sound pressure levels experienced by the measurement surface in the vortex impingement region were measured for three setups. The first, namely the *propeller on* setup is identical to the setup with which the rest of the experiments was performed. The measurements for this setup were taken in the vortex interaction region, between $0.9 - 1.1$ y/R. For the second, the *propeller off* setup, the propeller was removed and the electric motor was left off during the measurement. Finally, for the *windtunnel off* setup, the tunnel was turned off but the cooling pump was left on. Additionally, in order to evaluate the effect of the windtunnel velocity, the three measurement setups were examined for freestream velocities 10 m/s and 15 m/s at an advance ratio of 0.67. To investigate the effect of the measurement surface on the background noise the analyses were performed with both the NACA0012 and NACA0016 wings.

From the results a number of observations can be made. There is a distinct difference in Frequency Pressure Level between the propeller on and propeller off measurements. These differences are largest the low frequencies of the spectrum, which indicates that at these frequencies the differences are likely due to the propeller noise. The background noise measurements were are taken in the vortex region, which explains the large differences. The main peaks in the low frequency region correspond to the blade passage frequency, which for this case (RPS = 95, 2 bladed propeller) is 190 Hz, and its multiples, at 380 Hz, 570 Hz, etc. Additionally, there are smaller peaks at the propeller rotation frequency and its multiples, indicating there are some differences between blades. This discrepancy has been mentioned in Chapter 3 and is further confirmed here. Additionally, there are two peaks at approximately 6 and 12 kHz. Seeing that these peaks occur well outside the propeller frequency range and are not visible in the tunnel off setup, the most likely source is the tunnel itself. Finally, the difference between the tunnel on and tunnel off setups is very large. The M-tunnel in which the experiment is performed is a very loud tunnel. Finally, when comparing the background noise plots of the different test cases and wings, as provided in Appendix **??**, it can be concluded that there are no significant differences between the results.

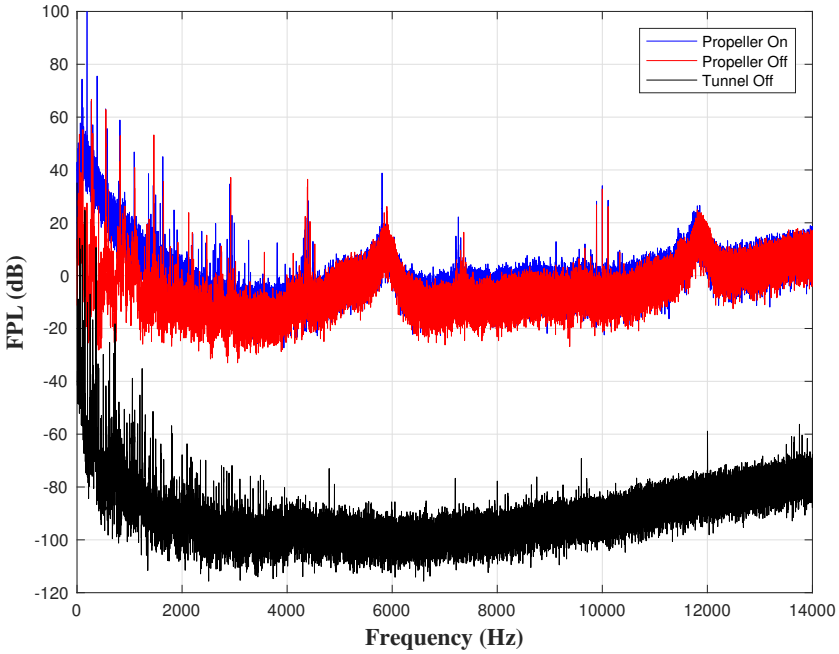

Figure 5.1: Background noise levels for the different measurement setups. y/R = 0.9[−], $J = 0.67$, $V_\infty = 10\ m/s$ and NACA0012

5.1.2. Uncertainty Analysis

The accuracy of the PIV data is assessed by performing an uncertainty analysis on the measurement data. This method consists of examining the individual contributions of the existing uncertainty factors for planar PIV measurements: peak-locking, intantaneous velocity error and mean velocity error. Peak-locking, which is also referred to as pixel-biasing and pixel-locking, results from the tendency for the measured displacement and location of the particles images to be biased to integer values. This occurs when the size of the particle images is smaller than or of the same order as as the pixel size [43]. Peak-locking can be examined by plotting the round-off error of the pixel displacement. If peak-locking indeed occurs during the measurements, one would expect the round-off error distribution to peak at zero.

A peak-locking analysis is performed on the axial component of the PIV measurement performed at $V_\infty = 10\ m/s$ and $J = 0.6$, for which the results are provided in figure 5.2. We find that peak-locking does not occur as the round-off error peaks at 0.2. The peak likely results from the fact that the a significant part of the field of view lies in the freestream region, where there exist a large number of vectors indicating the same displacement.

Instantaneous velocity errors are related to the accuracy of the cross-correlation process. A value of ≤ 0.1 pixel is usually maintained for this accuracy [44]. Using the pulse delay dt and the digital magnification factor M_{pix} the pixel error can be related to the velocity error:

$$\epsilon_V = \frac{\epsilon_{pix}}{M_{pix} \cdot dt} \tag{5.1}$$

Although a large number of images were used to average the velocities and remove random fluctuations, a *mean velocity error* still exists in the values obtained from the measurements. An estimate of this error is possible using equation 5.2 [45], where σ_U is the standard deviation of the velocity component V and N is the number of images taken.

$$\epsilon_{V,mean} = \frac{\sigma_V}{\sqrt{N}} \tag{5.2}$$

The same method can be applied to the remaining velocity component. Additionally, it should be noted that the error is highly dependent on where the error is examined within the flowfield, as the regions with high

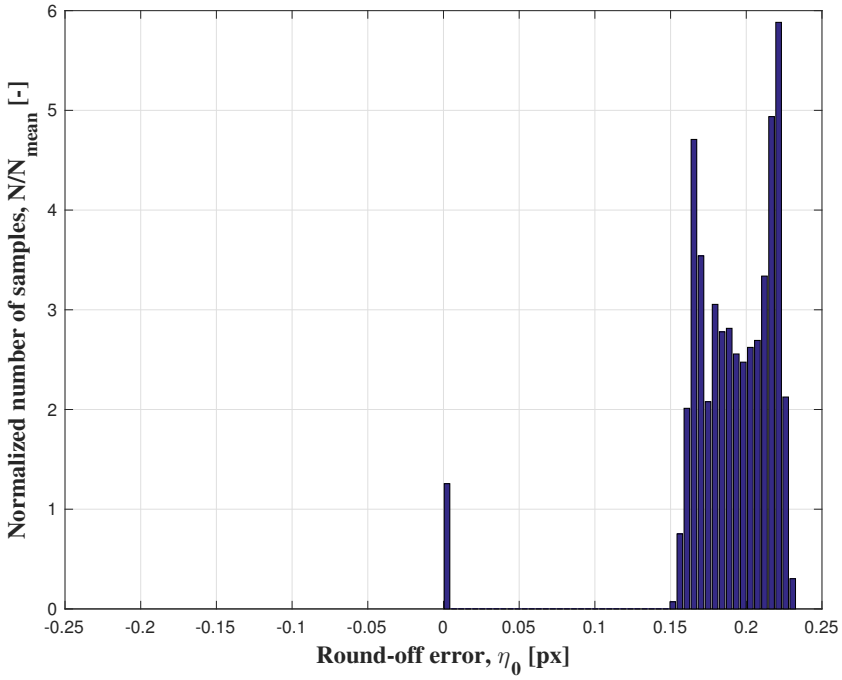

Figure 5.2: Round-off error distribution of the axial displacement component of the planar PIV measurements, for $V_\infty = 10 m/s$, $J = 0.6$, $y/R = 0.96$.

turbulence, such as the tip vortex region, will be significantly higher than the error in non-turbulent regions, such as the freestream. The results of the instantaneous and mean velocity error analyses are provided in table 5.1. It can be concluded that the velocity errors are less than 1.5% of the freestream velocity.

Table 5.1: Instantaneous and mean velocity error values of the planar PIV measurements. ($J = 0.6$, $V_\infty = 10 m/s$)

Region		Absolute	Relative
	ϵ_v $[m/s]$	0.121	1.2%
Slipstream	$\epsilon_{U,mean}$ $[m/s]$	0.018	0.2%
Vortex	$\epsilon_{U,mean}$ $[m/s]$	0.027	0.3%
Freestream	$\epsilon_{U,mean}$ $[m/s]$	0.008	0.1%

5.1.3. Propeller Performance Analysis

To assess the accuracy of the thrust measurements, the propeller performance is examined by plotting the thrust coefficients over a range of advance ratios for different windtunnel velocities. Ideally, the results would present a single linear curve, indicating that the propeller performance is equal for all windtunnel velocities and the thrust coefficient and advance ratio are linearly related.

The propeller thrust was measured for windtunnel velocities of $5-25$ m/s with a 5 m/s step size, for which the results are presented in figure 5.3. The steps in advance ratio correspond to a 5 gram force step size in thrust measurement. Additionally, the advance ratio range for each measurement has a lower limit set by the fact that no negative thrust values were measured. The upper limit is set by the maximum voltage and current of the engine driving the propeller. From the plots it can be observed that both the slope and the offset of the curves is different for each measurement set. Due to the difference in minimum and maximum measured advance ratio per set, the relative offset of the curves cannot be compared. The gradients of the curves can be compared however. The gradient values and percentage deviation from the mean are provided in table 5.2.

From table 5.2 it can be concluded that the slope becomes larger with an increase in windtunnel velocity. This corresponds to an increase in propeller performance seeing that for the same decrease in advance ratio, i.e.

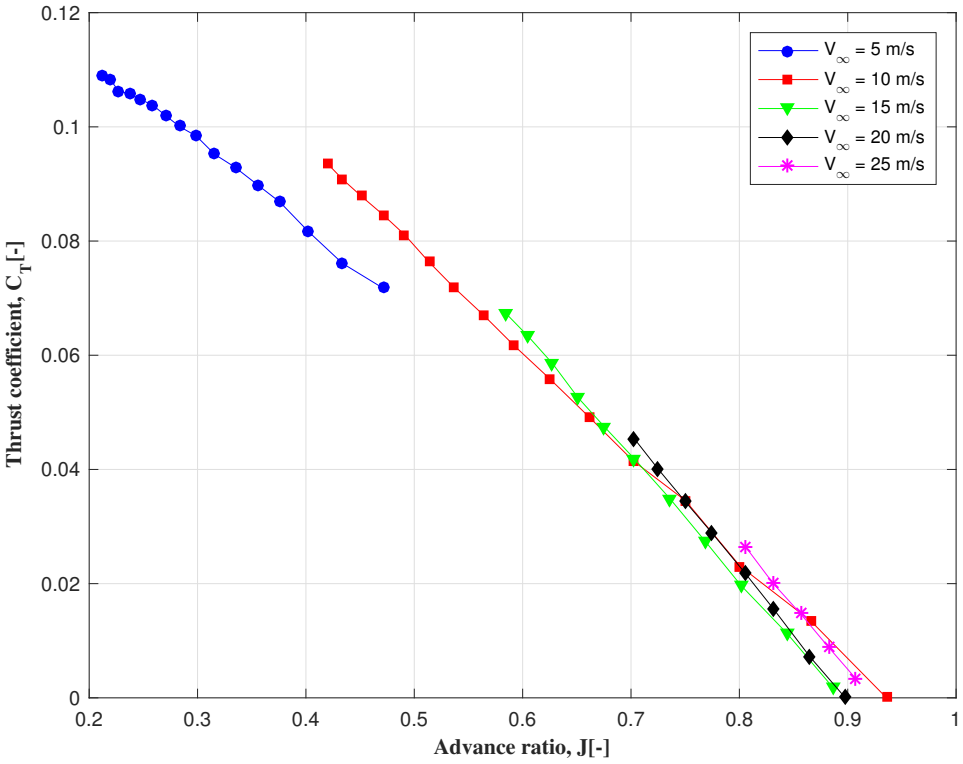

Figure 5.3: Thrust coefficient versus advance ratio for different freestream velocity values.

Table 5.2: The gradient and deviation from mean values of the C_T-J curves for different freestream velocity values.

Velocity	Slope	Deviation from mean
5 [m/s]	-0.145	+27.5 %
10 [m/s]	-0.181	+9.6 %
15 [m/s]	-0.218	-8.6 %
20 [m/s]	-0.223	-16.2 %
25 [m/s]	-0.225	-12.2 %
Avg.	-0.198	

an increase in RPS, the increase in thrust coefficient is larger. The underlying cause is the increase of Reynolds number with an increase in windtunnel velocity. It is hypothesized that at lower Reynolds numbers a laminar separation bubble exists over parts of the propeller blade, causing the lift-drag ratio of the blade to decrease [46]. Additionally, it is known that the effect of Reynolds number on the L/D-ratio is more pronounced under Re values below orders of $1 \cdot 10^5$ [47]. Another explanation for the reduced propeller performance at lower advance ratios is that the blade stalls. Due to the higher rotational velocity the angle that the blade experiences increases. At a certain point the flow separates from the blade, as is shown with the PIV measurements in figure 3.6, resulting in a reduction in lift. The results have. Seeing that both explanations are expected to occur and that the experiment has been performed between a range of advance ratios for which the thrust curve shows linear behavior, it can be concluded that the measurements are correct and that the experimental data can be used for further analysis.

5.2. Verification of Conceptual Model

In order to perform the comparison between the experiential results and the results from the conceptual model, the latter needs to be verified. If possible, the data will be verified quantitatively, else a qualitative approach is used. In this section the verification of the different components of the model are discussed.

5.2.1. Vortex Characteristics

In order to verify the circulation contained in the vortex, a different method to determine the circulation is used. This method makes use of the propeller loading and assumes that the circulation is constant along the propeller span and is shed instantaneously at the propeller tip. These assumptions are considered valid, seeing that during the experiment the measurement surface was positioned at a significant distance from the propeller, allowing the circulation that is shed along the propeller span as a result of the lift distribution to roll up and be largely contained in the vortex. By making this assumption it allows one to use equation 5.3, where T_b is the thrust produced per blade and A is defined in equation 5.4, where R_{hub} is the radial distance from the center of the propeller to the base of the blade and R_{tip} the radius of the entire blade. The thrust per blade is in turn determined with equation 5.5, where D_p is the diameter of the propeller.

$$\Gamma_0 = \frac{T_b}{A} \tag{5.3}$$

$$A = \int_{R_{hub}}^{R_{tip}} \rho \cdot \sqrt{V_0^2 + (2\pi nr)^2} \cdot cos\left(atan\left(\frac{V_0}{2\pi nr}\right)\right) \mathrm{d}r \tag{5.4}$$

$$T_b = \frac{\rho C_T}{N} \frac{V_0^2}{J^2} D_p^2 \tag{5.5}$$

The results for the different experimental cases are collected in table 5.3, together with the results obtained through the PIV data as described in Chapter 4 and their corresponding differences. It is expected that the circulation obtained with the above described method is larger than the circulation obtained with the PIV measurements. This is due to the fact that in reality, i.e. the measurement made during the experiment, the circulation shed from the propeller blade rolls up into the vortex over a certain period of time. In contrast, the blade loading method assumes an idealized version of reality, where the shed circulation is instantaneously contained in the vortex resulting in an overestimation of the vortex circulation.

The results provided in table 5.3 show significant differences between the PIV measurements and the results obtained from the blade loading method. As expected, the blade loading method overestimates the circulation in the vortex, but it does predict the right order of magnitude.

Table 5.3: Vortex circulation values determined using the PIV measurements and the blade loading method, for the three different cases examined during the experiment.

	From PIV [m^2/s]	From blade loading method [m^2/s]	Difference [%]
Case 1	0.091	0.116	27%
Case 2	0.069	0.083	20%
Case 3	0.104	0.120	15%

5.2.2. Vortex Component of Model

To verify the results of the vortex pressure component as determined with the conceptual model a qualitative method, consisting of a trend analysis, will be employed. In this particular case two aspects of the vortex component will be investigated, namely the tangential velocity distribution and the core pressure distribution of the vortex. Additionally, the expected outcome of the conceptual model will be defined in a qualitative manner. Figure 5.4 displays the tangential velocity and pressure distribution of a vortex with representative circulation computed using the conceptual model.

With respect to the tangential velocity distributions a number of expectations can be formulated; firstly, seeing that the absolute value of the tangential velocity is considered, the shape of the velocity distribution at the vortex centerline should show two positive peaks and a value of zero at the vortex center. Furthermore, the magnitude of the tangential velocity should decrease as the vortex ages due to the diffusion factor contained in the Lamb-Oseen vortex model. Finally, moving away from the vortex centerline should result in two changes to the tangential velocity distribution. Since the tangential velocity is zero only at the vortex center, the distinctive shape of two peaks and a valley should be replaced by a simple single peak. Secondly, the maximum tangential velocity should decrease in magnitude when moving away from the centerline. From

figure 5.4 it can be concluded that each of the expected trends are present in the results from the conceptual model.

As the vortex core pressure is closely linked to the tangential velocity, the expected trends of the vortex pressure closely resemble those discussed previously. The only difference is that the pressure distribution at the vortex centerline should be shaped as a single valley. The other trends, namely the reduction in magnitude with age and with distance from the centerline, hold for the pressure distribution, as is confirmed from examining figure 5.4.

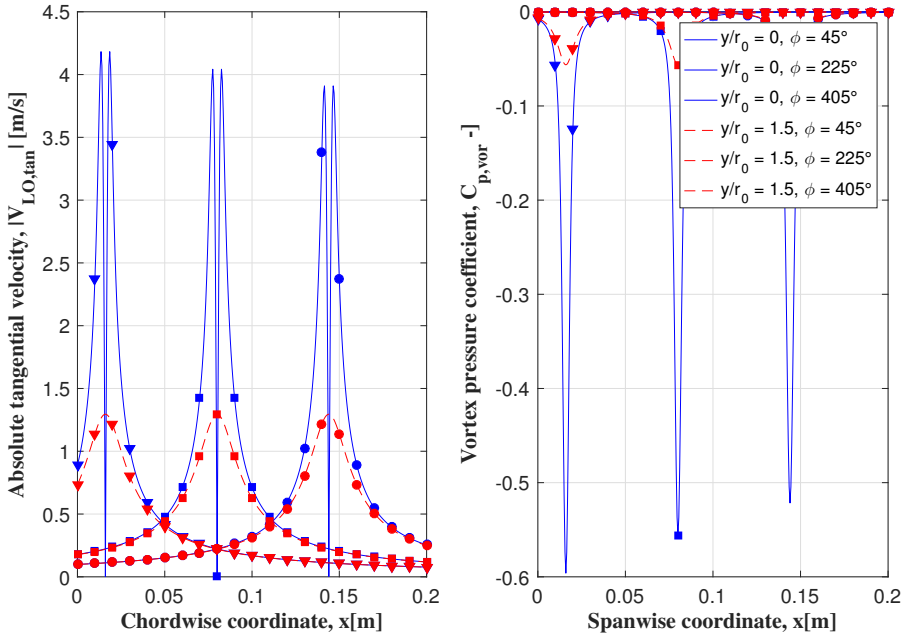

Figure 5.4: Absolute tangential velocity and pressure distributions of the vortex computed using the conceptual model at spanwise coordinates $y/r_0 = 0$ and $y/r_0 = 1.5$ and phase angles $\phi = 45°, 225°$ and $405°$.

5.2.3. Induced Angle of Attack Effect

As explained in Chapter 4, the axial velocity component at the leading edge induced by the vortex governs the magnitude of the induced pressure fluctuation. Therefore, the expected results with respect to the induced pressure fluctuations are based on the behavior of this velocity component at the leading edge. For a given spanwise location, the magnitude of the tangential velocity in the x-component decreases with increasing vortex distance to the leading edge. Therefore, given that at $\phi = 0°$ the vortex is located at the leading edge, the induced pressure is expected to decrease with passing of time as the vortex moves downstream and away from the leading edge. This behavior is confirmed when observing figure 5.5a.

On the other hand, for a given vortex age the velocity component in the axial direction at the leading edge increases when moving closer to the vortex centerline, but is equal to zero at the vortex centerline. The induced pressure is expected to increase and decrease correspondingly. These expectations are confirmed when examining figure 5.5b.

Another trend that is to be considered is the difference between the upper and lower surface. Seeing that the pitch angle of the vortex causes a downwash on the advancing side of the surface, the upper and lower surfaces are expected to react in opposite manners to one another; a downwash advancing side is expected to result in a less negative pressure distribution, while the corresponding upwash experienced by the retreating side will lead to lower pressure coefficient values over the airfoil. This opposite behavior between the upper and lower sides of the surface is clearly visible from figures 5.5a and 5.5b.

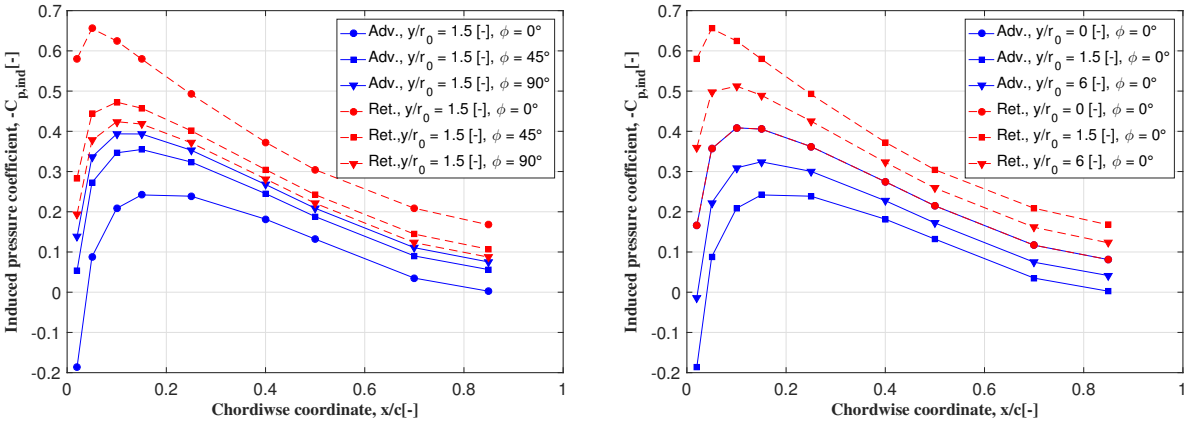

(a) Different vortex phase angles.

(b) Different spanwise coordinates.

Figure 5.5: Induced pressure coefficient distributions over advancing and retreating sides for multiple phase angles and spanwise coordinates.

5.2.4. Fluctuating Pressure

As covered in Chapter 4 the induced velocity component discussed in the previous subsection and the time dependent passing of the low pressure vortex core generate a time-dependent total pressure. In order to obtain the unsteady pressure component the baseline, i.e. constant, pressure component needs to be subtracted from the induced pressure. Seeing that the swirl component in the baseline flow is neglected, the resulting pressure distributions should be almost constant along the span of the wing. There should be a small change due to compressibility effects but at the flow velocities considered here these are negligible. Additionally, the airfoils used in the project are symmetrical. Combining this fact with the absence of swirl in the analysis, the baseline pressure distributions over the upper and lower surfaces should be the same.

Figure 5.6 shows the fluctuating pressure distributions as a result of the velocities induced by the vortex. As can be seen, the fluctuations on the upper and lower surface are equal, confirming the expected behavior. By moving away from the vortex core along the span the level of fluctuation also decreases, which is as expected. Similarly, the vortex pressure decreases as the vortex age increases from the moment it collides with the wing at the leading edge. This to is expected behavior. Furthermore, considering that the induced velocities at the vortex centerline are equal to zero the induced pressure should be equal to the baseline pressure, resulting in a net fluctuating pressure value of 0 at that location. In figure 5.6b that can be clearly observed.

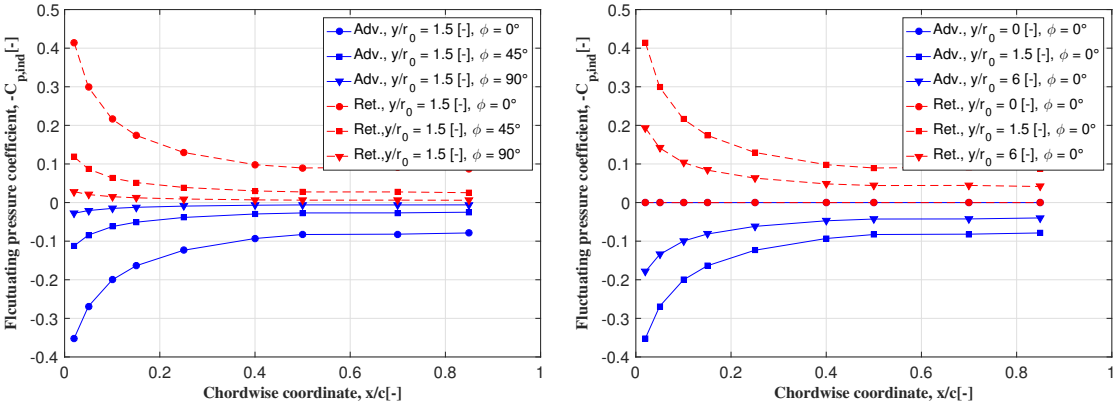

(a) Different vortex phase angles

(b) Different spanwise coordinates

Figure 5.6: Fluctuating pressure distributions, $C_{p,ind}$, over advancing and retreating sides for multiple phase angles and spanwise coordinates.

6

Results

The results from the verification performed in Chapter 5 show that the experiment was performed correctly. The results obtained during the experiment will be analyzed in section 6.1. Then, in section 6.2 a number of analyses are performed to investigate the similarities and differences of results measured during the experiment and those obtained from the conceptual model. The selected approach is to start with a high-level analysis to find the most significant differences, followed by more in-depth investigations and a quantification of these differences. The findings from the analyses will be used in Chapter 7 to answer the research questions.

6.1. Analysis of Experimental Results

The vortex-surface interaction measured during the experiment and described with the conceptual model is a complex one. To put the results in context and facilitate the discussion of the interaction, a schematic representation of the interaction, including the reference system, velocity vectors, flow regions and views, is presented in figure 6.1. Additionally, as the different experimental cases are used to analyze the results and will be mentioned regularly, the parameters corresponding to the different cases are provided again in table 6.1. First a general analysis of the results is performed in subsection 6.1.1, after which observations made in that subsection are discussed at greater length in subsections 6.1.2 to 6.1.5.

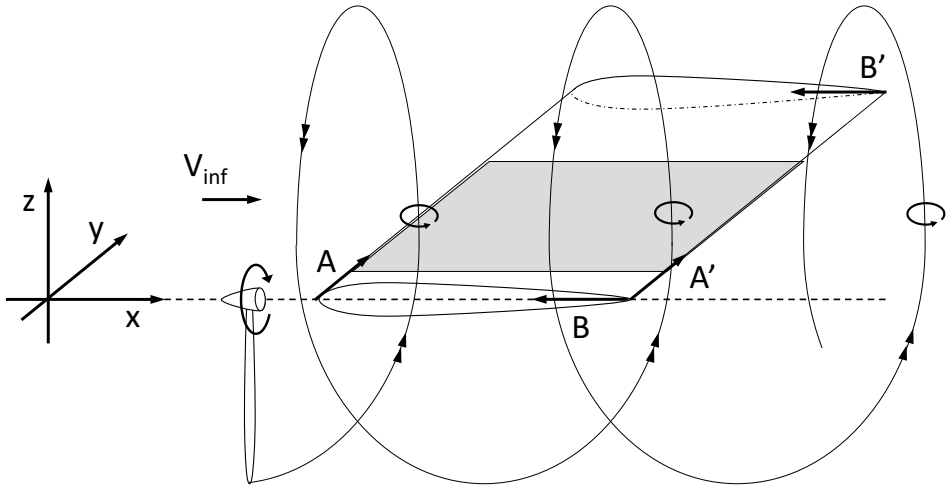

Figure 6.1: Schematic representation of the propeller tip vortex-surface interaction. The grey area represents the field of view as captured during the PIV measurements.

Table 6.1: Parameters describing the different experimental cases.

	Advance ratio [−]	Freestream velocity [m/s]
Case 1	0.60	10
Case 2	0.67	10
Case 3	0.67	15

6.1.1. General Analysis of Experimental Results

In order to obtain an overview of the pressure fluctuations over the surfaces, the RMS values of the unsteady pressure coefficient, $C'_{p,RMS}$, are plotted in the x/y-plane. This is done for both the advancing and retreating side of both the NACA0012 and NACA0016 airfoil for all measurement cases. The plots are shown in figures 6.2 and 6.3. In order to compare the results and place them in context, the data is plot logarithmically axial and spanwise axes of the contour plots have been non-dimensionalized with respect to the vortex radius measured during the experiment, r_0. The y-axis has been set to 0 at the spanwise coordinate of the vortex as determined with the PIV measurements. An additional set of axes has been added, of which the axial and spanwise axes have been non-dimensionalized with respect to the wing chord, c, and the propeller radius, R, respectively.

From the contour plots in figures 6.2 and 6.3 a number of observations can be made. On both sides, a region of high pressure fluctuations can be observed from the leading edge to the trailing edge with a width of approximately $1-2\ r_0$. The spanwise location of the region differs between the upper and lower region but is approximately at the y-coordinate where the vortex is expected to interact with the surface from the PIV measurements during the experiment. When one considers the width of the region, the spanwise location of the region and the magnitude of the pressure fluctuations with respect to the surrounding values, it is concluded that the pressure fluctuations are caused by the low pressure vortex core, which is in accordance with earlier experimental studies [26, 48]. This conclusion is confirmed by examining the waveforms plot in figures 6.5a and 6.5b. In the waveforms a clear periodic oscillation with a phase of π radians is present, which is accordance with the two vortices per propeller rotation. Another observation that can be made from figures 6.2 and 6.3, is the existence of a second region of high pressure fluctuations. This region is limited to the leading edge, namely from 0.00 to 0.04 x/c, and is only visible in the slipstream region of the flow, $0.4 < y/R <= 0.9$. The fluctuations in this region are likely caused by the interaction between the propeller wake and the surface.

Next to the similarities, it is also clear that there are significant differences between the advancing and retreating sides of the surface. One of the differences is the location where the assumed vortex path originates from. On the advancing side, the path is located at approximately $0.25\ y/r_0$, while on the retreating side the path is located at approximately $-1\ y/r_0$. At the leading edge there are more differences. On the advancing side there seems to be an absence of pressure fluctuations at the spanwise vortex interaction region and a presence of pressure fluctuations inboard of this region. The retreating side, however, does not show the absence of fluctuations observed at the vortex interaction region at the leading edge. Furthermore, it can be observed that on the retreating side the assumed vortex path seems to bend in the inboard direction, which it does not on the upper surface.

When comparing the results of the different cases, figures 6.2a through 6.2e, it is clear that the above mentioned behavior is visible for all cases. However, there are differences in the magnitude of the fluctuations, which are larger for test case 1 than for test cases 2 and 3. Case 3, on the other, hand shows larger fluctuations than case 2. Comparing the pressure fluctuations over the NACA0012 and NACA0016 wings, one can conclude that there are very few differences in both the distribution and magnitude of the pressure fluctuations.

6.1.2. Leading Edge Behavior

At the leading edge the experimental data shows striking behavior. The pressure fluctuation distribution is very different for the advancing and retreating side. On the advancing side in the slipstream region, $y/R = -1$ to -6, at the first microphone location, $x/c = 0$ to 0.02, the RMS values are significant, which is expected from the interaction between the unsteady downwash contained in the propeller slipstream and the surface. The RMS values in the vortex region, $y/r_0 = -1$ to 1 and $x/r_0 = 1$ to 18, are significant as well, which is also as expected. However, in contrary to previous studies [15, 16, 18] the $C'_{p,RMS}$ values at the leading edge in this

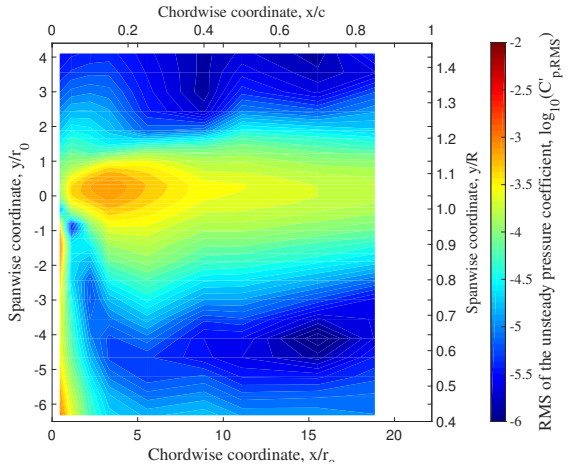

(a) Case 1, advancing side

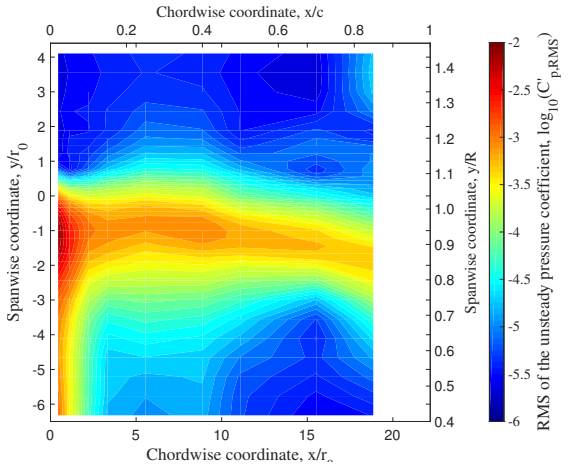

(b) Case 1, retreating side

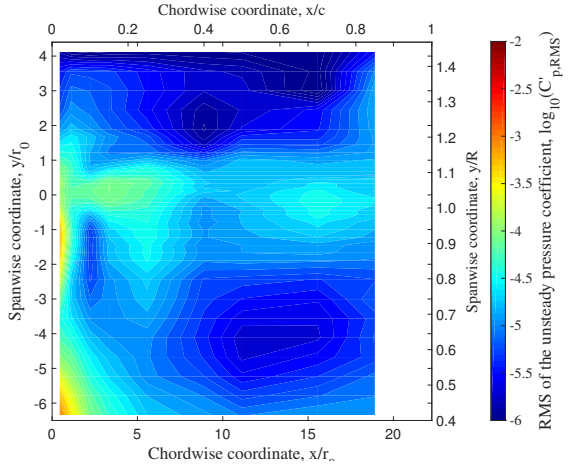

(c) Case 2, advancing side

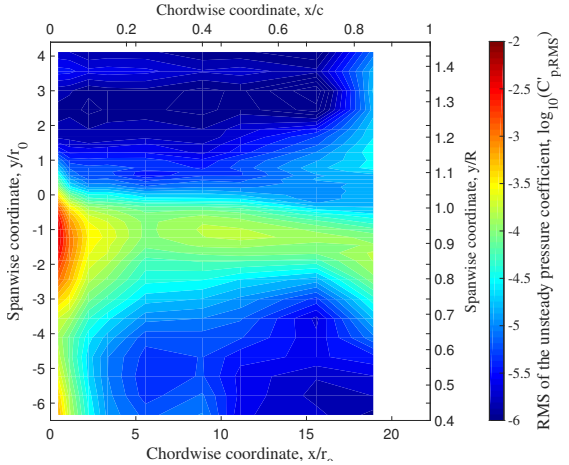

(d) Case 2, retreating side

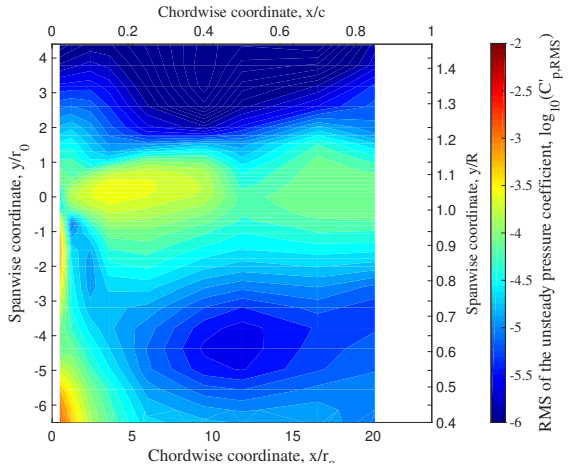

(e) Case 3, advancing side

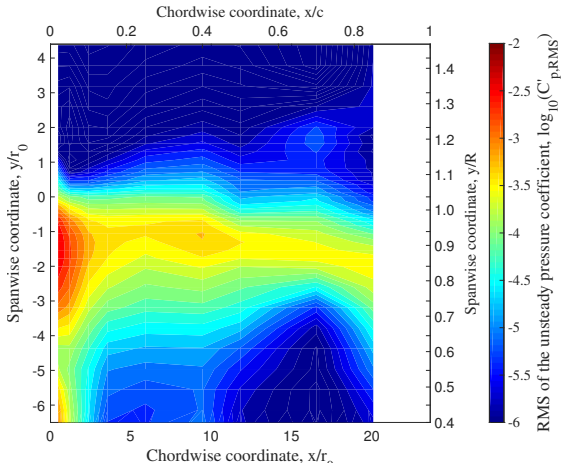

(f) Case 3, retreating side

Figure 6.2: Contour plots of the $C'_{p,RMS}$ distributions on advancing and retreating side from experiment. Logarithmic scale, airfoil NACA0012, $J = 0.6$ and $V_\infty = 10$ m/s.

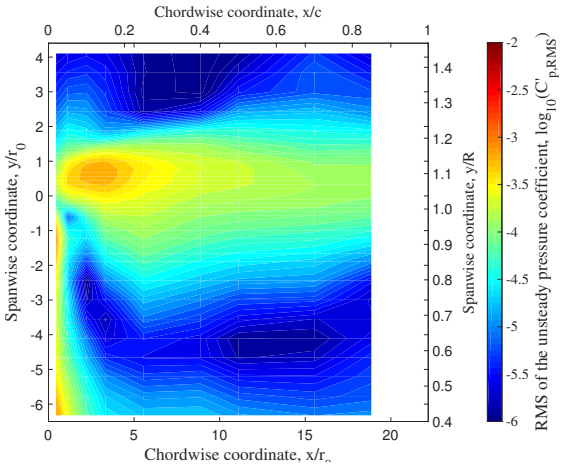

(a) Case 1, advancing side

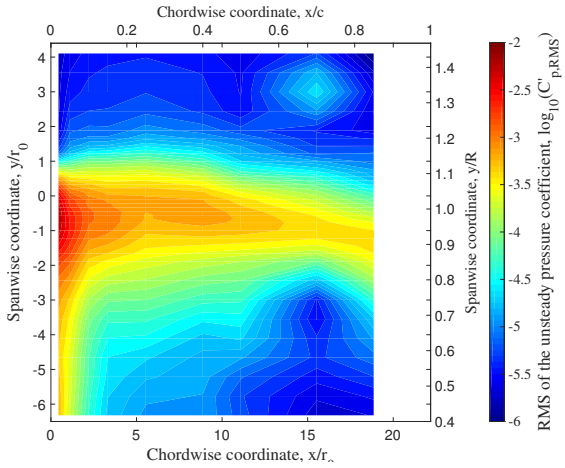

(b) Case 1, retreating side

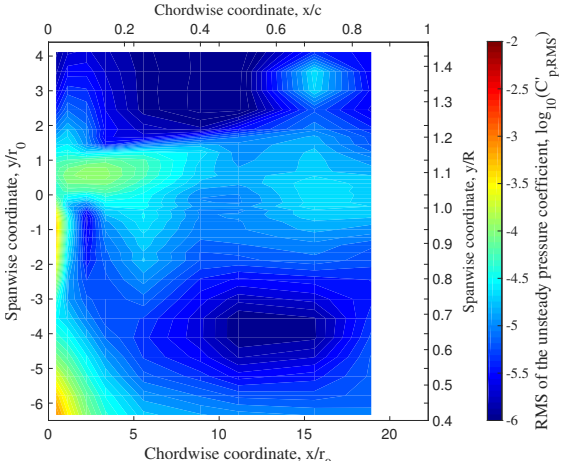

(c) Case 2, advancing side

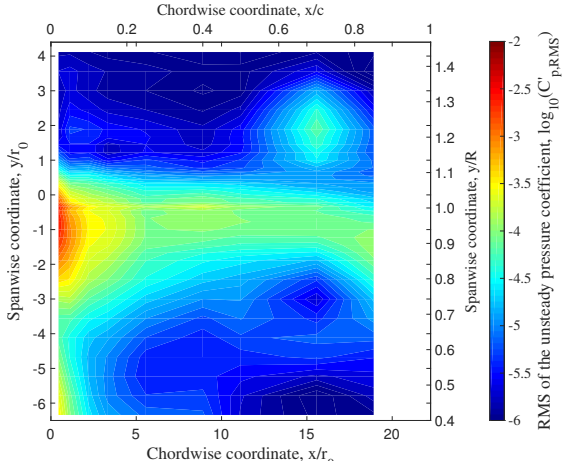

(d) Case 2, retreating side

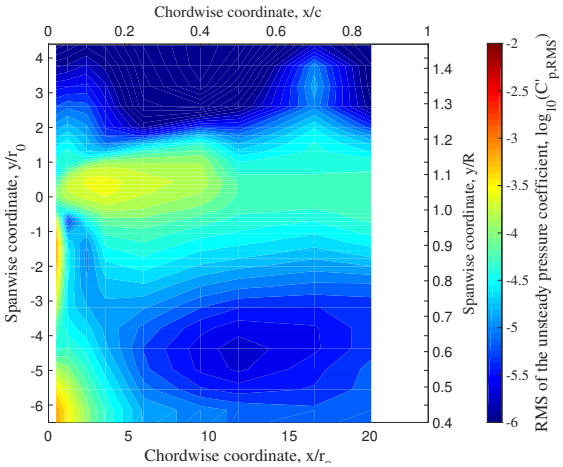

(e) Case 3, advancing side

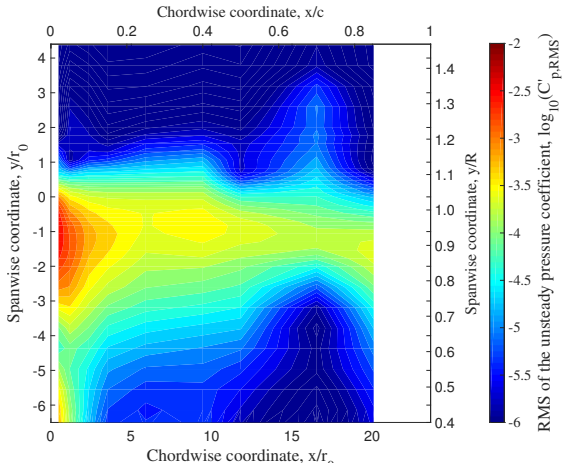

(f) Case 3, retreating side

Figure 6.3: Contour plots of the $C'_{p,RMS}$ distributions on advancing and retreating side from experiment. Logarithmic scale, airfoil NACA0016, $J = 0.6$ and $V_\infty = 10$ m/s.

region, between $y/r_0 = -1$ to 1 and from $x/r_0 = 0$ to 1, are much smaller than expected. On the other hand, the retreating side experiences only one continuous region of high $C'_{p,RMS}$. This region, which is attributed to the vortex core pressure, starts at a different spanwise position than on the advancing side, namely between from $y/R = -2.5$ to 0 versus $y/R = -1$ to 1 respectively. Importantly, this behavior is clearly present in all combinations of cases and wings, as shown in figures 6.2 and 6.3.

These observations are further supported by examining the $C'_{p,RMS}$ values registered at the three leading edge microphone locations, corresponding the chordwise coordinates $x/c = 0.02, 0.05$ and 0.1. The results are visualized as seen from the aft of the wing (fig. 6.1, view A-A'), as shown in figure 6.4. It is clear that on the advancing side in the slipstream region the largest pressure fluctuations occur at the first microphone position, then the second and then the third. At the expected vortex interaction location, however, the order of the magnitude of the $C'_{p,RMS}$ values is reversed. The retreating side does not show this behavior. However, the fact that the vortex seems to interact more inboard of the location where it would be suspected could cause an overlap between the pressure fluctuations generated by the vortex and the wake, which would hide the phenomenon described above. Here too, the results of the other combinations of test cases and airfoils provided in Appendix C show the behavior described above.

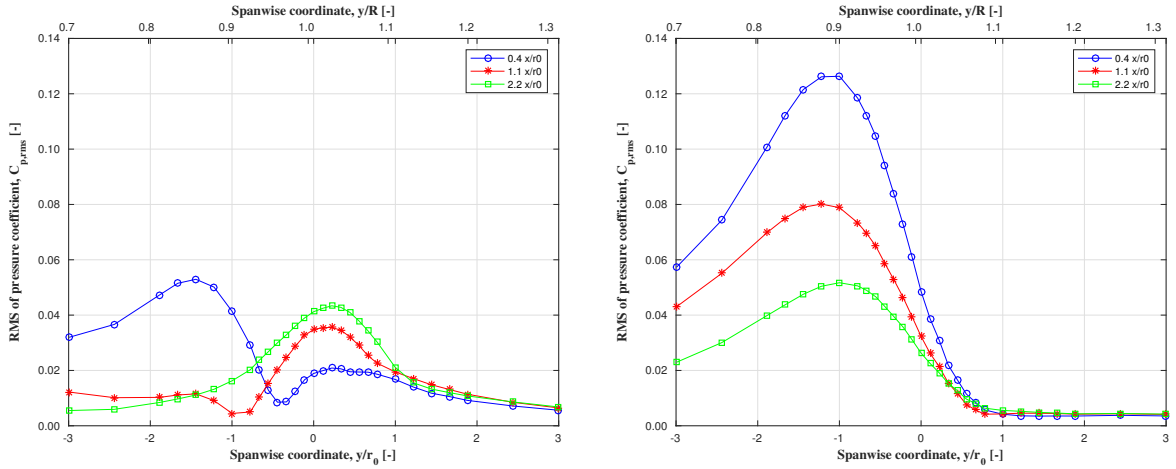

(a) Advancing side

(b) Retreating side

Figure 6.4: Spanwise distribution of the RMS of the unsteady pressure coefficient, $C'_{p,RMS}$, at the leading edge for both the advancing and retreating sides. NACA0012, $J = 0.6$ and $V_\infty = 10$ m/s.

In conclusion there are two differences between the advancing and retreating surface that are unexpected; the first is the difference in vortex interaction location. The second is the absence of pressure fluctuation RMS at the leading edge vortex region on the advancing side. The source of this behavior is either a physical phenomenon or an error made during the experiment. A number errors could have been made during the experimental campaign that would explain these differences. With respect to the difference in the spanwise coordinate of the vortex path a misalignment issue could hypothetically be the cause. Seeing that only one row of microphones on one side of the measurement surfaces was used to measure the pressure fluctuations, the wing had to be removed from the setup, flipped and returned to the setup in order to measure the pressure fluctuations on both sides of the wing. During this procedure an error could have been made. However, due to the symmetrical shape of the setup this is not a possible error source. Additionally, the behavior is present in all combinations of test cases and wings and it is unlikely that the same error would be made for each measurement.

With respect to the low values of the $C'_{p,RMS}$ at the leading edge in the vortex region of the advancing side, two possible errors could be conceived; there could have been some sort of error with the leading edge microphones (microphones #1, #2 and #3) resulting in lower observed $C'_{p,RMS}$. However, seeing that the measurements performed with both wings show the same behavior this is unlikely to be the case. Another source of error could be a too large microphone spacing which would result in the vortex not being registered. As the measurement resolution at the leading edge is 1mm in chordwise direction and 4mm in the spanwise di-

rection and the vortex diameter is 20mm, the vortex should be visible in the results. It is therefore concluded that the source of the unexpected behavior is not an error made during the experiment and that a physical phenomenon causes the unexpected behavior of the leading edge pressure fluctuations and vortex interaction location.

In order to examine the unexpected behavior, the waveforms at the leading edge, i.e. at microphones #1, #2 and #3, in the vortex region are visualized for both the advancing, figure 6.5a, and the retreating side, figure 6.5b. The assumed vortex centerline, for which the data is plotted, is different for the two sides, namely y/r0 = 0.5 for the advancing side and y/r0 = −0.75 for the retreating side. It should be noted that the waveforms have been phase synchronized with respect to the peak magnitude of microphone #1 on the retreating side in order to better compare the time-dependent pressure at each chordwise location. Note that the waveforms show negative unsteady pressure coefficient, $-C_p'$.

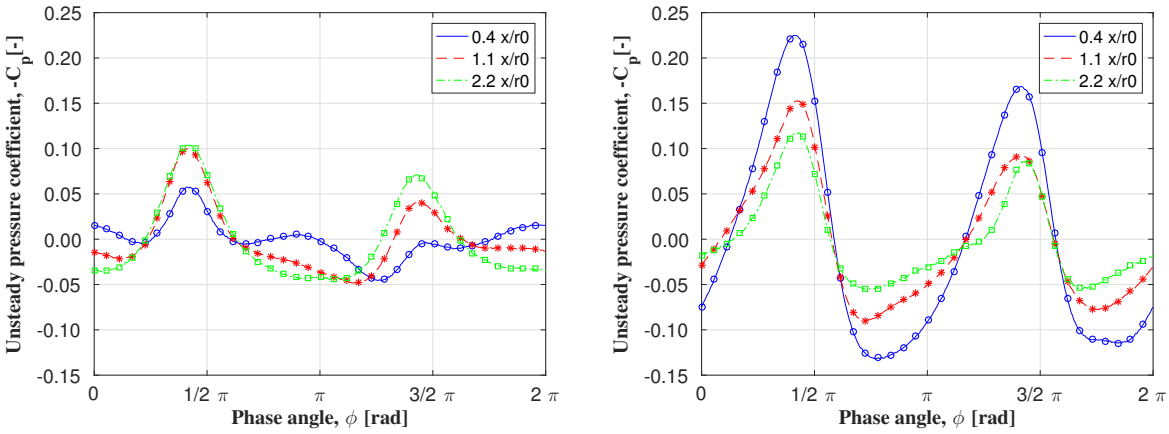

(a) Advancing side

(b) Retreating side

Figure 6.5: Phase synchronized waveforms of the unsteady pressure coefficient $-C_p'$ waveform at the vortex centerline, at the leading edge for both the advancing and retreating surface. NACA0012, $J = 0.6$ and $V_\infty = 10$ m/s.

At the first microphone position on the advancing side, the expected increase in unsteady pressure at the vortex passage, at $\phi = 1/2\pi$ and $3/2\pi$, does in fact occur. However, it is also observed that the low $C'_{p,RMS}$ value for that microphone is likely due to the presence of a net zero pressure coefficient at $\phi = \pi$ and 2π. Considering the conservation of momentum, the expectation is that the magnitude of the negative unsteady pressure coefficient peak is approximately equal, or at least of the same order, as the magnitude of the flange following the peak. This behavior is indeed present for the measurements captured with microphone #3, but becomes less true when moving towards the leading edge. It seems as though there is a phenomenon that causes a reduction in pressure at these phases, counteracting the expected increase in pressure. A difference in pressure between the first and second vortex passage can also be observed and is attributed to the defects or deformations of the propeller, resulting in different vortex strengths between the two blades.

On the retreating side, the behavior of the microphones is different. Although the decrease in pressure coefficient when moving away from the leading edge is present, as is the difference between the first and second vortex passage, the unsteady pressure values of the flanges do not significantly deviate from the expected values. It seems as though the unexpected behavior of the vortex at the leading edge is limited to the advancing side only. Additionally, the unsteady pressure peak is largest at the leading edge and becomes smaller as one moves towards the trailing edge, which is not the case for the advancing side.

From the observations made above, it is theorized that the unexpected lack of $C'_{p,RMS}$ near the leading edge on the advancing side exists due to interference between the propeller wake and propeller vortex. The low pressure in the vortex core results in a low pressure over the surface, while downwash from the blade wake results in an increase in pressure over the advancing side and a decrease in pressure on the retreating side. If these components overlap, the unsteady pressure on the advancing side should become less negative while on the retreating side becoming more negative. This corresponds to the behavior observed in figure 6.5.

If the hypothesis is true and there indeed is interference between the wake and the vortex, this should be visible when subtracting the unsteady pressure values obtained with microphone #3 from those obtained with microphones #1 and #2, as done in figure 6.6. As the unsteady pressure induced by the blade wake is concentrated at the leading edge and rapidly decreases when moving toward the trailing edge, the influence of the wake on the total waveform quickly decreases from microphone #1 to #3. The shape of these waveforms should therefore resemble those induced by the blade wake only, with the waveform of mic #1 minus #3 most similar and #2 minus #3 becoming less similar and smaller in magnitude. In the slipstream region at a significant distance from the vortex, at approximately $0.5y/R$, the induced unsteady pressure can be assumed to be a result of purely the wake and can therefore be used for comparison. The corresponding waveforms are provided in figure 6.7.

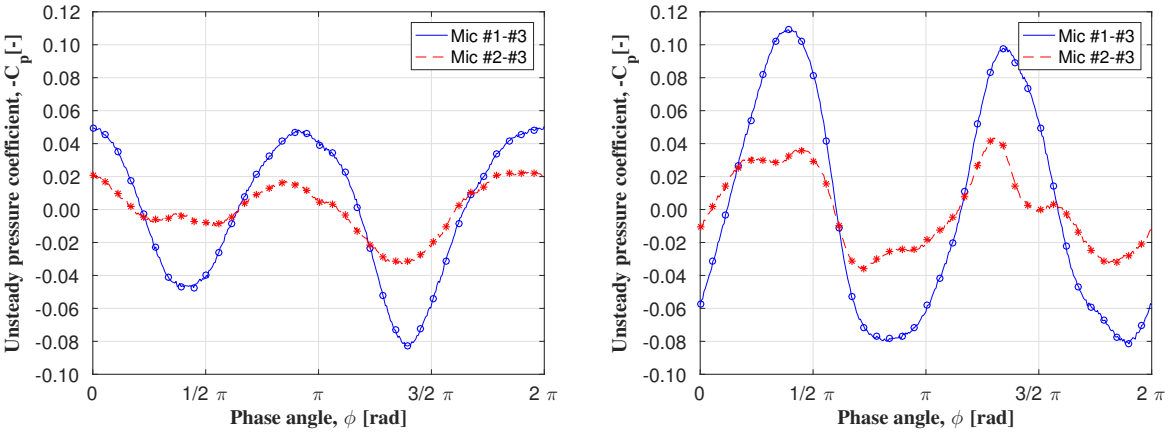

(a) Advancing side **(b)** Retreating side

Figure 6.6: Differences in unsteady pressure, $-C'_p$, between microphones #1 and #3 (blue line) and microphones #2 and #3 (red line) at the vortex centerline for both the advancing and retreating surface. The waveforms were phase corrected before subtraction. NACA0012, $J = 0.6$ and $V_\infty = 10$ m/s.

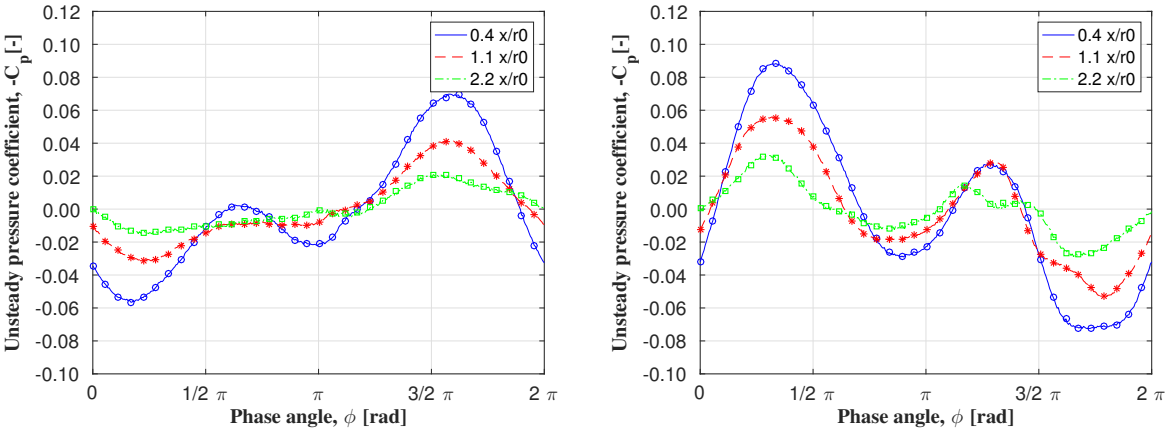

(a) Advancing side **(b)** Retreating side

Figure 6.7: Phase synchronized waveforms of the unsteady pressure coefficient, $-C'_p$, waveform in the slipstream region ($y = 0.47y/R$), at the leading edge for both the advancing and retreating surface. NACA0012, $J = 0.6$ and $V_\infty = 10$ m/s.

When comparing figures 6.6 and 6.7 it can be observed that the overall shape, magnitude and timing of the waveforms are similar. Furthermore, a strong reduction in magnitude of the waveforms can be observed moving from the leading to the trailing edge. Although significant differences exist between the waveforms and no definitive proof can be provided at the time, it is suspected that there indeed exists interference between the propeller vortex and the slipstream wake, resulting in the previously unexpected leading edge behavior at the

vortex centerline. It should be noted that other studies do not show the behavior described here. The region of vortex induced pressure fluctuations starts immediately at the leading edge. The difference between these studies [15, 26] that may have caused the different results are the distance of the measurement surface with respect to the propeller, the windtunnel and the propeller itself.

6.1.3. Vortex Path

As mentioned before, the path of the vortex on the retreating side of the surface bends inboard toward the trailing edge, as can be seen from figures 6.2 and 6.3. On the advancing side, this shearing motion is not visible. The paths of the vortex for all combinations of airfoils and cases are plot for the advancing and retreating side in figures 6.8a and 6.8b respectively. This has been done by locating the spanwise coordinate of the maximum $C'_{p,RMS}$ for each chordwise microphone coordinate. It should be noted that the first microphone has been omitted due to the fact that the $C'_{p,RMS,max}$ values for this chordwise location was often dictated by the interaction between the wake and the surface instead of the microphone. A version with the first microphone included is provided in Appendix C.3.

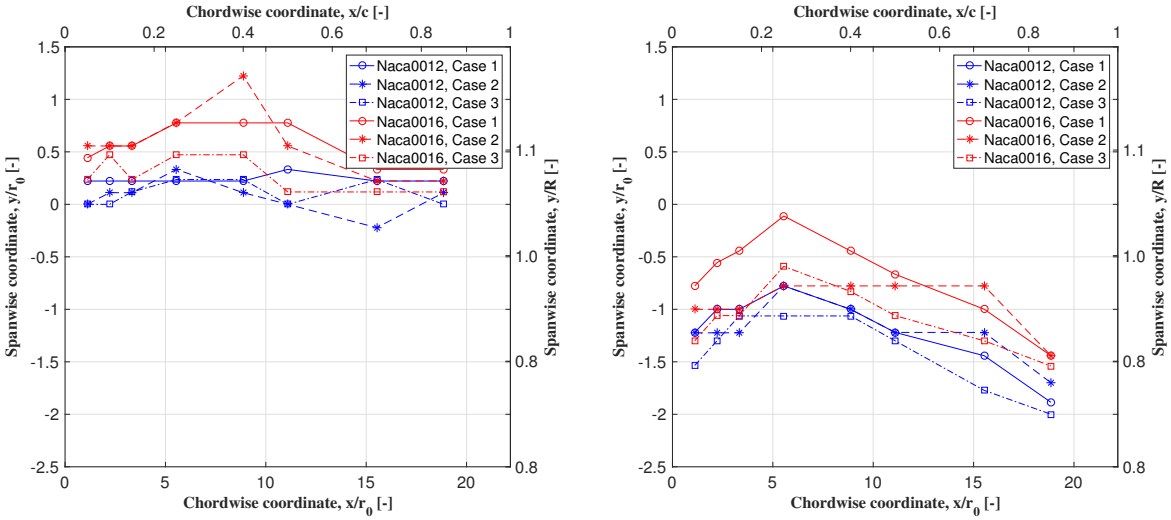

(a) Advancing side

(b) Retreating side

Figure 6.8: Spanwise $C'_{p,RMS,max}$ location at each chordwise microphone position for all combinations of cases, wings and surfaces.

As discussed in Chapter 2, the separate vortex filaments on the advancing and retreating side created as a result of a vortex-surface collision, start to move outboard and inboard respectively due to the velocities caused by the circulation shed from the surface due to spanwise lift variations. As is visible, this behavior, called 'vortex shearing', is present on the retreating side and absent on the advancing side for all combinations of cases, wing geometries and sides. Research has previously shown that the vortex shearing affects the retreating side to a larger extent than it does the advancing side [15, 16, 18]. This could be caused by the velocity component of the flow in axial direction of the vortex reference frame, but a definitive explanation for the difference in shearing cannot be given. Nonetheless, the results obtained from the experiment do concur with other experimental investigations.

It is immediately clear from figure 6.8 that the spanwise coordinate of the vortex path is significantly more outboard on the advancing side of the surface than on the retreating side. This corresponds to the observations made from figures 6.2 and 6.3. The difference may partially be contributed to the mass conservation effect, which causes the flow on the advancing and retreating side to move outward and inward respectively. However, the large measure and small distance in which this occurs, namely approximately 1.25 vortex radii of spanwise movement in 1 vortex radius of chordwise movement is too much to solely be a result of the mass conservation effect. Another cause could be a misalignment between the circular wing mount and the propeller setup resulting in a vortex incidence angle, γ (consult figure 2.6). These phenomena do not explain the difference in spanwise location of the vortex path between the NACA0012 and NACA0016, which is also visi-

ble from figure 6.8. The paths of the NACA0012 airfoil are more inboard than those of the NACA0016 airfoil. The difference in location may be attributed to the difference in leading edge radius but a concrete explanation can currently not be provided.

A difference between case 1 (J = 0.6) and cases 2 and 3 (J = 0.67) would have been expected seeing that a higher loading would cause a larger shedding of circulation and therefore a larger shearing action. However, this behavior is not distinguishable from figure 6.8. The likely cause for this is the small difference in advance ratio between the two cases and the fact that there is only a small number of data points from which to perform the analysis.

6.1.4. Effect of Cases and Wing Geometry

From the $C'_{p,RMS}$ contour plots provided in figures 6.2 and 6.3 it can be observed that for the different cases there are differences in magnitude, not in distribution, of the pressure fluctuations over the surface. The values are largest for case 1 on both the NACA0012 and NACA0016 wing, which is expected considering the advance ratio is lower than that of cases 2 and 3. This results in a higher blade loading, which in turn results in a stronger vortex and therefore larger pressure fluctuations over the surface. Additionally, the pressure fluctuations observed at the leading edge in the slipstream region are larger due to the increase in wake strength.

There is also a difference, however, between the $C'_{p,RMS}$ magnitudes measured in cases 2 and 3, as the latter shows significantly larger values over all combinations of surfaces and wings. A number of explanations could be possible. Firstly, the RMS values of the pressure fluctuations over a certain period of time become larger if the number of vortices and wakes that pass in that time frame increase. As the RMS values are taken over a propeller phase of 2π the same number of vortices contribute to the RMS values, so this is not the cause. A more likely explanation is that the vortices are stronger as they have had less time to diffuse due to the higher freestream velocity. On the other hand, the effect could be reduced by the reduced time in which the circulation shed from the propeller can roll up in the vortex. It is hard to quantify the relative contribution of these factors.

When comparing the logarithmically plotted $C'_{p,RMS}$ values, as shown in figures 6.2 and 6.3, no significant differences between the results from the NACA0012 and NACA0016 measurements can be observed. Logarithmically plot data allows one to observe the distribution of pressure fluctuations of different orders within one plot. Although this makes allows for more information to be visualized in one figure, it does give a distorted view of the actual data set. In order to investigate the differences in pressure fluctuations between the two wings, the same contour plots have been created but they have been plot linearly. The results are presented in Appendix C. In short, the conclusion drawn from the logarithmic plots is confirmed and there seems to be very limited difference between the pressure fluctuations over the two wings.

Finally, another observation can be made from figures 6.2 and 6.3, namely that there is a difference in magnitude of the pressure fluctuations between the advancing and retreating side of the surface. This has been previously shown and is therefore as expected [15, 16, 18]. One of the possible causes for the difference is the axial velocity in the vortex core. The flow in axial direction of the vortex reference frame is orientated (almost) perpendicular to the surface. As explained in section 2.3, this flow component must stagnate on the advancing side, leading to a pressure increase, while on the retreating side the opposite happens. Seeing the lack of three dimensional flow data, this hypothesis cannot be confirmed.

6.1.5. Vortex Incidence Angle

The final parameter that will be covered is the incidence angle of the vortex with respect to the surface. As discussed in section 2.3, the incidence angle determines the type of interaction, namely impingement versus collision, and the measure of downwash caused by the vortex. During the experiment the effect of the incidence angle was measured for both NACA0012 and NACA0016, but only one test case, namely test case #1. To visualize the effect of incidence angle on the magnitude and distribution of the pressure fluctuations, the spanwise $C'_{p,RMS}$ values (view A-A', fig. 6.1) are plot for the different angles. The fluctuations measured with microphone #3 were selected so that the unexpected vortex behavior discussed in subsection 6.1.2 is not contained in the plots. Also, note that for all plots the incidence angle of 50 degrees is missing. This angle could not be measured due to mechanical interference between the circular wing mount and ground structure. Additionally, for NACA0012, advancing side, γ = 70 and NACA0016, advancing side, γ = 90 the measurements

were not made.

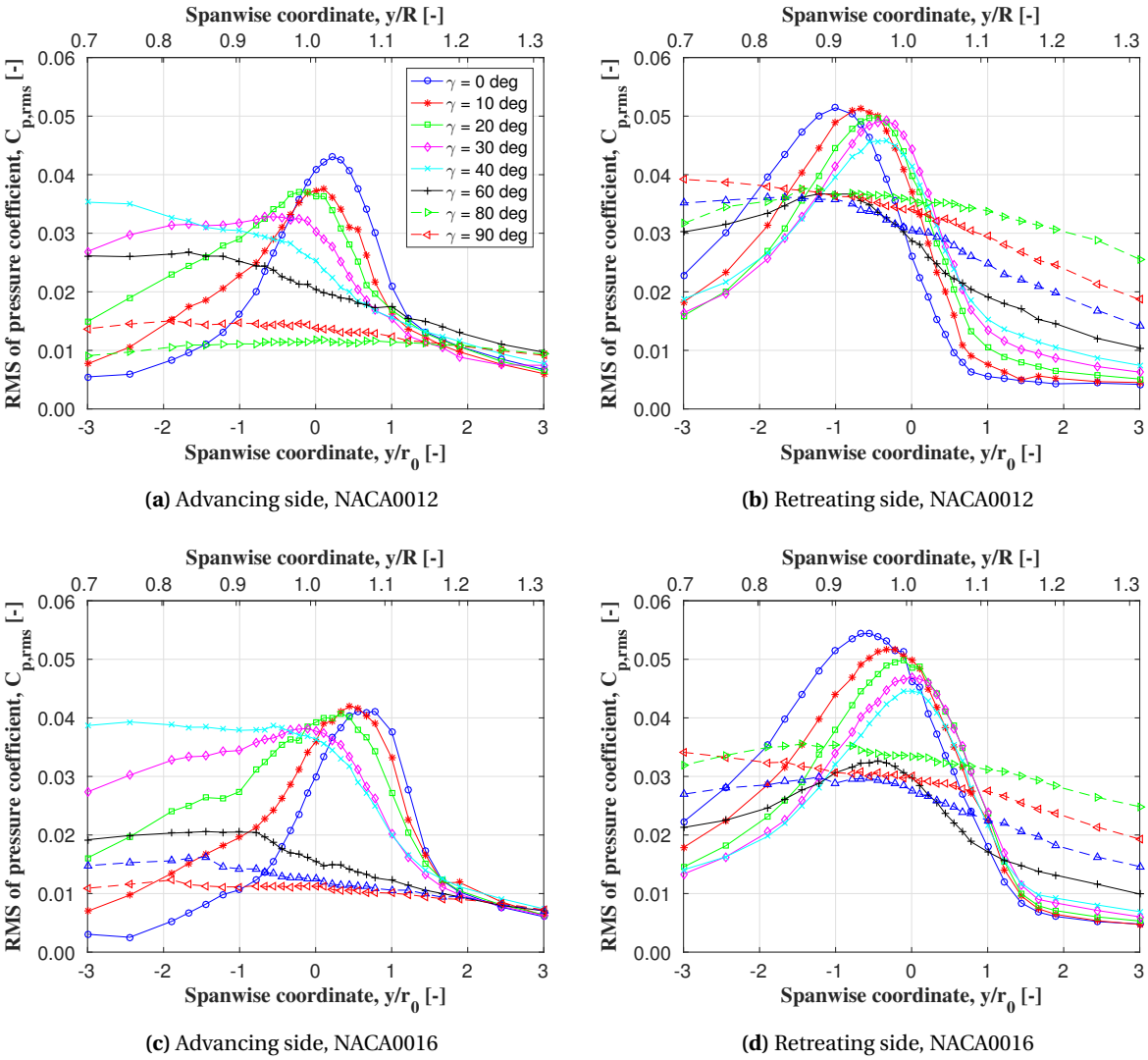

(a) Advancing side, NACA0012

(b) Retreating side, NACA0012

(c) Advancing side, NACA0016

(d) Retreating side, NACA0016

Figure 6.9: Effect of incidence angle on $C'_{p,RMS}$ values at microphone position #3, which corresponds to 0.1 x/c. $J = 0.6$ and $V_\infty = 10$ m/s.

First a comparison is made between the advancing and retreating side of the NACA0012 airfoil, i.e. between figures 6.9a and 6.9b. We can observe that on both sides that in the vortex region (-1 to 1y/r_0) the magnitude of the RMS values decreases with increasing incidence angle. These trends occur at a relatively steady rate up to $\gamma = 40$. After that point a rapid increase in interaction width and a decrease in RMS magnitude occurs for both sides. On the advancing side the increase in pressure peak width also occurs at incidence angles smaller than 40 degrees. A further difference between the two sides is that the peak moves inboard on the advancing side and outboard on the retreating side, at least up to an incidence angle of 40 degrees, after which the peak that is generated by the vortex disappears.

Using the schematical representation of the interaction at different incidence angles presented in figure 6.10 the observations made above can be explained. The widening of the pressure peak on the advancing side is believed to be caused by an increase in the area of the surface with which the vortex interacts due to the orientation of the vortex relative to the surface. This is less so for the retreating side, which corresponds to the observations made from figure 6.9. On the advancing side the corresponding steady decrease of the magnitude of the interaction is due to the increased downwash induced by the vortex resulting in smaller fluctuations. However, for the retreating side an increase in RMS values would be expected considering the

direction of the as the induced velocities. No clear explanation can be found for the slight decrease in RMS values between $\gamma = 0$ and 40 degrees on the retreating side.

With respect to the rapid decrease in RMS at incidence angles larger than 40 degrees it is theorized that a change of the interaction type occurs, namely from a collision to an impingement. Given that the vortex radius, 0.01 m, is of the same order as the surface nos radius, 0.02 m, a parallel collision is unlikely to take place. At a certain point the vortex will not collide with the surface but pass the surface on the retreating side, leaving the core intact and reducing the interaction strength. Although the data points to this explanation no definitive proof can be provided.

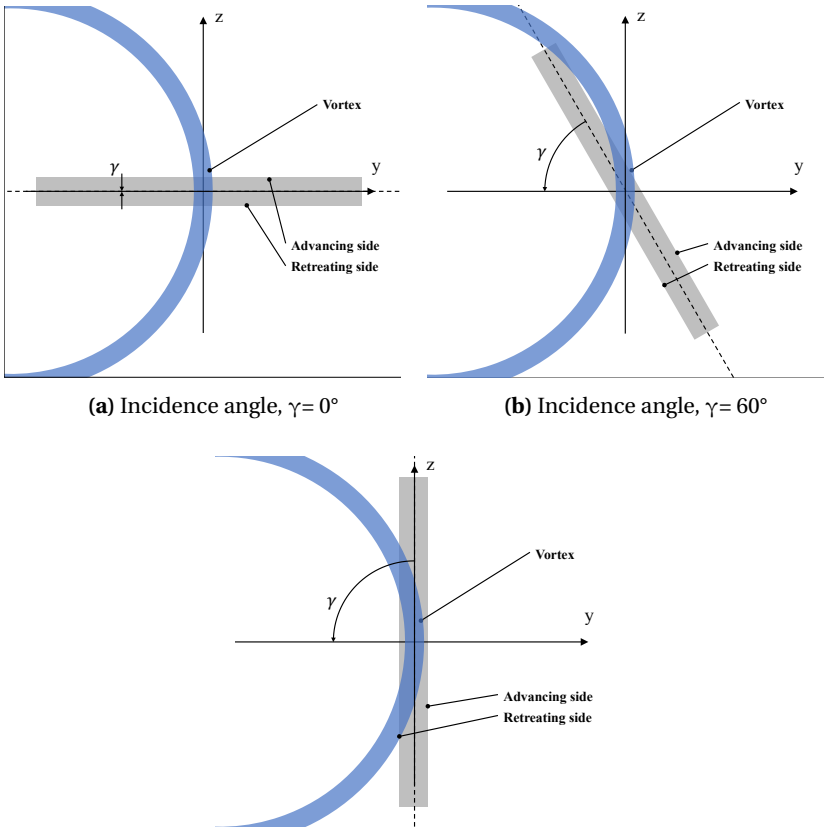

(a) Incidence angle, γ= 0°

(b) Incidence angle, γ= 60°

(c) Incidence angle, γ= 90°

Figure 6.10: Schematic representation of the vortex-surface interaction for different incidence angles.

When comparing the results of the NACA0012 and NACA0016 airfoils it can be concluded that no large differences are present. For the advancing side it seems that the pressure peaks of the NACA0012 are slightly sharper, which is expected considering the smaller nose radius. Similarly, on the retreating side there are no large differences between the two airfoils. The only observation that can be made is that the rate at which the magnitude of the RMS values decreases is slightly larger for the NACA0016.

6.2. Validation of Conceptual Model

Although not all behavior observed in the experimental results can be definitively clarified, the data will be used to assess the conceptual model. First, a general assessment of the model is performed in order to identify the discrepancies between the model and the experimental results. These discrepancies will then be discussed followed by an investigation into the effect of the airfoil geometry and test cases on the pressure fluctuations.

6.2.1. General Assessment of Conceptual Model

As was done for the analysis of the experimental results in section 6.1, the initial assessment is done by obtaining the RMS values of the phase averaged pressure coefficient, $C'_{p,RMS}$, for each data point, the results of which are provided in figure 6.11. The axis limits of the contour are equal to that of the results from the conceptual model in order to facilitate a proper comparison between the two. In contrast to the previous section, the data is plot linearly in order to prevent a distorted analysis of the differences. The NACA0012 airfoil is analyzed at $J = 0.6$ and $V_\infty = 10$ m/s, which corresponds to test case 1 during the experiment.

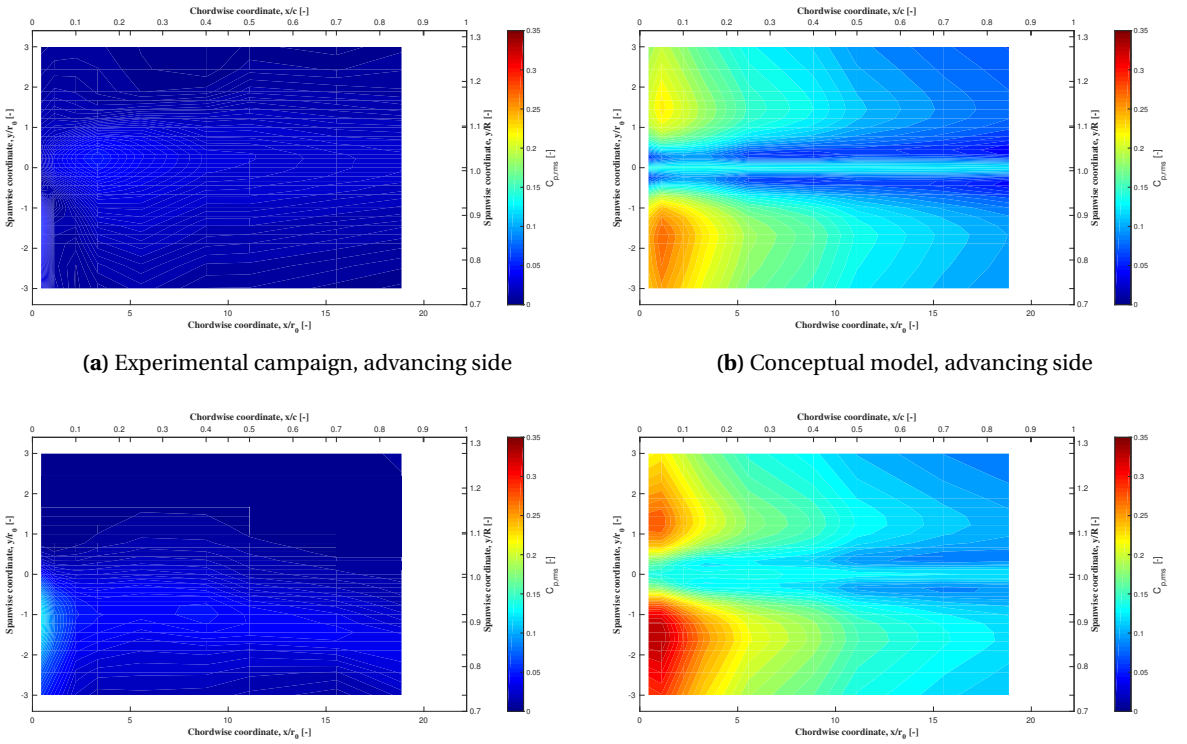

(a) Experimental campaign, advancing side

(b) Conceptual model, advancing side

(c) Experimental campaign, retreating side

(d) Conceptual model, retreating side

Figure 6.11: Retreating side $C'_{p,RMS}$ distribution obtained from the conceptual model and the experimental results. NACA0012, $J = 0.6$, $V_\infty = 10$ m/s.

From figure 6.11 it is immediately clear that the results of the conceptual model and the experimental results are remarkably different. The difference in magnitude of the $C'_{p,RMS}$ values is striking. The differences are in fact so large, that the RMS distributions of the experimental results are hardly visible in the figures. In order to visualize the distribution of the RMS values the same results are presented with different z-axis values in figures 6.12. It should be noted that a conclusion on the accuracy of the model should not be drawn from the $C'_{p,RMS}$ values alone. To quantify the accuracy, the waveforms of the pressure fluctuations should be observed, as will be done in subsection 6.2.2.

From figure 6.12 it can be concluded that the relative contributions of the vortex pressure and the induced angle of attack effect to the total pressure fluctuation differ drastically. The experimental results show that the vortex is the main contributor of pressure fluctuations, while in the model the induced angle of attack effect has the largest impact on the pressure fluctuations. This is most strongly visible in the freestream region, between 0.5 to 0.9 y/R. When considering the spanwise $C'_{p,RMS}$ distributions (view A-A' in figure 6.1) of the experimental results and the conceptual model data as provided in figure 6.13, it can be observed that the experimental results approach zero immediately outside the vortex interaction region. This is not the case in the results of the conceptual model. On the basis of the experimental results it can be concluded that the contribution of the induced angle of attack effect to the unsteady pressure resulting resulting from the vortex-surface interaction is negligible with respect to the contribution of the low pressure vortex core. It should therefore be excluded from the conceptual model.

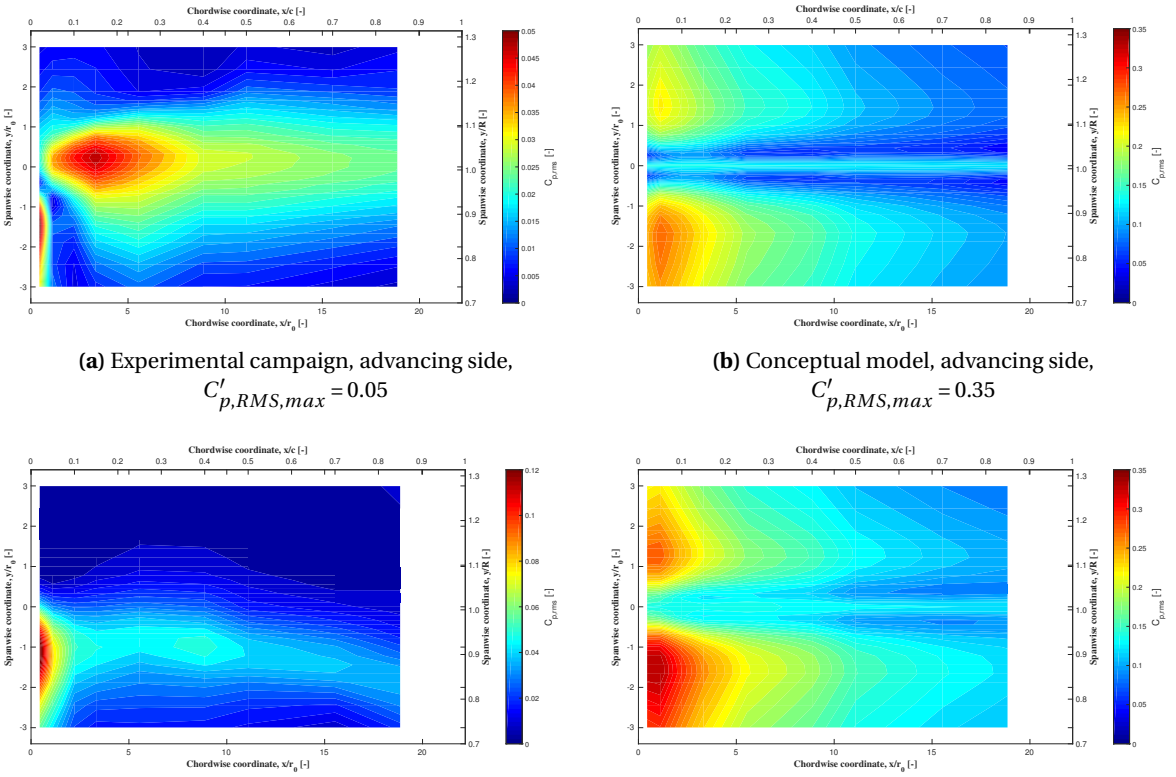

(a) Experimental campaign, advancing side, $C'_{p,RMS,max} = 0.05$

(b) Conceptual model, advancing side, $C'_{p,RMS,max} = 0.35$

(c) Experimental campaign, retreating side, $C'_{p,RMS,max} = 0.12$

(d) Conceptual model, retreating side, $C'_{p,RMS,max} = 0.35$

Figure 6.12: Retreating side $C'_{p,RMS}$ distribution obtained from the experimental results and the conceptual model. NACA0012, $J = 0.6$, $V_\infty = 10$ m/s.

Further discrepancies between the experimental data and results from the conceptual model can be distinguished when considering the vortex region in figures 6.12a through 6.12d. The vortex core size of the conceptual model is much smaller than that of experimental results, which in turn results in a higher vortex pressure coefficient. Furthermore, a clear decrease in pressure fluctuation strength can be observed on the vortex path toward the trailing edge of the surface in the experimental results, while in the model there is a limited reduction, indicating different rates of vortex decay. These discrepancies between the model and experimental data will be discussed in more detail later in the next subsection.

As a result of the simplifications made to model the interaction, additional differences between the experimental results and model data are expected. As determined in section 6.1, vortex shearing is observed on the retreating side of the surface during the experiment. This is absent in the conceptual model results as it was not contained in the model. Similarly, in the slipstream region the effect of the wake as observed in the experimental results is not visible in the results obtained with the conceptual model. The differences created by the omission of these phenomena from the model are significant and will be taken into account when the model is evaluated. However, they will not be further discussed as they are not contained in the model.

6.2.2. Vortex Core Size and Strength

In the conceptual model, the vortex core diameter, defined as the distance between the peak tangential velocity components, is determined by the use of the Lamb-Oseen vortex model. The size is dependent on the kinematic viscosity ν and the vortex age t, as defined in equation 2.5, while the size of the vortex core during the experiment has been obtained from PIV measurements. The values found for both values are presented in table 6.2. Note that the vortex core sizes were determined at the leading edge. The corresponding vortex age is used to calculate the Lamb-Oseen vortex radius.

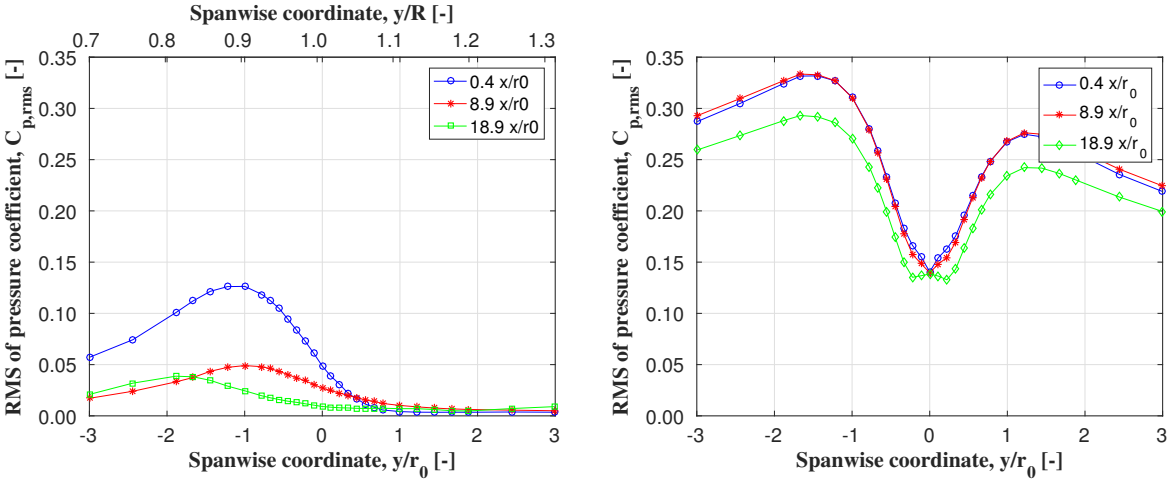

(a) Results from experimental campaign

(b) Results from conceptual model

Figure 6.13: Comparison between the experimental and model spanwise $C'_{p,rms}$ over the chord, considered for the retreating side. NACA0012, $J = 0.6$ and $V_\infty = 10$ m/s.

Table 6.2: Vortex circulation values determined using the PIV measurements and the Lamb-Oseen model, for the three different cases examined during the experiment.

	From PIV [mm]	From Lamb-Oseen [mm]	Difference
Case 1	9.0	2.2	76%
Case 2	9.0	2.2	76%
Case 3	8.5	1.8	79%

From the results we can conclude that the Lamb-Oseen vortex core size is 4 to 5 times smaller than the vortex core size measured during the experiment. The larger core size of cases 1 and 2 with respect to case 3 is likely a result of the vortex age seeing that the vortex travels downstream faster and is therefore less diffused when it encounters the surface leading edge.

The effect of the difference in core size is twofold; firstly, the magnitude of the vortex pressure fluctuations in the vortex region simulated by the model is significantly larger than the fluctuations measured during the experimental campaign, as was observed in figure 6.11. Secondly, the effect is more localized, as is visible from both figures 6.12 and 6.14. Note that microphone #1, #6 and #9, which correspond to 0.02, 0.35 and 0.90 x/c respectively, are presented.

An explanation for the difference in vortex core size could be an asymmetry or other defect present in the propeller. The PIV measurements discussed in section 3.3 and the thrust measurements covered in subsection 5.1.3 showed that the propeller behaved consistently only for a small span of advance ratios. Although the experiment was performed within the advance ratio bounds obtained from these analyses, the assumed defect in the propeller could have resulted in a vortex that was more diffused or unstable at its origin than expected, leading to a quicker decay and increase in vortex radius.

More likely, however, is that the Lamb-Oseen vortex model does not correctly predict vortices created by a propeller. It is designed to model idealized vortices, not real vortices. There are clear discrepancies at the vortex origin: the Lamb-Oseen model generates a vortex of infinitely small radius at vortex age $t = 0$, while in reality the vortex core has a finite radius at this age. Additionally, the circulation shed from the propeller requires time to roll up and form a coherent vortex. This is not the case for a Lamb-Oseen vortex, where all circulation is contained in the vortex from $t = 0$. It is expected that the combination of the finite core at the vortex creation and the roll-up of circulation over time results in a larger vortex core size than modeled with the Lamb-Oseen model.

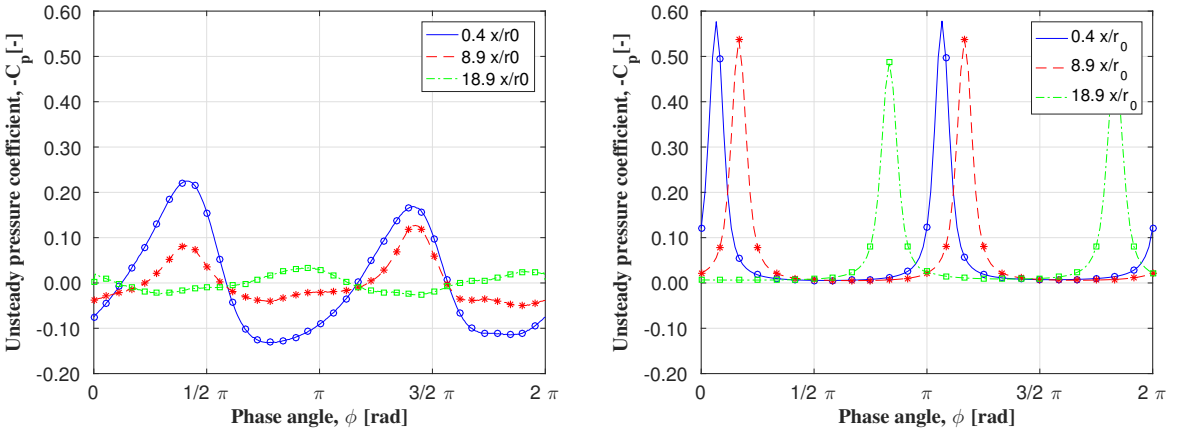

(a) Results from experimental campaign

(b) Results from conceptual model

Figure 6.14: Retreating side C_p' waveform obtained from the conceptual model and the experimental results. NACA0012, $J = 0.6$, $V_\infty = 10$ m/s.

In order to examine the effect of the inaccurate modeling of the vortex core radius on the pressure fluctuations resulting from the conceptual model and to see if improvements can be made, the Lamb-Oseen model was replaced with a vortex of constant radius, equal to the value obtained from the PIV measurements. The resulting contour plots are presented in figure 6.15 and the waveforms corresponding to the same analyses are provided in figure 6.16.

From figure 6.16 it can be observed that the unsteady pressure induced by the vortex as obtained from the conceptual model has become much less negative with the adjusted, i.e. larger, vortex core radius. This is in accordance with the expected behavior. However, it has become also significantly less negative than the pressure induced by the vortex as measured during the experiment. This is unexpected as the strength of the vortex measured during the experimental results is are taken as input for the model and therefore should be approximately equal.

The cause of this discrepancy is the method used to determine the vortex radius in the vortex from the PIV measurements made during the experiment. The technique was based on the assumption that the smoke particles measured with the PIV had the same characteristics as the other particles in the flow. Seeing that they have a different mass and size this is not true as it results in incorrect values at points where there exist large velocity gradients in the flow, such as in and around vortices. The discrepancy between the vortex radius determined using this method and the actual vortex radius proves to be much larger than expected. The vortex core pressure as obtained with the conceptual model on the vortex radius determined from the PIV measurements. Therefore the vortex core pressure fluctuations are also inaccurate. In conclusion, both the way the vortex radius is obtained from the experimental campaign as the approach employed to model the low pressure vortex core, namely the Lamb-Oseen vortex model, should be improved in order to increase the accuracy of the conceptual model.

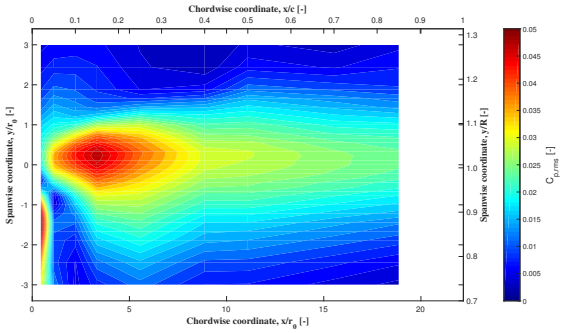

(a) Experimental campaign, advancing side, $C'_{p,RMS,max} = 0.05[-]$

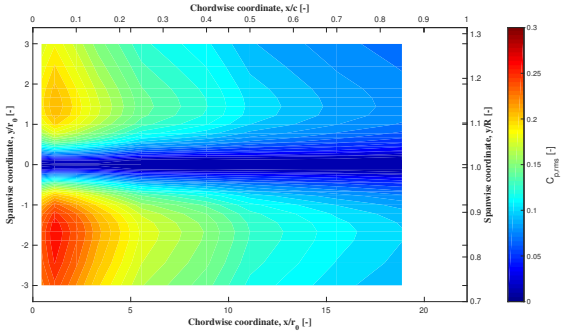

(b) Conceptual model, advancing side, $C'_{p,RMS,max} = 0.35[-]$

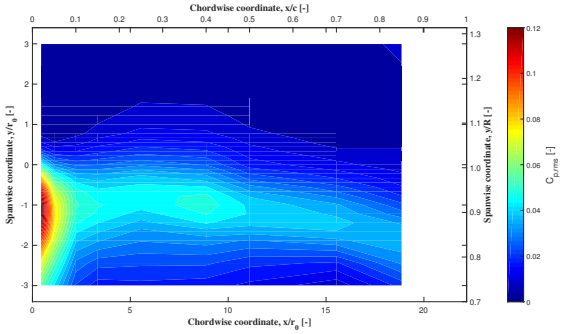

(c) Experimental campaign, retreating side, $C'_{p,RMS,max} = 0.12[-]$

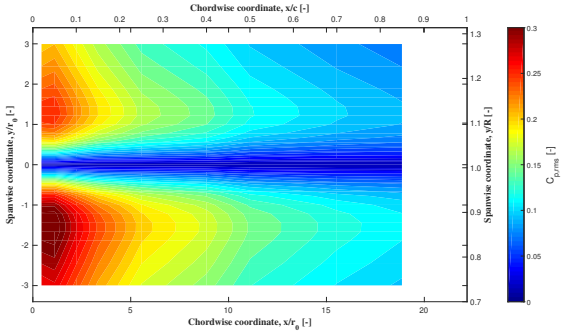

(d) Conceptual model, retreating side, $C'_{p,RMS,max} = 0.35[-]$

Figure 6.15: Contour plots of the RMS value of the unsteady pressure coefficient from the model and the experiments. The vortex radius has been adjusted from the value determined with the Lamb-Oseen model to the radius measured with the PIV measurements. NACA0012, $J = 0.6$, $V_\infty = 10$ m/s.

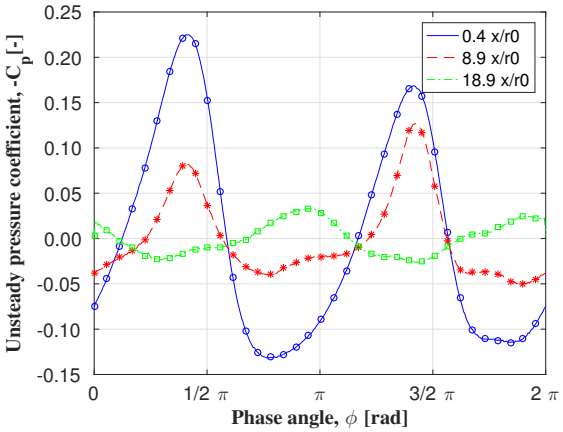

(a) Results from experimental campaign

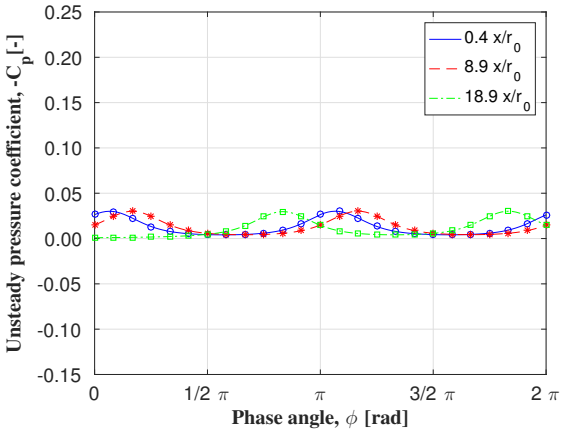

(b) Results from conceptual model

Figure 6.16: C'_p waveform obtained from the conceptual model on the retreating side. The vortex radius has been adjusted from the value determined with the Lamb-Oseen model to the radius measured with the the experimental results. NACA0012, $J = 0.6$, $V_\infty = 10$ m/s.

7

Conclusion and Recommendations

The objective of this thesis was to increase the understanding of vortex-surface interactions. This was done by quantifying the effect of the governing parameters and sub-phenomena on the magnitude and distribution of the vortex induced pressure fluctuations over a surface. To achieve this goal, an experimental campaign was performed in an open jet, low-speed windtunnel at Delft University of Technology and developing a conceptual model describing the interaction. By answering the research questions posed in Chapter 1, the main findings are presented.

7.1. Conclusions

What is the effect of the governing parameters on the pressure fluctuations induced by the vortex over the surface during the interaction?

- *Which parameters are critical for the vortex surface interaction?* For the vortex-surface interaction treated during this project, namely the case of a tractor propeller and a downstream wing, the most important parameters governing the interaction are the advance ratio and incidence angle. Less critical are the freestream velocity and, in case of symmetric airfoils, the airfoil thickness and nose radius.
- *What effect do the selected parameters have on the magnitude of the pressure fluctuations on the surface?* The pressure fluctuations on the surface increase with decreasing advance ratio. On the advancing side a reduction of the advance ratio from 0.67 to 0.60 results in an increase of the maximum RMS of the unsteady pressure coefficient, $C'_{p,RMS}$, caused by an impingement of the vortex ($0.9 < y/R <= 1.0$) by 156%. The peak unsteady pressure coefficient, C'_p, increases 150%, from 0.04 to 0.10. On the retreating side, the same reduction in advance ratio caused a 28% increase in maximum $C'_{p,RMS}$ and a 30% increase in peak C'_p. The increase in pressure fluctuations is attributed to an increase in vortex strength, associated with the higher propeller blade loading at lower advance ratio. An increase in freestream velocity has a similar effect as a decrease in advance ratio, but it is less pronounced. By increasing the freestream velocity from 10 to 15 m/s (at constant advance ratio), the maximum $C'_{p,RMS}$ increased with 60% on the advancing side. On the retreating side no differences were observed. Contrary to expectations, the airfoil geometry has a no discernible effect on the magnitude of the pressure fluctuations. On the other hand, the incidence angle, meaning the angle between the vortex axis and the lateral surface axis, has a large effect on the magnitude of the pressure fluctuations on the wing. The maximum $C'_{p,RMS}$ caused by the vortex impingement decreased by 72.5% on the advancing side and 28% on the retreating side for an increase in incidence from 0 to 90 degrees. Such a change in incidence angle corresponds to a change from perpendicular to parallel vortex interaction. In the slipstream region, $0.4 < y/R <= 0.9$, on the advancing side the $C'_{p,RMS}$ goes up with increasing incidence angle up to 40 degrees, after which the value decreases to the levels measured at 0 degrees incidence angle. Away from the propeller slipstream boundary, $1.1 < y/R <= 1.3$, on the retreating side, an increase in incidence angle causes an increase in $C'_{p,RMS}$ of a factor 3.
- *What effect do the selected parameters have on the distribution of the pressure fluctuations on the surface?* No discernible difference in unsteady pressure distribution over the surface is present for both a

change in freestream velocity from 10 to 15 m/s (at constant advance ratio) and a change in advance ratio from 0.60 to 0.67. A response to change in advance ratio was expected based on previous studies published in open literature, but may not be visible due to the small change. The surface thickness and nose radius does impact the distribution of unsteady pressure over the surface, primarily due to a change in vortex path. For the NACA0012 the vortex interacts more inboard than is the case for the NACA0016, namely at 0.25 times the vortex radius outboard of the spanwise vortex impingement location identified with the PIV measurements. On the retreating side the spanwise vortex interaction location is at −1.25 times the vortex radius with respect to the location determined with the PIV measurements. The NACA0016 results show a spanwise vortex location of approximately 0.50 times the vortex radius on advancing side and −0.75 times vortex radius on the retreating side. The incidence angle has a very large impact on the distribution of unsteady pressure over the surface. Due to the change in orientation, the area of interaction between the vortex and surface increases, resulting in a wider spanwise distribution of the pressure peak. From 0 to 40 degrees incidence angle, the width of the $C'_{p,RMS}$ peak increases and the location of the pressure peaks moves. On the advancing side the location moves from 0.25 times the vortex core radius outboard of the vortex impingement location determined with the PIV measurements to 1.25 inboard of that location, while on the retreating side the spanwise interaction location moves outboard from −1 to 0 vortex core radii with respect to the location determined with the PIV measurements. Increasing the incidence angle further, from 40 up to 90 degrees, the width of the pressure peak increases dramatically from a distinguishable peak to an almost constant value over the entire measurement width.

How accurate is the conceptual model?

- *What are the quantitative differences between the experimental data and the model results?* In the vortex region, the conceptual model (using the Lamb-Oseen model) overestimates the pressure fluctuations by a factor 3. In the slipstream region at the leading edge the same is true. For the entire freestream region the conceptual model overestimates the pressure fluctuations by much larger amounts, as the fluctuations measured in the freestream region are almost negligible.

- *To what modeling approaches can the differences be attributed?* The main difference between the model and the experimental results was the overestimation of the induced angle of attack effect of the model. In the experimental results this component could not be observed, as only the vortex core pressure and propeller wake could be identified as contributors to the pressure fluctuations. Additionally, the Lamb-Oseen vortex model appears not to be suitable for application in propeller tip vortex modeling. The Lamb-Oseen model assumes a coherent vortex which incorporates all circulation from $t = 0$ and has an infinitely small radius at its inception. In the case of a propeller vortex, the circulation shed from the propeller rolls up into the vortex over an extended period of time. Moreover, the vortex has a finite radius at vortex age $t = 0$. Finally, the method with which radius, and therefore the circulation, was calculated was inaccurate. Seeing that these values were used in determining the tangential velocity distribution and pressure distribution of the vortex, the pressure fluctuations induced by the vortex on the surface were also inaccurate.

What is the relative contribution of the sub-phenomena to the pressure fluctuations induced by the vortex over the surface during the interaction? From the experimental results it is clear that the main component generating pressure fluctuations over the surface is the low pressure vortex core. The vortex path and spanwise location of both vortex filaments and the vortex strength itself are therefore of significant importance. The second largest component contributing to the measured pressure fluctuations is the wake of the propeller, which is not strictly part of a vortex-surface interaction. Although the maximum pressure fluctuations generated by the two components are of the same order, the effect of the wake is limited to the leading edge, while the vortex effect spans over the entire chord. In contradiction to what was initially expected, the induced angle of attack effect caused by the velocities induced by the vortex seems to have a negligible contribution to the total pressure fluctuations induced by the vortex over the surface.

7.2. Recommendations

Though many studies have been performed on the vortex-surface interaction phenomenon, more fundamental investigations are still required. Though the phenomenon is understood in a qualitative way, a lot of

additional quantitative knowledge must be acquired to effectively and efficiently mitigate the noise generated by the interaction.

Considering the unexpected behavior of the vortex at the leading edge of the surface, and the fact that no definitive explanation could be provided for it, further experimental investigation is recommended. Two different experimental campaigns are proposed. The first would be performed in the same tunnel with the same setup, but with the addition of a highly detailed stereo PIV measurement in the x/z-plane at the vortex region at the leading edge of the wing. This would provide a better understanding of the events that cause the vortex behavior at that location. The second setup would be performed with the same wings but in a different tunnel with a more precisely manufactured propeller. The goal of this experiment would be twofold: firstly, to investigate if the unexpected behavior of the vortex at the leading edge was a result of either the poorly manufactured propeller, or the large axial distance of the measurement surface with respect to the propeller plane. Secondly, the different propeller would allow for a larger range of advance ratios to be investigated, which would be used to confirm or dispute the trends identified with the small range of advance ratios currently used.

To investigate the possibility of improving the model and to find out if an accurate solution is possible, an attempt can be made to fit the pressure fluctuations generated by the conceptual model on those obtained from the experiment. A trial and error approach can be employed by changing the circulation value used as input in the model and comparing the waveforms resulting from it to those obtained from the experiment. In doing so the correct value for the circulation can be obtained allowing a better evaluation of the model. Alternatively, a better approach to determine the vortex core radius and corresponding vortex circulation could be devised. This would lead to more accurate modeling of the low pressure vortex core and thus the pressure fluctuations induced by the vortex over the surface.

Although the conceptual model discussed in this report is not accurate, the development of such a simplified model would still contribute a lot to the body of knowledge. It could be used to evaluate the relative contributions of the different vortex-surface interaction sub-phenomena, as suggested in this project. Another use would be the execution of a ‘parameter sweep’ to investigate the effect of the governing parameters on the unsteady pressure distribution and magnitude, which was done in a more limited manner with the experimental campaign. However, for the latter intended use the approach taken in this project would not be recommended as the level of fidelity would be too low. A much more in-depth approach is recommended seeing the complex behavior of the flow.

IV

Appendices

A

Appendix - Microphone Calibration and Data Processing

A.1. Microphone Calibration and Processing Flowchart

The microphones require a frequency dependent calibration, as is described in references [15] and [16]. A number of Matlab routines have been used to perform the calibration, of which the flowchart is provided in Appendix A. The following steps were taken in the calibration process:

- A LinearX M53 reference microphone was calibrated using a GRASS 42AA piston phone at 250 Hz. By dividing the known pressure RMS of the signal, as provided by the manufacturer and corrected for atmospheric conditions, with the RMS of the measured voltage signal, the amplification factor at said frequency, $F_{ref,250Hz}$, is obtained. Combining the amplification factor with the unit specific frequency response curves of the reference microphone provided by the manufacturer allows for the full characterization of its frequency dependent behavior.
- Subsequently, the surface microphones were calibrated. The reference microphone was positioned at approximately 1mm from, and perpendicular to, the surface at the microphone location. A white noise noise audio file was played by a loudspeaker positioned at a distance from the surface to ensure homogeneous noise distribution, as is shown in figure A.1. The voltage signal of both the surface microphone and the reference microphone were recorded. This process was repeated for each surface microphone. It was confirmed that the position and orientation of the reference microphone with respect to the surface did not impact its own measurement, nor that of the surface microphone.
- The voltage signal of the reference microphone, ${v_{ref}}^0(t)$, is multiplied with the amplification factor in order to obtain the pressure. A Fourier transform is performed on the signal and expressed in logarithmic scale, providing the $FPL_{ref}(f)$. The before mentioned frequency correction curve provided by the manufacturer, $\Delta FPL_{cc}(f)$, is then added to the signal. The true pressure spectrum at the measurement location, $P_{ref,corr}(f)$, is obtained by converting the signal back to the linear scale.
- Using a Fourier Transform the voltage signals of each surface microphone were transformed into the frequency domain. Then the true pressure spectrum as well as the microphone voltage spectra for each measurement location are converted into one-third octave bands, resulting in $P_{ref,corr}(f_{1/3})$ and ${V_{mic}}^0(f_{1/3})$. Note that these bands are defined at the center frequencies of each one-third octave band. They are used to obtain a smooth frequency response curve. Interpolation is used to obtain the intermediate response values. Finally, by dividing the pressure spectra by the corresponding voltage spectra, the frequency-dependent response factors are obtained for all surface microphones.

The calibration process was done twice for both wings; once before the experiment and once after. This was done to ensure the first calibration, which was applied to the measured data, was done correctly. For analogy with the typical response curve provided by the manufacturer the sensitivity of the calibration curves, expressed in logarithmic scale (dB re. 1/V), was obtained (see equation A.1). All calibration curves are found in Appendix A. The curves show a distinct quasi-linear region from 100 to 6000 Hz, with a sharp drop in

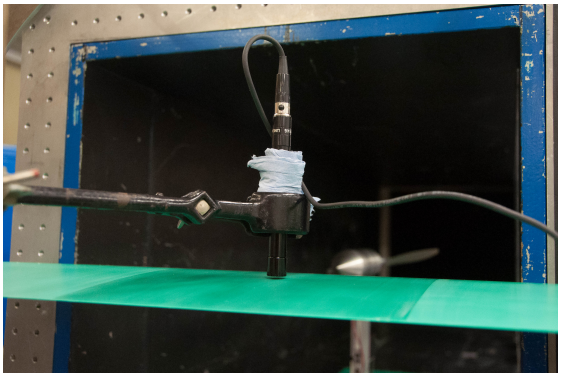

(a) Location of reference microphone position with respect to the surface.

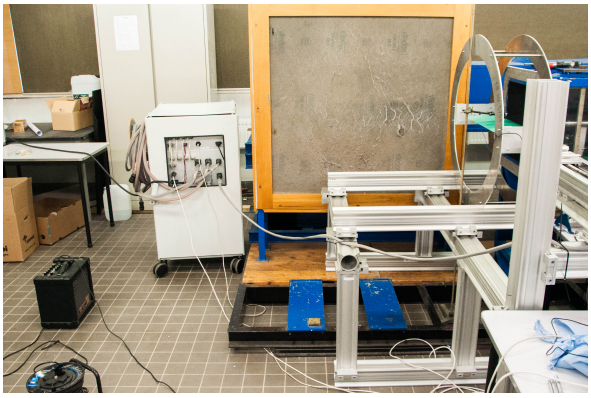

(b) Location of speaker with respect to the measurement surface.

Figure A.1: Overview of calibration setup.

sensitivity above 6000 Hz. This behavior is in accordance with the curve provided by the manufacturer. Both calibration sessions show similar results in this region, but there is a clear difference in behavior for frequency values below 100 Hz. The differences could be attributed to different atmospheric conditions such as relative humidity.

$$\text{sensitivity} = 20 \cdot log_{10}\left(\frac{1}{F_{mic}}\right) \tag{A.1}$$

In figure A.2 the flowchart presenting the operations that are carried out in order to obtain parameters of interest from the raw experimental data. The two main steps are the calibration of the microphones and the processing of the data. A number of notes are indicated in the figure and are as follows:

1. The reference microphone calibration factor is obtained using the piston phone, which operates at a frequency of 250 Hz and a SPL of 114 dB. Therefore, its does not show frequency-dependent behavior.

2. A frequency dependent correction curve that is provided by the reference microphone manufacturer is added to obtain the reference microphone calibration curve.

3. As discussed in chapter 3, a phase shift exists between the NI9125 and NI9234 DAQ modules, which is removed from the microphone signals.

4. As discussed in chapter 3, a mean voltage is present in the signals of each microphone. Seeing that only the fluctuations are of interest, the mean is removed from the signal.

5. Welch's method is used to obtain power spectral densities of the time-dependent variables. This leads to cleaner spectra than with Fourier transforms. Hanning windows of 50% overlap are used. The raw data are divided into approximately 200 windows, obtaining a frequency resolution of 3.125 Hz.

In figures A.3 to A.6 the calibration curves obtained at the start and end of the experiment are provided for both wings.

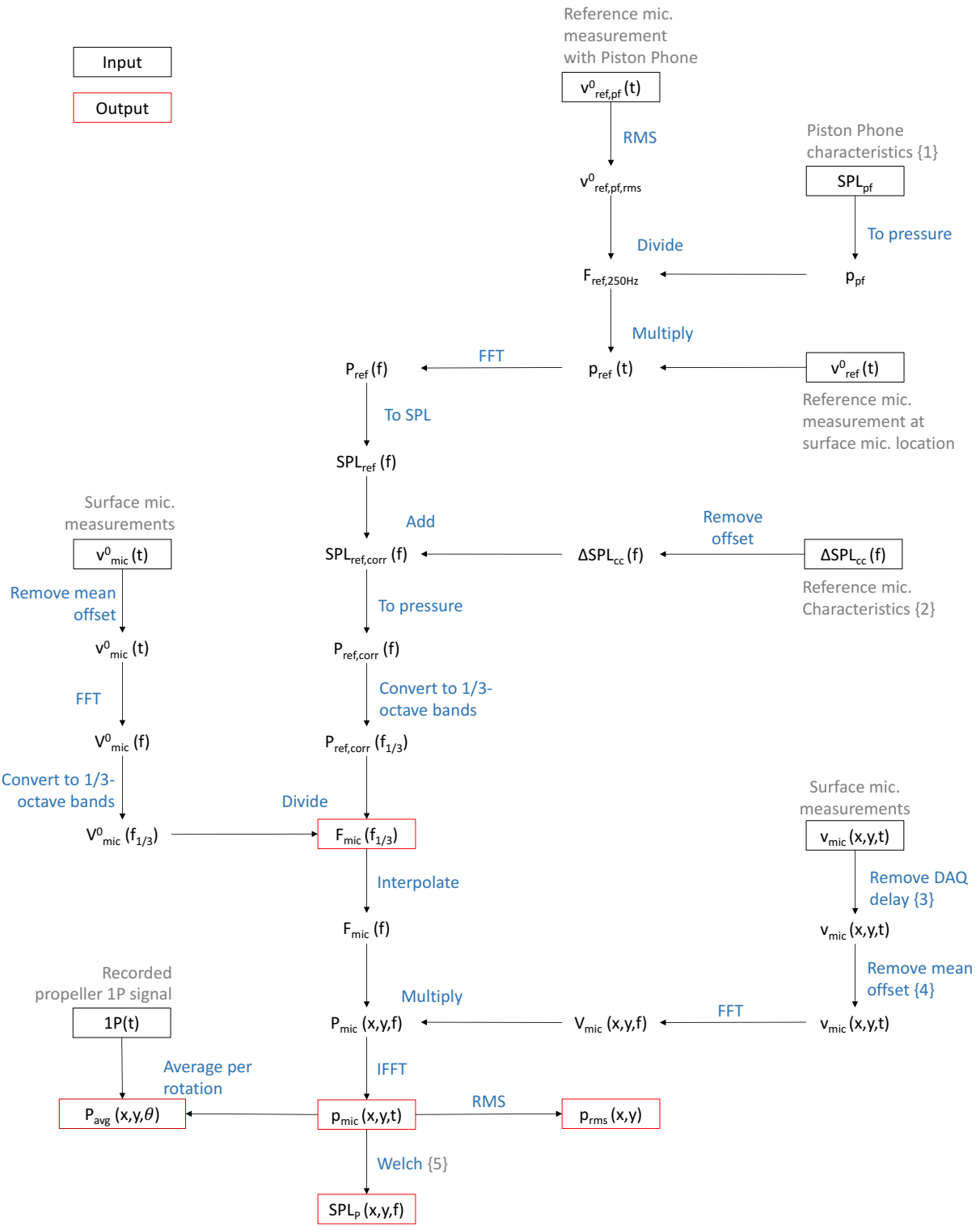

Figure A.2: Calibration and Data Processing Flowchart

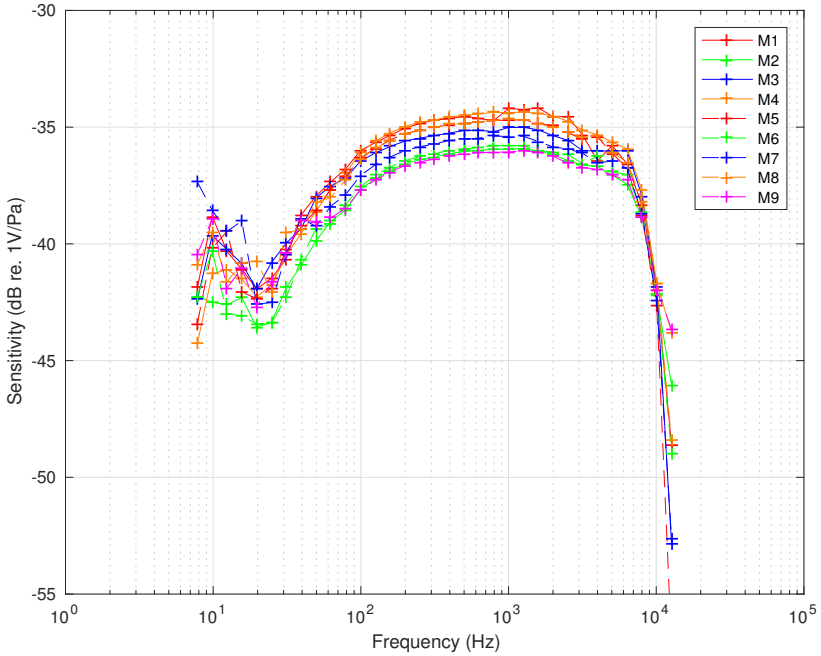

Figure A.3: Calibration curves of wing 1, version 2.

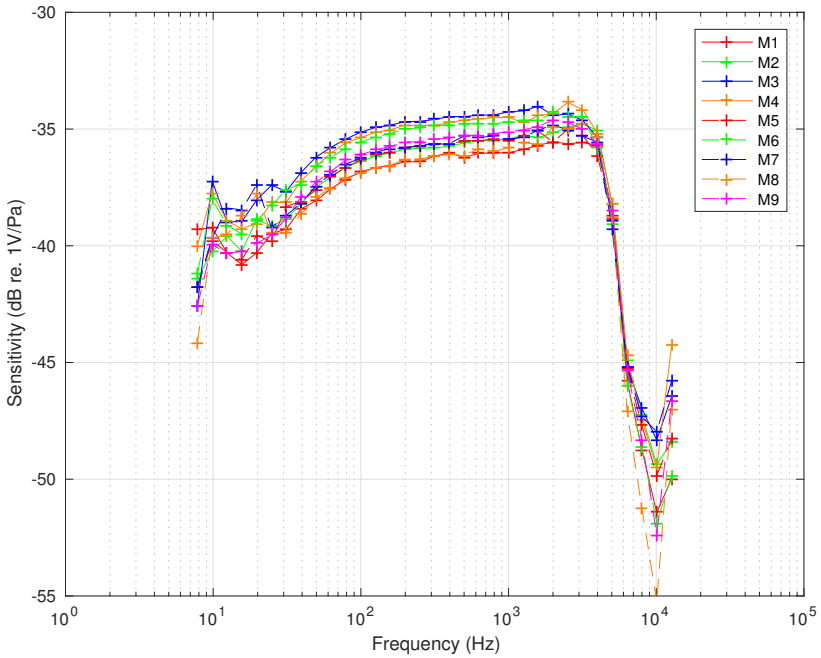

Figure A.4: Calibration curves of wing 2, version 1.

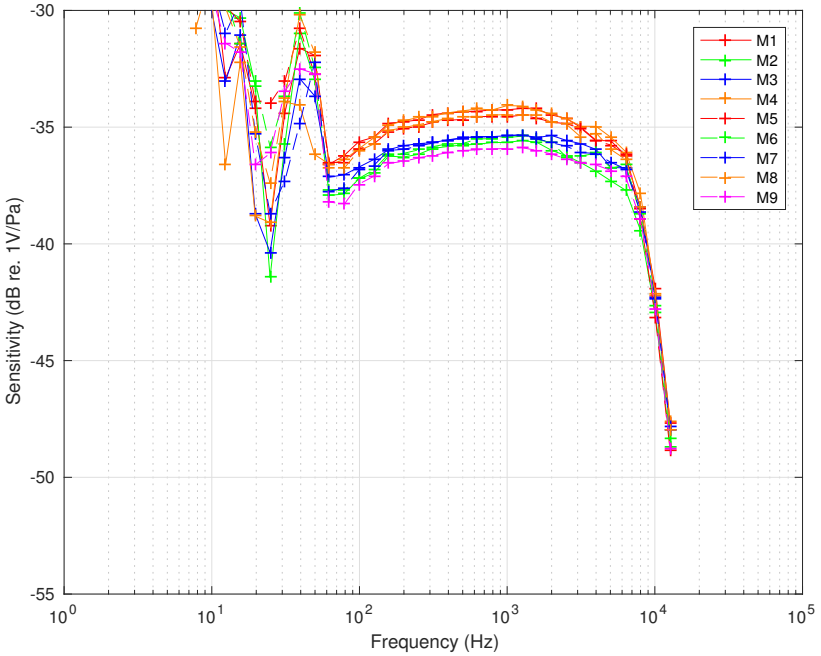

Figure A.5: Calibration curves of wing 1, version 2.

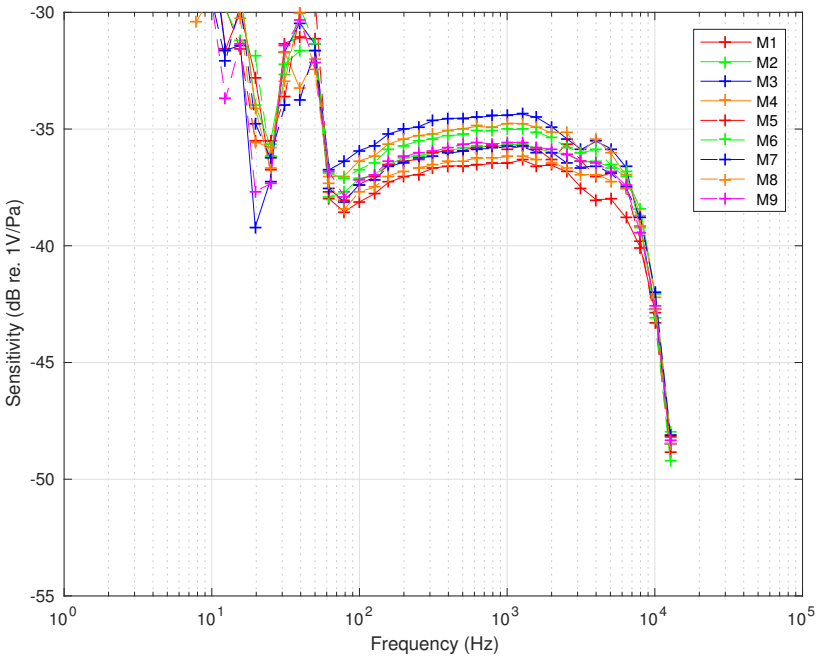

Figure A.6: Calibration curves of wing 2, version 2.

A.2. DAQ System Corrections

The signals generated by the 9 microphones were acquired by three analogue Data Acquisition Systems (DAQ's). Only two NI9234 modules with four ports each were available, so the microphone positioned nearest to the trailing edge (microphone #9) was connected to a different module, the NI9215. There exist a number of differences between the DAQ modules [39] [38]:

- *Resolution;* the NI9215 has a 16 bit resolution versus the 24 bit resolution of the NI9234.
- *Sensitivity;* the NI9215 has a ± 10 V signal range versus a ± 5 V signal range of the NI9234.
- *Phase difference;* although both modules sample their channels simultaneously, the NI9234 contains a anti-aliasing filter, which filters the signal for frequencies above the sampling frequency. The filtering requires a buffering time resulting in a phase shift between the microphone connected to the NI9215 module and those connected to the NI9234 modules.
- *Mean voltage;* the NI9234 is AC/DC coupled, meaning it is possible to set the module so that the output signal only contains the voltage oscillations. This is not the case for the NI9215 module, the signal of which also contains a DC voltage of approximately 0.6 V.

Although the accuracy and sensitivity of the NI9215 module are less than that of the NI9234 modules, the impact on the results is expected to be minimal seeing that the measurements are not required to be particularly accurate or sensitive. The phase shift, however, may be of importance, especially when the phase averaged pressure results are examined. It was found that the phase shift was approximately 12 degrees. Seeing that this is a significant value it was therefore removed during the data processing.

In order to solve the difference in mean voltage between the two DAQ modules and to improve the accuracy of the results, the signal mean was removed from all microphones. As shown in figure A.7, the mean value varies over time and thus a blanket removal of the average mean would not be desirable. A more precise method was chosen, consisting of calculating the mean per propeller revolution and subsequently subtracting it from the signal. Finally, the microphone signal was checked for clipping, of which no evidence was found.

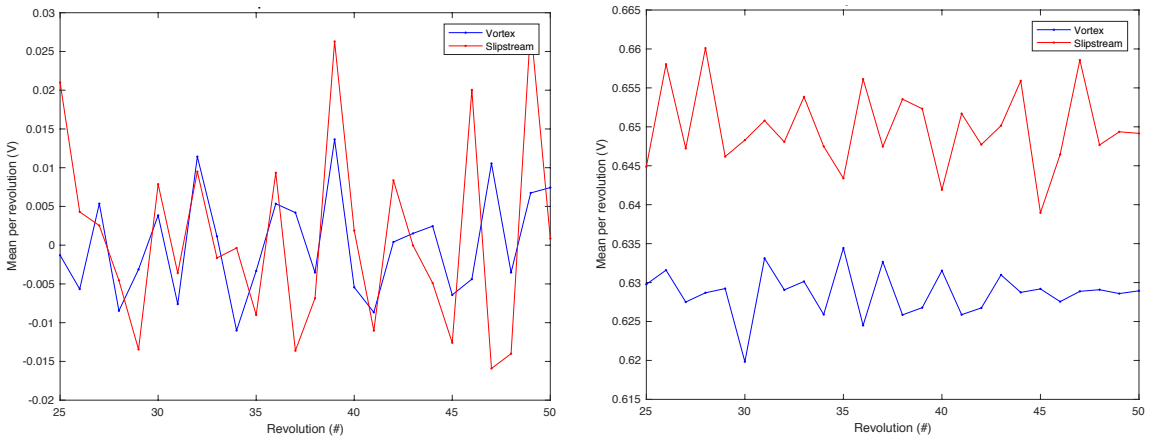

(a) Microphone #1

(b) Microphone #9

Figure A.7: Mean values per rotation for a sample of rotations in the slipstream and vortex regions.

A.3. Phase Averaging

The broadband component of the raw microphone signal was removed, allowing a clearer analysis of the periodic pressure fluctuations related to the vortex-surface interactions. Seeing that the tonal components at the blade passage frequency as observed in the pressure spectra are clearly dominant to the broadband component, as will be discussed in chapter 5, it can be concluded that removing the broadband component will not have a significant effect on the unsteady vortex-surface interactions. The component is removed by a process called 'phase averaging', in which the microphone signal is split up into time intervals corresponding to one full propeller revolution and averaged over all rotations. A temporal resolution of 1 degree is used, which is relatively accurate and can easily be achieved. It can be observed that the results converge for the sampling rate and acquisition time used during the experiment, as is demonstrated in figure A.8.

Although convergence is proven, the curves obtained from the phase averaging do show a significant amount of fluctuations. This is likely the result of a high amplitude of the random fluctuations within the signal, which can be attributed to two sources. Firstly, the windtunnel that was used to perform the experiment has a relatively high level of freestream turbulence. Secondly, the source of fluctuations could be the hardware used in the experiment. However, the hardware in question, namely the Sonion 8010T microphones and the NI9234 and NI9215 DAQ's, has been used in earlier experiments performed in a different (less turbulent) wind tunnel at the LSL, which produced results with a much lower level of fluctuations [15]. Therefore, the hardware as source of the fluctuations is deemed improbable. It is concluded that although the fluctuations are significant, the converged solutions allow for an effective analysis.

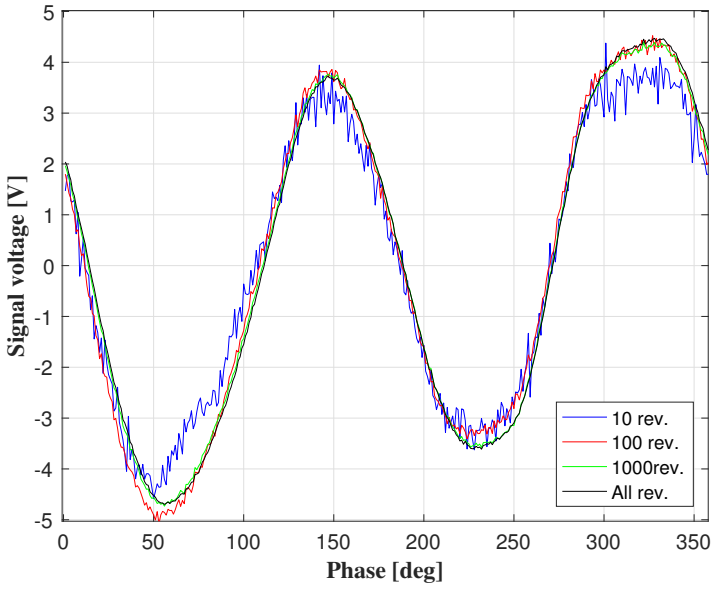

Figure A.8: Example of convergence of phase averaged results for increased number of propeller rotations.

A.4. PIV Processing

The PIV calibration was performed using a calibration plate that was positioned exactly in the FOV. The cameras were focused on the plate and a calibration image of the plate was taken. The designated PIV post-processing software, in this case Davis version 8.3, can then calculate the location and orientation of the plate, correct the FOV and scale the axes.

In order to obtain the vector field of a certain flowfield, the particles in both images of the image pair need to be cross-correlated. A number of processing steps were taken in order to increase the accuracy with which the cross-correlation is done by the software. The following steps were taken in order to optimize the resulting vector field, with the corresponding images provided in figure A.9:

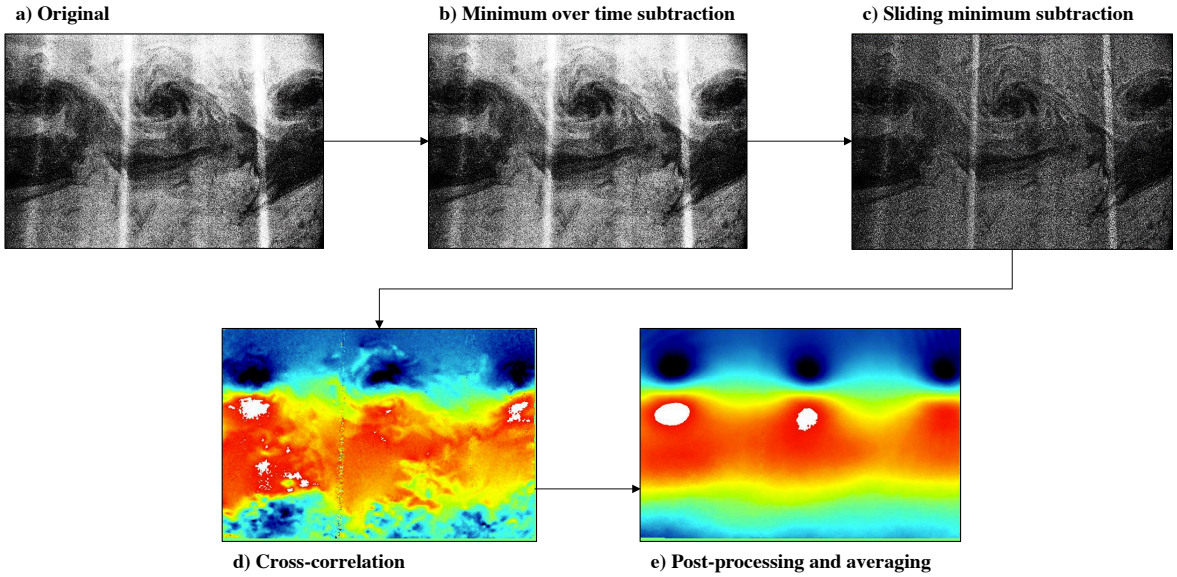

Figure A.9: Images depicting the PIV processing steps taken.

- *Minimum over time subtraction;* for every pixel in each image, the lowest intensity value for that pixel observed in the entire set of images, was subtracted. This action resulted in a higher contrast in the images, which in turn allows for better cross-correlation.
- *Sliding minimum subtraction;* a normalization of each image was performed, in order to remove discrepancies, such as a laser that has is brighter on one side of the image than on the other.
- *Cross correlation;* the cross correlation that was employed was a sequential multipass with a 24 x 24 pixel window size and 50% overlap. For a detailed description on cross correlation, consult reference [44].
- *Post processing;* finally, the resulting PIV vector fields were smoothed and the average was taken over all images.

A.5. Infrared Reflective Sensor

The blade passage frequency of the propeller was determined by means of an infrared reflective sensor, which consists of an IR LED and a phototransistor pair. The motor has a hole in its nacelle just behind the propeller which provides a line of sight between the sensor and the propeller axis. On two sides of the axis a reflective dot is present. When the reflected light is detected a voltage is generated. This signal is read at a sampling rate of 150 Hz and analyzed by an RPS counter and subsequently acquired by a National Instruments 9215 DAQ module and stored using LabView software.

The alignment of the two sensor components with the reflective dot on the propeller shaft is relatively sensitive. Additionally, in order to allow free movement to the load cell, which is required for valid thrust measurements, the propeller motor and pylon are not connected. This means that the optical sensor remains in place while the motor moves when thrust is increased. This can result in erroneous signals, due to the fact that the rotation of the axis is not registered. An example of such a signal is provided in figure A.10. in the post-processing, done with Matlab R2016a, these signals have been identified and the missing peaks have been replaced.

Furthermore, two sanity checks on the correctness of the 1P signal were performed. Firstly, the pitch of the vortex helix was determined from the PIV images allowing for the calculation of the corresponding RPS. Secondly, the frequency spectrum of the microphone data was examined and the 1P signal was located. From these checks it was concluded that the system was working nominally.

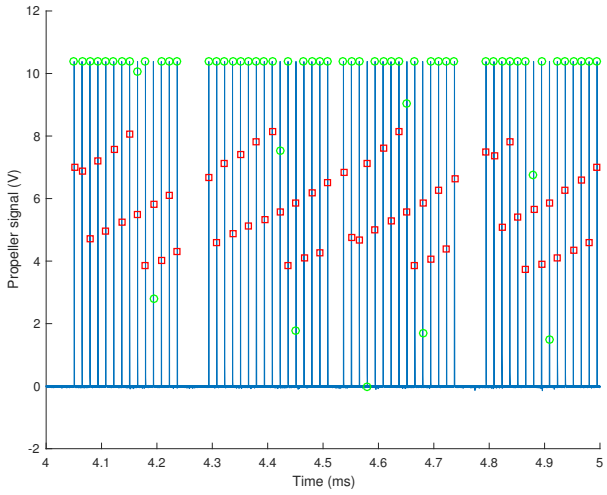

Figure A.10: Example of erroneous propeller signal data.

B

Appendix - Background Noise

B.1. Background Noise Plots

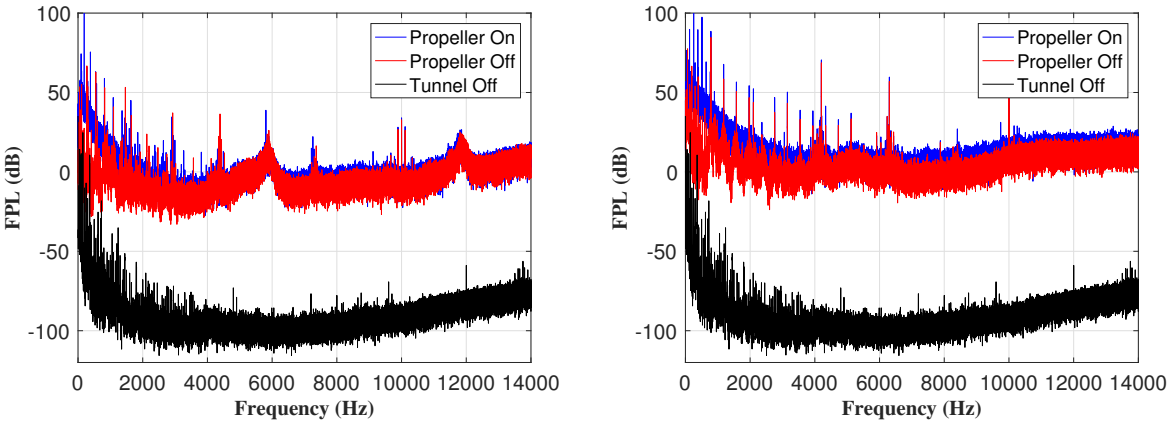

(a) NACA0012, Case 1

(b) NACA0012, Case 3

(c) NACA0016, Case 1

(d) NACA0016, Case 3

Figure B.1: Background noise measurements for test cases 1 (J = 0.60 and $V_i nf$ = 10 [m/s]) and 3 (J = 0.67 and $V_i nf$ = 15 [m/s]) and NACA0012 and NACA0016

C

Appendix - Additional Experimental Results

C.1. Contour Plots of RMS of Unsteady Pressure Coefficient on the Wing Surface

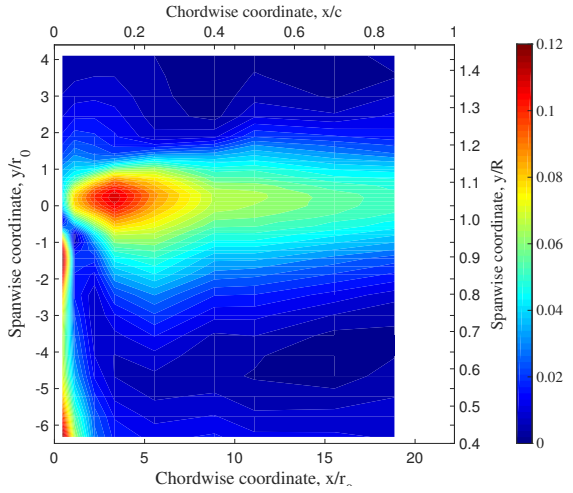

(a) Advancing side, case 1

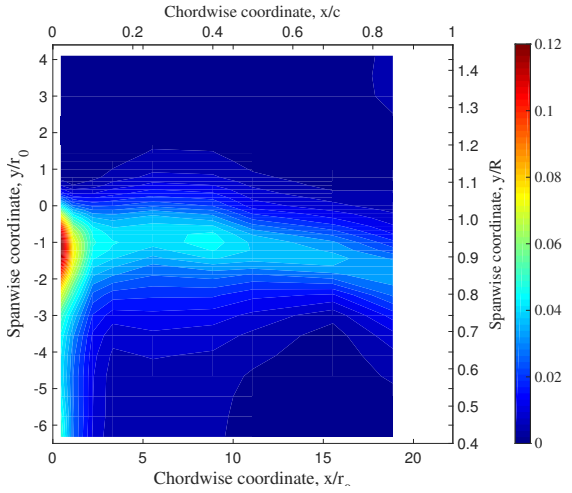

(b) Retreating side, case 1

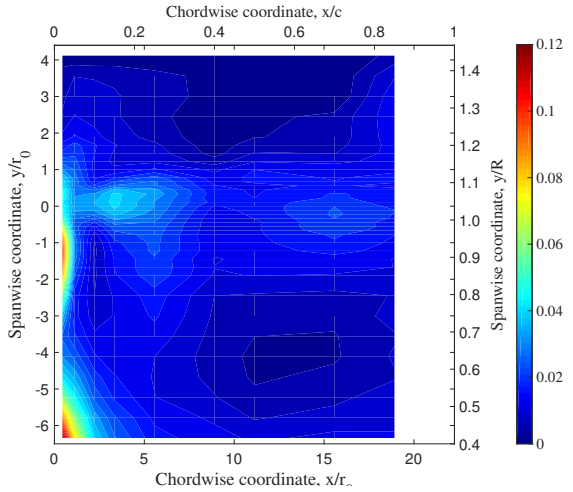

(c) Advancing side, case 2

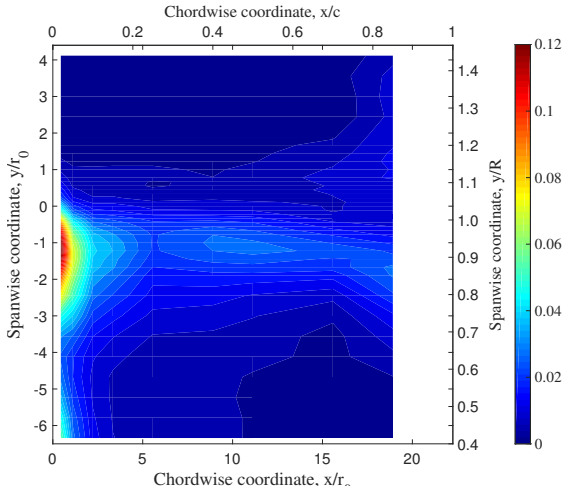

(d) Retreating side, case 2

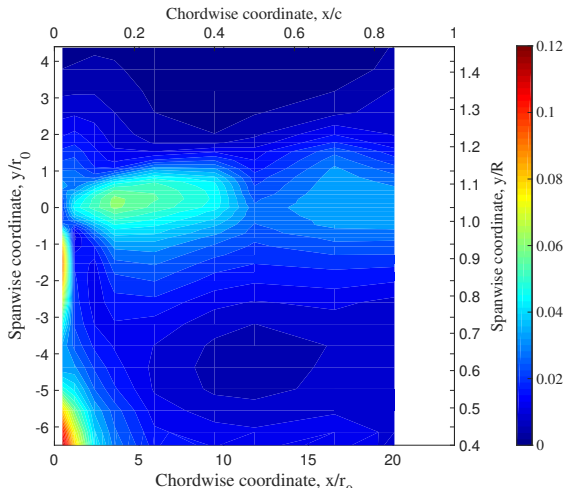

(e) Advancing side, case 3

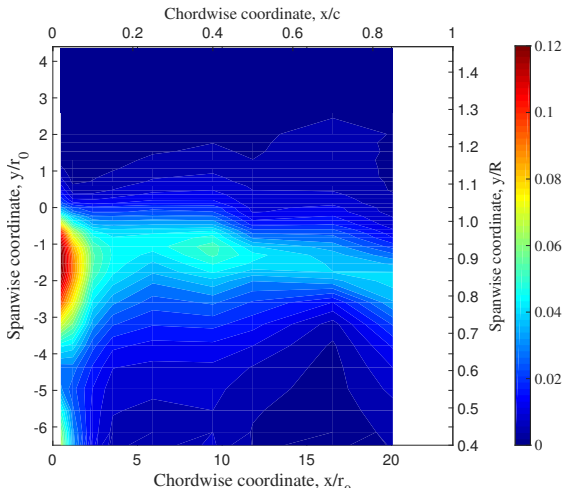

(f) Retreating side, case 3

Figure C.1: Contourplots of the $C'_{p,RMS}$ distributions on advancing and retreating side from experiment. Linear scale, airfoil NACA0012.

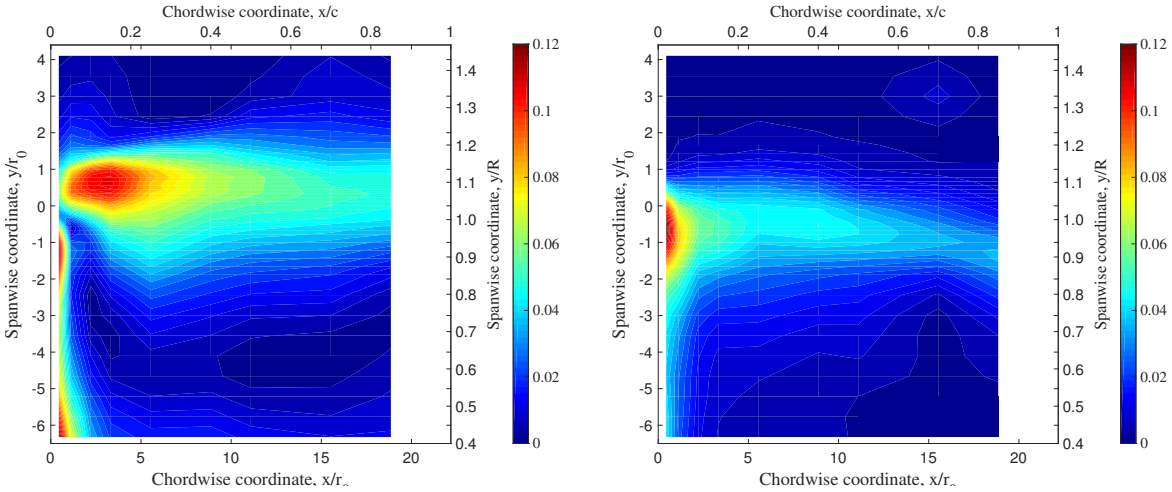

(a) Advancing side, case 1

(b) Retreating side, case 1

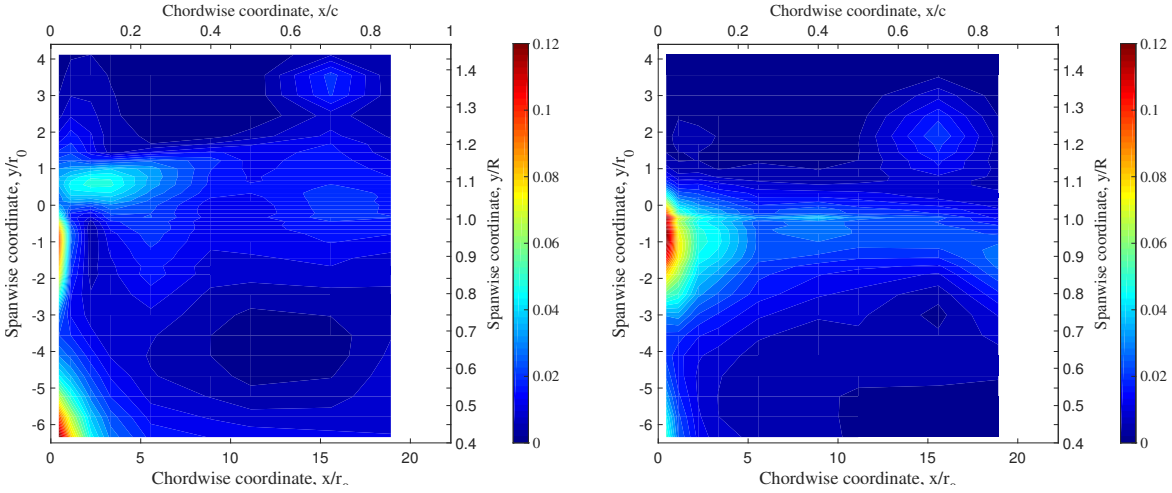

(c) Advancing side, case 2

(d) Retreating side, case 2

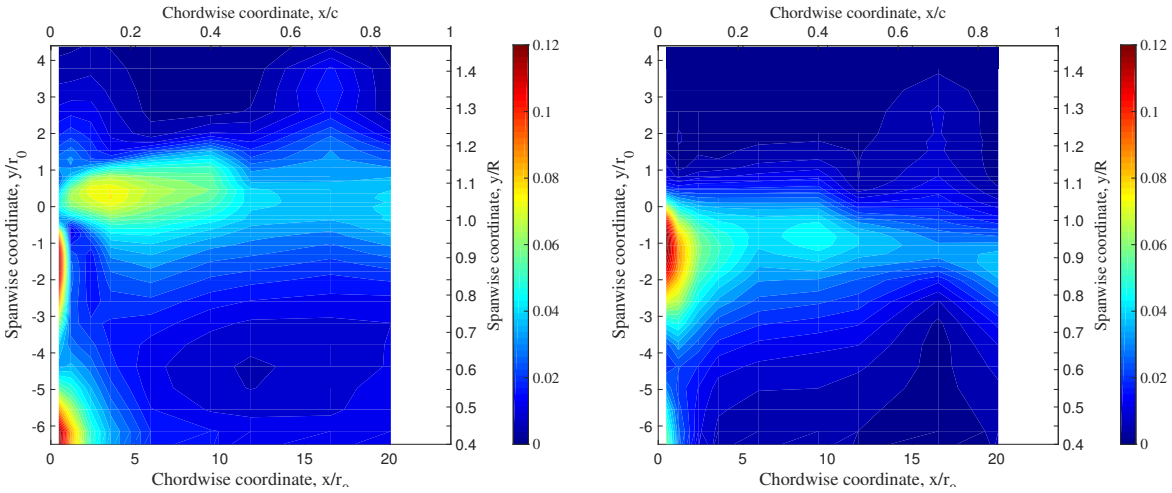

(e) Advancing side, case 3

(f) Retreating side, case 3

Figure C.2: Contourplots of the $C'_{p,RMS}$ distributions on advancing and retreating side from experiment. Linear scale, airfoil NACA0016.

C.2. Spanwise Distribution of the RMS of the Unsteady Pressure Coefficient

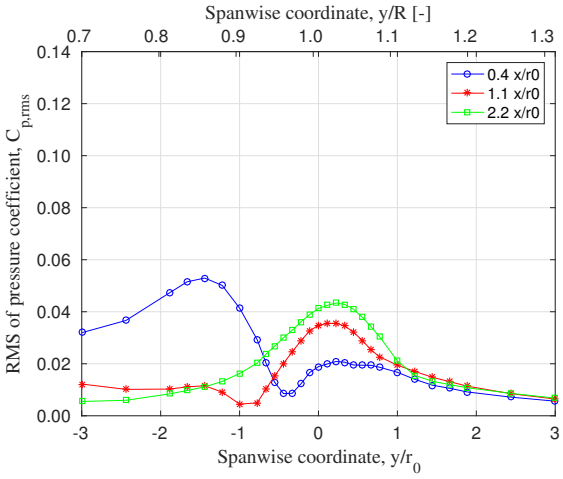

(a) Case 1, advancing side

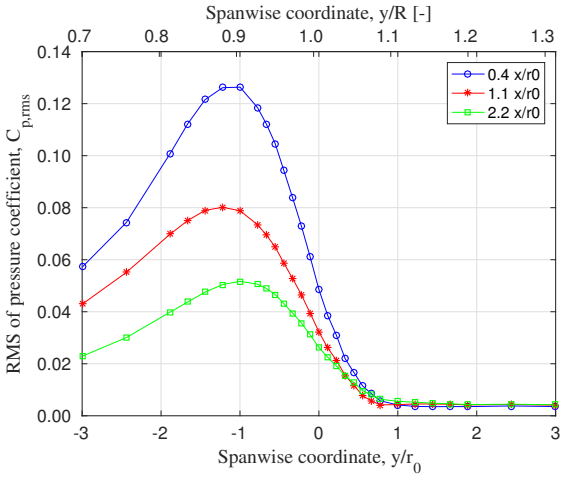

(b) Case 1, retreating side

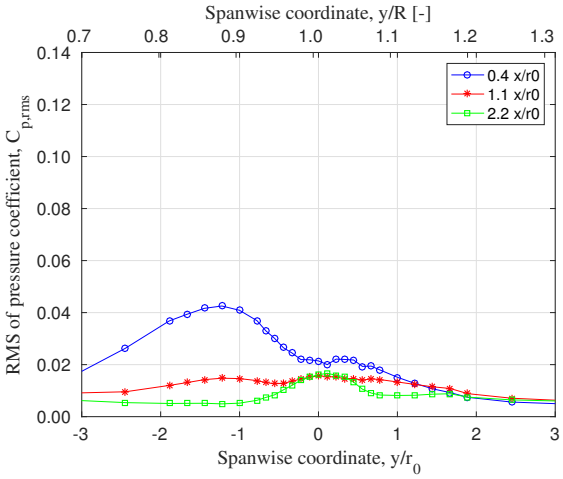

(c) Case 2, advancing side

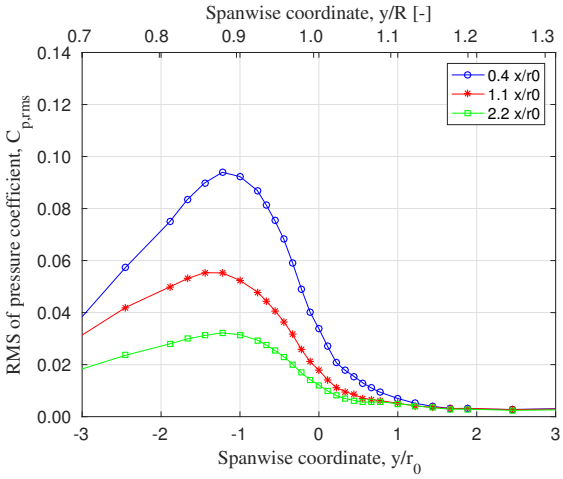

(d) Case 2, retreating side

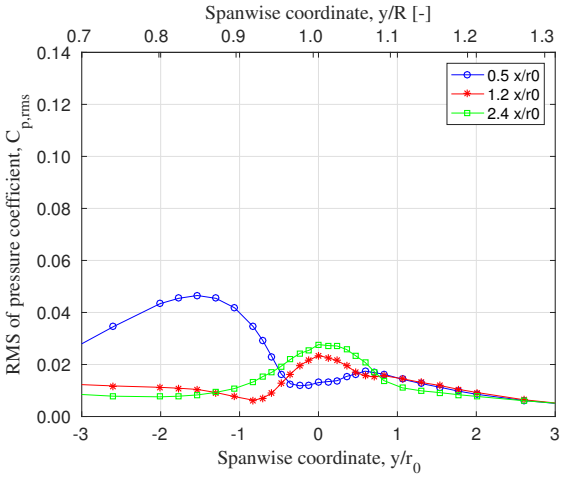

(e) Case 3, advancing side

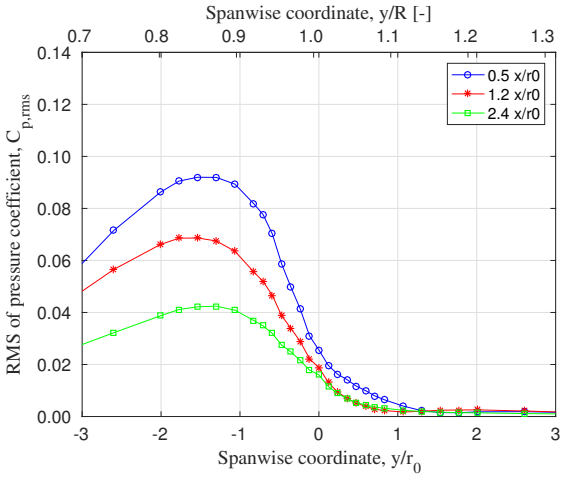

(f) Case 3, retreating side

Figure C.3: Aft view experimental $C'_{p,RMS}$ at leading edge on advancing and retreating surfaces. NACA0012, Cases 1, 2 and 3

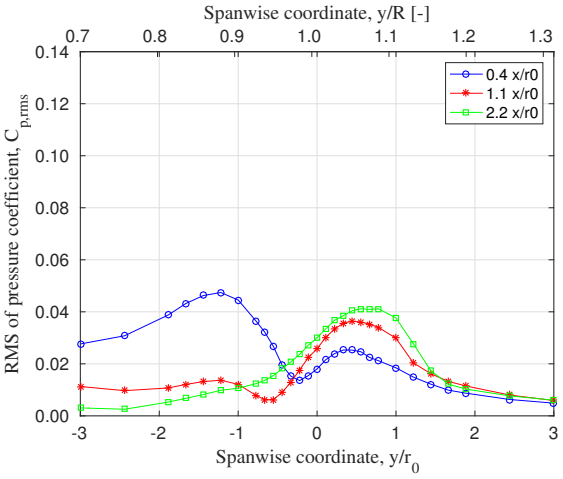

(a) Case 1, advancing side

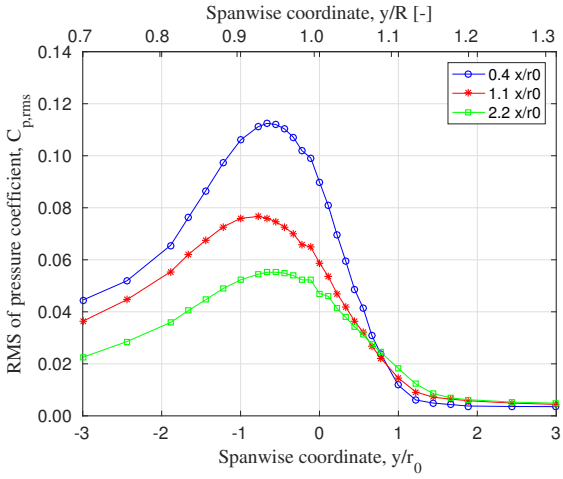

(b) Case 1, retreating side

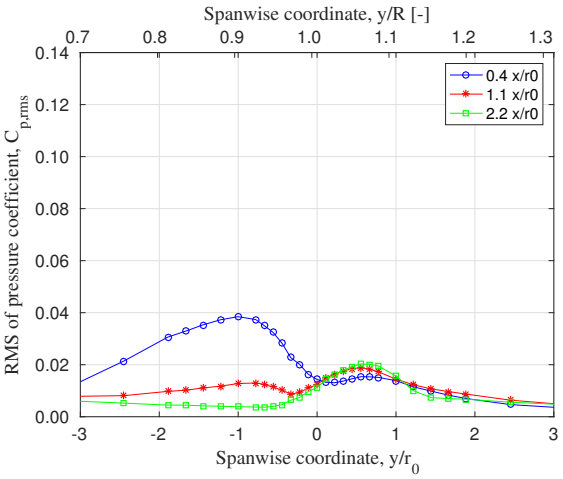

(c) Case 2, advancing side

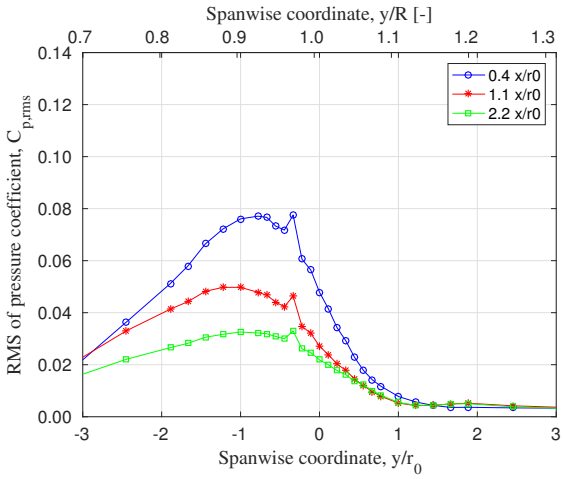

(d) Case 2, retreating side

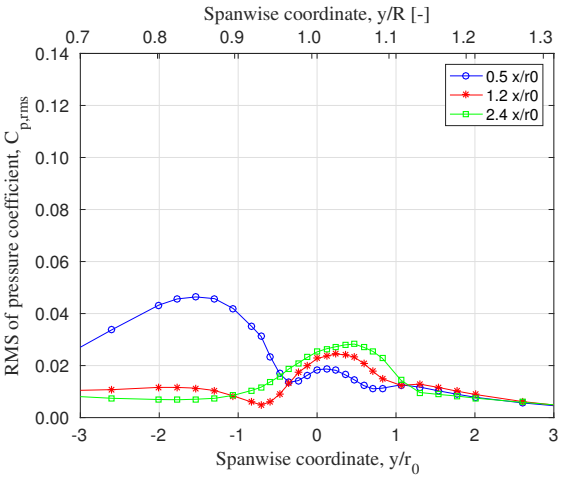

(e) Case 3, advancing side

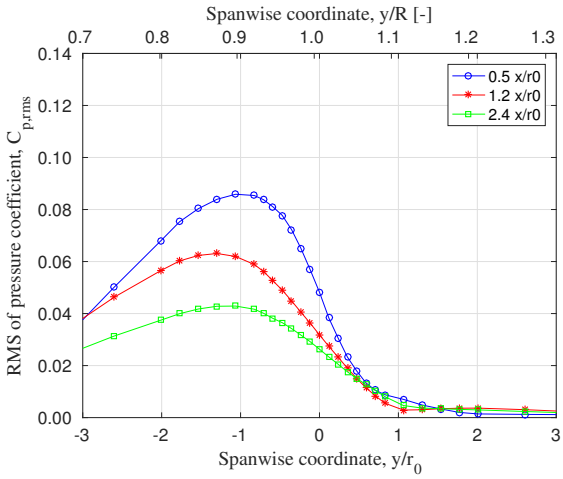

(f) Case 3, retreating side

Figure C.4: Aft view experimental $C'_{p,RMS}$ at leading edge on advancing and retreating surfaces. NACA0016, Cases 1, 2 and 3

C.3. Vortex Path

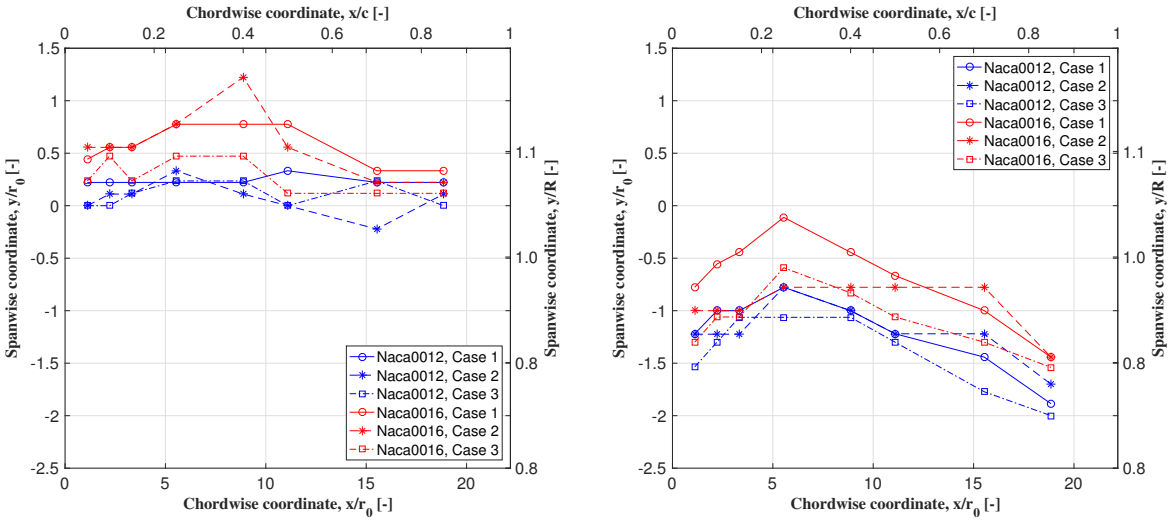

(a) Advancing side

(b) Retreating side

Figure C.5: Spanwise $C'_{p,RMS,max}$ location at each chordwise microphone position for all combinations of cases, wings and surfaces. In these figures the first microphone position has been added.

Bibliography

[1] D.C. Mikkelson, G.A. Mitchell, and L.J. Bober. Summary of recent nasa propeller research. In *AGARD Fluid Dynamics Panel Meeting on Aerodynamics*, 1984.

[2] R.D. Hager and D. Vrabel. Advanced Turboprop Project. Technical report, NASA Lewis Research Center, 1988.

[3] R. Babikian, S.P. Lukachko, and I.A. Waitz. The historical fuel efficiency characteristics of regional aircraft from technological, operational, and cost perspectives. *Journal of Air Transport Management*, 2002.

[4] Europrop International GmbH. `https://www.europrop-int.com/`. [Online; accessed 23-05-2016].

[5] The High-Level Group on Aviation Research. FlightPath 2050 - Europe's Vision for Aviation. `http://ec.europa.eu/transport/modes/air/doc/flightpath2050.pdf`. [Online; accessed 06-04-2017].

[6] J.B.Jr. Whitlow and G.K. Sievers. Summary of recent nasa propeller research. In *AGARD Fluid Dynamics Panel Meeting on Aerodynamics*, 1984.

[7] C.H. Hansen. *Occupational Exposure to Noise: Evaluation, Prevention and Control. World Healt Organisation Special Report, S64*, chapter 1. Fundamentals of Acoustics. Federal Institute for Occupational Safety and Health.

[8] M. Roger, C Schram, and S. Moreau. On open rotor blade-vortex interaction noise. *AIAA Aeroacoustics Conference*, 2012.

[9] L.L.M. Veldhuis. *Propeller wing aerodynamic interference*. PhD thesis, Delft University of Technology, 2005.

[10] S. Ljunggren, I. Samuelsson, and K. Widig. Slipstream-Induced Pressure Fluctuations on a Wing Panel. *Journal of Aircraft*, 1989.

[11] I.J. Loeffler. Structureborne noise conctrol in advanced turboprop aircraft. *25th Aerospace Sciences Meeting*, 1987.

[12] R.K. Majjigi, K. Uenishi, and P.R. Gliebe. An Investigation of Counterrotating Tip Vortex Interaction. Technical report, NASA Lewis Research Center, 1989.

[13] Q. R. Wald. The Aerodynamics of Propellers. *Progress in Aerospace Sciences*, 2006.

[14] S.I. Green. *Fluid Vortices*. Kluwer Academic Publishers, 1994.

[15] R. de Vries. *Unsteady Pylon Loading for Pylon-Mounted Tractor Propellers*. PhD thesis, Delft University of Technology, 2016.

[16] R.T. Johnston and J.P. Sullivan. Unsteady Wing Surface Pressures in the Wake of a Propeller. *Journal of Aircraft*, 1992.

[17] M. Roger, C Schram, and S. Moreau. On vortex–airfoil interaction noise including span-end effects, with application to open-rotor aeroacoustics. *Journal of Sound and Vibration*, 2014.

[18] A.D. Thom and K. Duraisamy. Computational Investigation of Unsteadiness in Propeller Wake–Wing Interactions. *Journal of Aircraft*, 2013.

[19] F. Falissard and G. Delattre. Investigation of Counter-Rotating Open-Rotor Orthogonal Blade / Vortex Interaction Noise. *20th AIAA/CEAS Aeroacoustics Conference 20th AIAA/CEAS Aeroacoustics Conference*, 2014.

[20] M. Roger and A. Carazo. Blade-geometry considerations in analytical gust-airfoil interaction noise models. *AIAA Aeroacoustics Conference*, 2010.

[21] M.E. Quaglia, S. Moreau, M. Roger, and R. Fernando. A three-dimensional analytical approach for open-rotor blade vortex interaction (bvi) tonal noise. *AIAA Aeroacoustics Conference*, 2015.

[22] R.H. Schlinker and R.K. Amiet. Airfoil gust response and the sound produced by airfoil-vortex interaction. *AIAA Aeroacoustics Conference*, 1984.

[23] M.J. Kingan and R.H. Self. Counter-Rotation Propeller Tip Vortex Interaction Noise. *15th AIAA/CEAS Aeroacoustics Conference*, 2009.

[24] F.X. Caradonna, J. Lautenschlager, and M. Silva. An Experimental Study of Rotor-Vortex Interactions. *26th Aerospace Sciences Meeting*, 1988.

[25] H. Glauert. *The Elemensts of Aerofoil and Airscrew Theory*. Cambridge University Press, 1983.

[26] R.T. Johnston and J.P. Sullivan. Experimental Results of a Propeller / Wing Interaction Study. *Journal of Aircraft*, 1991.

[27] D. K. Gowanlock and C. S. Matthewson. Control of Rotor Tip Vortices. *37th AIAA Aerospace Sciences Meeting and Exhibit*, 1999.

[28] J. C. McWilliams. A Demonstration of the Suppresion of Turbulent Cascades by Coherent Vortices in Two-Dimensional Turbulence. *Journal of Aircraft*, 2013.

[29] Y. O. Han and J. G. Leishman. Investigation of Helicopter Rotor-Blade-Tip-Vortex Alleviation Using a Slotted Tip. *AIAA Journal*, 2004.

[30] Roxana Vasilescu. *Helicopter Blade Tip Vortex Modifications in Hover Using Piezoelectrically Modulated Blowing*. PhD thesis, 2004.

[31] Anderson Jr., J.D. *Fundamentals of Aerodynamics*. McGraw-Hill, 1985.

[32] A.R. Ahmadi. An Experimental Investigation of Blade-Vortex Interaction at Normal Incidence. *23rd AIAA Aerospace Sciences Meeting*, 1985.

[33] A.T. Conlisk. A Theory of Vortex-Surface Collisions. *2nd AIAA, Theoretical Fluid Mechanics Meeting*, (1995), 1998.

[34] D. Rockwell. Vortex-Body Interactions. *Annual Review of Fluid Mechanics*, 30(Wardlaw 1980), 1998.

[35] P. Margaris and I. Gursul. Vortex Topology of Wing Tip Blowing. *Aerospace Science and Technology*, 2010.

[36] S. Vedamanickam. *Aerodynamics of a Two-Bladed Propeller with Passive Blade Tip-Vortex Control*. PhD thesis, Delft University of Technology, 2017.

[37] SONION. *Microphone 8010T Data Sheet*, September 2015. Version 3.

[38] National Instruments. *NI9234 DAQ Data Sheet*, October 2015.

[39] National Instruments. *NI9215 DAQ Data Sheet*, March 2016.

[40] M. Alster. Improved calculation of resonant frequencies of helmholtz resonators. *Journal of Sound and Vibration*, 24(1):63 – 85, 1972.

[41] Fokker. *Fokker F50 Specification Sheet*. "Online; accessed 06-04-2016".

[42] M. Drela. `http://web.mit.edu/drela/Public/web/xfoil/`. [Online; accessed 06-08-2017].

[43] D. Michaelis, D.R. Neal, and B. Wieneke. Peak-locking reduction for particle image velocimetry. *Measurement Science and Technology*, 27(10):104005, 2016.

[44] M. Raffel, C.E. Willert, and J. Kompenhans. *Particle Image Velocimetry - A practical guide*. Springer, 2nd edition edition, 2007.

[45] D. Ragni, A. Ashok, B.W. van Oudheusden, and F. Scarano. Surface pressure and aerodynamic loads determination of a transonic airfoil based on particle image velocimetry. *Measurement Science and Technology*, 20(7), 2009.

[46] R.W. Deters, A. Krishnan, G. Kumar, and M.S. Selig. Reynolds Number Effects on the Performance of Small-Scale Propellers. In *32nd AIAA Applied Aerodynamics Conference*, AIAA Aviation Forum. American Institute of Aeronautics and Astronautics, jun 2014.

[47] M.S. Selig, J.F. Donovan, and D.B. Fraser. *Airfoils at Low-Speeds*. SoarTech Publications, 1989.

[48] R. de Vries, T. Sinnige, B. Della Corte, F. Avallone, D. Ragni, G. Eitelberg, and L.L.M. Veldhuis. Tractor Propeller-Pylon Interaction, Part I: Characterization of Unsteady Pylon Loading. AIAA SciTech Forum. American Institute of Aeronautics and Astronautics, 2017.